Title
Partial-Transient-Liquid-Phase Bonding of Advanced Ceramics Using Surface-Modified Interlayers

Author
Reynolds, Thomas Bither

Publication Date
2012

Peer reviewed|Thesis/dissertation

Partial-Transient-Liquid-Phase Bonding of Advanced Ceramics Using Surface-Modified Interlayers

By

Thomas Bither Reynolds

A dissertation submitted in partial satisfaction of the

requirements for the degree of

Doctor of Philosophy

in

Engineering – Materials Science and Engineering

in the

Graduate Division

of the

University of California, Berkeley

Committee in charge:

Professor Andreas M. Glaeser, Chair
Professor Ronald Gronsky
Professor Claudia Ostertag

Fall 2012

Partial-Transient-Liquid-Phase Bonding of Advanced Ceramics
Using Surface-Modified Interlayers

by Thomas Bither Reynolds

Abstract

Partial-Transient-Liquid-Phase Bonding of Advanced Ceramics
Using Surface-Modified Interlayers

by

Thomas Bither Reynolds

Doctor of Philosophy in Materials Science and Engineering

University of California, Berkeley

Professor Andreas M. Glaeser, Chair

Partial-transient-liquid-phase (PTLP) bonding of advanced ceramics employs an A/B/A sandwich-style interlayer that is designed such that the outer cladding, A, forms a transient-liquid phase that disappears at the bonding temperature due to diffusion of A into the core layer, B. The resultant bonds can have re-melt temperatures that are significantly higher than the bonding temperature. The success of PTLP bonding relies on the proper selection of the interlayer components: the transient liquid must be able to flow into and fill strength-limiting interfacial flaws, the adhesion between the interlayer and the bulk ceramic must be sufficiently high to prevent interfacial failure, the formation of strength-reducing brittle phases at the interface should be minimized, and the residual stresses due to coefficient of thermal expansion (CTE) mismatch should be minimized. The composition of the transient liquid predominately determines the interfacial characteristics of the bond, while the core composition determines the residual stresses in the assembly. In recent work, Al_2O_3 bonded using Ni/Nb/Ni interlayers produced joints that were of such high strength that all bonded samples failed exclusively in the ceramic and not at the joint during 4-point bend testing.

The wetting characteristics of the Ni-Nb transient-liquid and the CTE of Nb are favorable for the fabrication of strong PTLP-bonded Al_2O_3. However, for other ceramic systems, using a binary interlayer system such as Ni-Nb may not be desirable. When using binary interlayers it is not possible to control the composition of the transient liquid and the core independently. In order to expand PTLP bonding to other advanced ceramics, this study examined a new interlayer design that employs a surface-modified core, such as Mo-surface-modified Nb, instead of a homogeneous core, such as pure Nb. A surface-modified core is a core layer with an intentionally inhomogeneous composition in order to better control the composition of the transient-liquid and the core layer independently. It was found that Al_2O_3 PTLP bonded using a Mo-surface-modified V core and a Ni cladding had fracture strengths of 302±29 MPa. This is comparable to those using Ni/Nb/Ni interlayers, 341±28 MPa. In both assemblies, all of the samples failed in the ceramic bulk. The insights gained from these experiments were used to develop interlayer design guidelines for the PTLP bonding of other advanced ceramics.

To my family.

Contents

Acknowledgements

I wouldn't have been able to complete this work without the support of those around me. A hearty thanks to my advisor, Professor Glaeser, who put up with me for all these years and suffered through the innumerable mistakes in all of my drafts. Thanks goes out to the research group, both past and present: Joe, Josh, Melissa, Sung, Chris, Mary, and Miri. You made the low points easier to get through, and I appreciate the support. Thanks to all my friends for the great memories, and for helping keep me grounded throughout the grad school experience. And finally, thanks to my family, for having faith that I would eventually get out of college.

I also would like to acknowledge the financial support of the NSF and the IMI Program of the National Science Foundation under Award No. DMR 0843934, without which this work could not have been completed.

1. Introduction

To produce higher-performing products, the use of dissimilar materials within a single device is often the only way to achieve the desired performance goals. Ceramic materials in particular – with their low densities, high melting temperatures, high compressive strengths, and good corrosion resistance – are reemerging as desirable components in aeronautical, aerospace, industrial, and nuclear applications. However, their brittle and inert nature also poses a number of technical challenges that have limited ceramics from being easily integrated into larger systems, and thus has prevented their advantageous properties from being exploited to the fullest. As a result, the ability to quickly and reliably bond ceramics both to dissimilar materials and to themselves will play an important role in the future implementation of ceramics in cutting-edge devices.

When bonding ceramics to a dissimilar material such as a metal, a number of materials-selection and preparation criteria must be met to form a strong and reliable bond. There must be good contact between the metal and ceramic component to minimize the number of voids or flaws, which can act as stress-concentrators, at the interface. This can be accomplished through mechanical polishing of the bonding surfaces, through the use of a liquid phase that spreads across the interface and solidifies at some point during the bonding process, or some combination thereof. The bonded components must have inherently strong interfacial adhesion; otherwise the interface will fail well below the strength of the bulk constituents. Residual stresses that may be introduced during the cooling cycle of the joining process must be minimized in order to maintain the inherent strength of the bonded materials. The materials' composition must be chosen carefully in order to manage or minimize the formation of secondary phases, which often have drastically different properties than the parent materials, and can introduce additional residual stresses or weak interfaces that can cause failure. Finally, if the bonded assembly is intended to be used at higher temperatures, the materials themselves must have high enough melting temperatures to mitigate the effects of creep or other high-temperature degradation processes.

To be commercially viable, there are a number of desired features for the bonding process beyond those required solely to produce a strong bond. Relatively low bonding temperatures and short bonding times both lower the energy and overall production costs. Minimizing the preparation time through less-stringent surface preparation requirements can also reduce costs. Finally, the ability to scale the procedure by processing large numbers of samples simultaneously, such as by minimizing any applied pressures during joining, will drastically reduce production and labor expenses.

Currently, diffusion bonding and brazing are the two most common techniques used to bond ceramic components. Diffusion bonding is a solid-state process, where the materials to be joined are placed in contact with one another at a temperature at which diffusion can occur across and along the interface to eliminate any interfacial voids and flaws, typically 0.5-0.9× the melting temperature of one or both components. To minimize the diffusion distances and thus the time needed for bonding, stringent surface preparation is needed to reduce the size of the interfacial voids prior to bonding. In addition, high applied pressures are often employed to increase the driving force for diffusion and induce bulk plasticity at the interface. Through this technique, it is possible to join materials below their melting temperature to protect temperature-sensitive microstructures and to join material

combinations that could not be achieved through liquid-phase-based techniques. However, because of its reliance on solid-state processes, even under ideal conditions, high joining temperatures and lengthy processing times (on the order of hours to tens of hours) are often required. The high applied pressures can also cause deformation, requiring further machining after bonding. While diffusion bonding can produce strong bonds for use at a wide range of temperatures, the additional processing demands make it a poor choice for all but the most specialized of applications.

Brazing, by contrast, is a widely used technique for joining ceramic components. It relies on a liquid-metal film between two ceramic components or a ceramic and a metal component. When the braze solidifies, it bonds the two components. Since brazing is a diffusionless process, the joining times are quite short, on the order of seconds or minutes, and thus the processing time is minimal. The braze is chosen so that it wets the interfaces of the two components, allowing it to spread across the interfaces and flow into and fill any interfacial gaps and voids on the surfaces. This minimizes the amount of surface preparation needed prior to joining. However, the ability of the braze to wet and spread across the ceramic interface is not always achievable without the addition of a reactive element to the braze, which causes the formation of reaction products, and can significantly lower the strength of the bonded assembly. In addition, since the liquid phase must be taken above its melting temperature, the use temperature for brazed materials is inherently lower than the bonding temperature. This means that for materials with sensitive microstructures or those that are to be used at relatively high temperatures, brazing is a poor technique.

In the past 20 years, partial-transient-liquid-phase (PTLP) bonding has emerged as a potential alternative to more traditional bonding methods. It combines some of the property advantages – high use temperatures and lower joining temperatures – of diffusion bonding with some of the processing advantages – less stringent surface-preparation and shorter bonding times – of brazing. As a result, PTLP bonds can be formed at temperatures well below the ultimate use temperature of the joint, using relatively short processing times (on the order of minutes to hours). However, due the addition of a transient-liquid phase, the inherent complexities of the bonding system increase, and each PTLP-bonded system must be chosen carefully to achieve the desired strength and properties. Recently, a number of investigations have focused on the success of Ni/Nb and Co/Nb interlayer systems to join Al_2O_3 ceramics[1-3]. While these successes have shown the viability of the PTLP technique using Nb interlayers to join Al_2O_3, the effect of changes in interlayer chemistry is less understood. The current study explores the effects of chemistry on the wetting characteristics of the liquid-phase layer, processing conditions, and the interactions between the liquid- and solid-phase interlayer components when using interlayers consisting of refractory metals other than Nb. Chapter 2 presents a selection of prior investigations that were the foundation of the current work. Chapter 3 presents the proposed approach of using surface-modified interlayers for PTLP bonding, and details the experimental procedures used in this study. Chapter 4 presents and discusses the results of the study. Chapter 5 summarizes the findings and the results are used to help develop a methodology for expanding the PTLP technique beyond the Al_2O_3 system.

2. Background

In a wide range of technologies, ceramic materials offer a number of advantages – low density, high melting point, good corrosion resistance, and high compressive strength – that make their use desirable. However, most ceramics are brittle in nature and have low fracture toughness. This severely limits the formability of ceramic components and causes many devices to employ ceramics as part of a larger assembly that contains dissimilar materials. Often, this means bonding metal and ceramic materials to one another. In order to produce bonds with high fracture strengths between dissimilar materials, two main criteria must be met. The bonds must have strong interfacial adhesion, and residual stresses introduced during the joining process must be minimized. In this section, several parameters necessary for the formation of successful metal/ceramic bonds are discussed.

2.1 Variables Affecting Bond Strength

2.1.1 Interfacial Contact and Adhesion

When attempting to bond two materials, a critical component of success is the ability to maximize the contact area of the bonded surfaces. Compared to the projected area of two solid surfaces, the area in contact can vary significantly when the contacting surfaces are rough. Several models have shown that the actual contact area between two surfaces is proportional to the applied pressure in both the case of plastically deforming and elastically deforming bodies[4,5]. In metals, the applied pressure will initially cause surface asperities to deform plastically, causing the contact area to increase until it is sufficiently large to support the applied pressure elastically[5]. However, Childs found that when bonding steels of a range of hardnesses, even when applied loads equivalent to very high hardness values (3× the hardness of the components) were used, work hardening caused the plastic deformation of the interface to stop before the surfaces had completely flattened[6]. This suggests applied pressure alone is not able to eliminate flaws and voids at the bonding interface, and other methods are needed to maximize the interfacial contact. There are two principle ways to further eliminate interfacial flaws in a bond: the first is to increase the temperature of the assembly to initiate solid-state diffusion processes, and the second is to introduce a liquid phase that spreads across the interface and fills any interfacial gaps and voids.

To successfully employ a liquid-phase bonding process, the liquid phase must wet the interface and spontaneously spread to fill any interfacial gaps and voids. Sessile-drop experiments, where a droplet of liquid is formed or placed on a solid substrate, are commonly used to determine the wetting characteristics of a liquid. Wetting is described by the contact angle that is formed at the liquid-solid-gas triple junction. For a non-reactive liquid on a flat, insoluble, rigid substrate, shown in Figure 2.1, the Young's equation expresses the equilibrium condition as a force balance between the surface tensions

$$\gamma_{SV} = \gamma_{SL} + \gamma_{LV}\cos\theta$$

where γ_{SV}, γ_{SL}, and γ_{LV} are the respective solid-vapor, solid-liquid, and liquid-vapor interfacial tensions, and θ is the contact angle of the liquid droplet. When $\theta < 90°$, the liquid is said to wet the solid, while when $\theta > 90°$, then the liquid is said to be non-wetting.

The contact angle can be used to determine the work of adhesion, W_{ad}, which is the amount of work needed to replace the solid-liquid interface with two free surfaces,

$$W_{ad} = \gamma_{LV}(1+\cos\theta).$$

In the absence of plasticity or other energy-dissipative processes, the work of adhesion is an indication of the "strength" of the interface. The higher the work of adhesion, the more energetically favorable the solid-liquid interface is to the formation of free surfaces. In a bonded system, the work of adhesion is assumed to be the minimum energy needed in order to fracture the interface. As the contact angle decreases, the work of adhesion increases. In addition, when $\theta < 90°$, the liquid-solid interface is energetically preferable to the liquid-vapor and solid-vapor interfaces, and thus the liquid will spontaneously spread between two parallel solid surfaces. Thus, using liquids that wet the surfaces to be bonded will help eliminate flaws along the surfaces and potentially lead to stronger interfaces. While attempts have been made to measure the relationship between W_{ad} and the bond strength, no clear conclusions were reached due to the energy dissipation caused by plastic deformation, the formation of residual stresses during cooling, and flaws forming at the interface[7,8].

At high temperatures, there are a number of factors that can cause variance in the measured contact angle: the roughness of the solid surface, the atmosphere of the furnace, and compositional changes due to diffusion. Diffusion in the solid substrate allows ridges to form at the triple line, due to the liquid's surface tension in the vertical direction, which is unaccounted for in Young's original equation. These ridges can change the local curvatures at the triple point, driving further diffusion and affecting the droplet's ability to spread across the interface[9]. The Smith equation describes the equilibrium relationship at the triple line between the three dihedral angles and the surface tensions.

$$\frac{\gamma_{LV}}{\sin\phi_S} = \frac{\gamma_{SV}}{\sin\phi_L} = \frac{\gamma_{SL}}{\sin\phi_V}$$

where γ_i is the surface tension and ϕ_i is the dihedral angle of phase *i*. In sessile-drop experiments, the liquid droplet forms rapidly, in less than a second. When measured $<10^3$ s after the droplet melting, the measured contact angles are typically similar to those predicted using Young's Equation. However, after $10^3 - 10^5$ s, ridges formed in the solid can be of sufficient height to alter the contact angle[10]. In liquid-phase joining, the time needed for the liquid to fill interfacial gaps is on the order of seconds, well below the time needed for significant ridging to occur, so the Young's contact angle is a relevant predictive tool to determine the ability of a liquid to wet the bonding interface.

Just as the roughness of the bonding surfaces can prevent complete interfacial contact, it can also affect the apparent contact angle of a liquid as it spreads across the interface. While neither the interfacial energies nor the Young's contact angle are changed by surface roughness, the effect on the apparent contact angle can be quite large. Wenzel was one of the first to attempt to model this phenomenon[11,12]. By placing a droplet of water on a saw-tooth surface where the spacing between the saw-tooth peaks was much smaller than the size of the droplet, he determined that the Young's contact angle, θ, and the observed contact angle, θ_W, were related by

$$\cos\theta_W = s_r \cos\theta \ ,$$

where s_r is the ratio of the actual surface area to the projected surface area and is always ≥ 1. Wenzel's results concluded that when Young's contact angle, $\theta > 90°$, the observed contact angle will increase as s_r increases. By contrast, when $\theta < 90°$, the observed contact angle will

decrease as s_r increases. However, since its initial publication, Wolansky and Marmur[13] have shown that Wenzel's relationship is only mathematically valid when the size of the droplet is infinitely larger than the length scale of the surface features. In addition, Wenzel assumes that the liquid will penetrate and fill all surface features, when in reality voids can form at the interface[14]. Figure 2.2 shows the surface of a solid covered in a liquid phase with a single unfilled, saw-tooth flaw. The change in interfacial free energy, δF_s, for a displacement of liquid, δl, into the flaw is

$$\delta F_s = -2\gamma_{LV}\cos(\phi)\delta l + \frac{2\cos(\theta)\delta l}{\gamma_{LV}} \quad .$$

At the equilibrium configuration, $d(\delta F_s)/d(\delta l) = 0$, the critical flaw angle, ϕ^*, is

$$\phi^* = 180° - \theta$$

When $\phi < \phi^*$, the liquid is able to spontaneously flow into and fill the flaw, while when $\phi > \phi^*$ it does not. This suggests that for a rough surface with a wide range of flaw sizes, when $\theta \leq 90°$, the liquid flows into and fills any interfacial flaws, while when $\theta > 90°$ the microscopic geometry of the flaw will determine whether the liquid is able to fill it entirely.

As the liquid phase attempts to reach its equilibrium configurations, such as when the droplet initially melts or is placed onto the substrate's surface in a sessile-drop experiment, sharp features on the surface can pin the triple line in place and arrest its movement across the surface. In a pinned orientation, the liquid may have a range of observable contact angles[9]. As a result, contact-angle hysteresis is commonly observed in real systems, where the observed contact angle of an advancing liquid front is different from that of a receding liquid front[15]. To better determine the relationship between surface roughness and contact angle, Bartlow developed a model describing the energetically favorable contact angles for a liquid placed on a rough surface[2]. By fixing the liquid volume and moving the location of the triple line across the surface, the overall energy of the system was calculated for a range of configurations, and the contact angles that minimized the overall energy were identified. It was found that while the macroscopic contact angle roughly followed the Wenzel's model as the surface roughness factor, s_r, increases, both the local and macroscopic contact angles could vary significantly due to pinning. Moreover, when a fractal surface roughness was used, the measured contact angles on opposing sides of the droplet could differ significantly.

While the substrate surface topography can alter the observed contact angle of a liquid droplet, the inherent surface energies of the system – and, by extension, the composition of the liquid droplet and solid substrate – play the largest role in determining the contact angle. For the wetting of liquid-metal droplets on ceramics, metals are described to be either reactive or non-reactive. Reactive metals have dramatically lower contact angles compared to non-reactive metals. On ceramic substrates, non-reactive metals such as Au, Ag, Cu, and Sn have contact angles, $\theta > 100°$ [16]. Ni has a contact angle, $\theta > 100°$ on Al_2O_3 substrates[7,17-24]. Reactive metals, such as Zr, Ti, or Cr can be added to non-reactive metals and lower the contact angle by forming a reactive layer (an oxide, carbide, or nitride phase), by forming a reaction product layer (e.g., an oxide, carbide, or nitride layer)[25,26] or by adsorption at the interface[21,23]. The quantity of reaction product formed will vary with the processing conditions.

2.1.2 Residual Stresses

In ceramic/metal/ceramic bonds that undergo thermal cycling, either during use or during the bonding process itself, the coefficients of thermal expansion (CTE) of the individual components have a large impact on the strength of the bonded assembly. During the bonding cycle, residual stresses can develop near the interlayer due to CTE mismatch between the components. Cao and Evans developed a model for ceramic cylinders bonded using a thin metal interlayer[27]. During the bonding process, when the CTE of the metal interlayer, α_{metal}, was larger than that of the ceramic, $\alpha_{ceramic}$, (which is typical in ceramic/metal assemblies), the ceramic component developed regions of both tensile and compressive residual stresses during cooling. At the perimeter of the bonded sample, the ceramic had a thin region of tensile stress perpendicular to the interlayer near the ceramic/metal interface, as shown in Figure 2.3a. Since most structural ceramics are inherently non-ductile, any regions of residual stress can act as initiation points for crack formation, which can lead to a significant decrease in strength of the bonded assembly. Moving inward radially away from the edge of the bonded assembly, the magnitude of the stress decreases significantly, as shown in Figure 2.3b. This suggests that flaws and cracks near the surface will have a larger impact on the strength of the sample.

2.1.3 Elastic Mismatch and Interlayer Plasticity

As the residual stress, $E\Delta\alpha\Delta T$, increases – where E is the modulus of the metal interlayer, $\Delta\alpha$ is the difference in CTE between the metal and ceramic constituents, and ΔT is the difference between the bonding and room temperatures – the stresses in the metal interlayer can exceed σ_0, the uniaxial yield stress of the interlayer. As the residual stress approaches σ_0, the metal interlayer transitions from behaving in an elastic manner to a plastic-elastic manner, as shown in Figure 2.4. In addition, when an external stress is applied to the bonded assembly, such as during 4-point bend testing, mismatch between the coefficients of elasticity of the bulk ceramic and the metal interlayer can induce stresses $1–6\times \sigma_0$ within the interlayer, inducing further plastic deformation[28]. During mechanical testing of a typical ceramic/metal/ceramic assembly, the plasticity induced in the interlayer can effectively eliminate the residual stress field due to CTE mismatch. This is beneficial, as localized plasticity minimizes stress concentrations within the interlayer[28-30]. As shown in Figure 2.5, He *et al.*[28] found that to propagate a crack near the bonded interlayer, the normalized energy release rate, G/G_b, where G is the energy release rate for the bonded sample and G_b is the energy release rate for a monolithic ceramic sample, reaches a maximum value and then decreases as the applied stress, σ, increases beyond σ_0. Thus, for ceramics bonded using a metal interlayer, the stress state of the interlayer is mainly dependent on the elastic-plastic relationship between the ceramic and metal. Thus, using a metal that has a low σ_0 can minimize the magnitude of both the interlayer stresses and the tensile stresses that form in the ceramic near the interlayer[28-30].

2.2 Traditional Bonding Techniques

2.2.1 Diffusion Bonding

Solid-state diffusion bonding relies on diffusion mechanisms and local deformation processes in order to eliminate gaps and voids along the interface of the two materials being

joined. When joining ceramic materials, metals are often employed as the interlayer material as metals are generally ductile and can more easily plastically deform to fill interfacial gaps and voids. The benefit of the diffusion-bonding process is it can produce robust bonds that are stable at high temperatures, and it can be used to bond material combinations that could not be joined using liquid-state bonding techniques, such as noble, refractory, and non-reactive metals[31-37]. To activate the diffusion mechanisms for bonding, processing temperatures for diffusion bonding are typically 0.5 – 0.9× T_m of the more ductile phase, typically the metal interlayer. The joining system can be chosen so that the metal interlayer has a higher melting temperature than the ceramic, minimizing creep and allowing the bonded system to operate at higher temperatures than the bonding temperature, such as in the case of Al_2O_3/Nb systems[31]. However, because the joining process relies on diffusion mechanisms, long processing times (≥10 h) are often needed to ensure proper adhesion and the elimination of voids at the interface. To increase the driving force for diffusion, to induce plastic flow, and to break down surface oxides, high applied pressures (≥10 MPa) are typically used[38]. In addition, the initial surface roughness strongly influences the final cohesion of the interface, and stringent surface preparation is required to reduce the initial void size and increase interfacial contact[39,40].

A number of models have been developed in order to better understand the void-reduction mechanisms for diffusion bonding[41-45]. To reduce the complexity of the problem, all of the models assume that plastic deformation occurs until an array of channels of uniform cross-section is produced, allowing the authors to use 2-D cross sections in their analyses. Wallach *et al.* assumed that an array of parallel diamond-shaped[42,43] or elliptical[46] channels were present. Argon[44] assumed an array of channels that had both short- and long-wavelength roughness by superimposing a short-wavelength, sawtooth-shaped profile upon a sinusoidal, longer-wavelength curve. While porosity was initially eliminated by plastic deformation, as bonding progresses it was found that volume diffusion dominates the elimination of the remaining pores at the interface. The diffusion mechanisms were analogous to those found in pressure-sintering models[47-52]. As an example, Reimanis showed that for single-crystal Al_2O_3 diffusion bonded with Nb, the bond front was found to grow and fill interfacial gaps. The fronts would meet to form pore channels, which subsequently broke into smaller pores and eventually disappeared[53].

Three main variables affect the strength of diffusion bonds: the applied pressure, the bonding temperature, and the time at temperature. As the applied pressure is expected to induce plastic flow, higher pressures usually correlate with higher bond strengths. Numerous studies have shown that this is true to a limit; however, at high enough pressures all the interfacial voids are filled and/or no more plastic deformation can occur due to work hardening[34,54-57]. Thus, after a sufficiently high pressure is applied, bond strength will become independent of the applied pressure, and diffusion mechanisms are needed to close any remaining interfacial voids.

Diffusion is influenced by both the bonding temperature and the holding time during the bonding process. As the bonding temperature is increased, plastic flow is activated and the amount of diffusion that occurs also increases, decreasing the size and amount of interfacial voids. In general, for a fixed bonding time, the bond strength increases as the bonding temperature is increased[37,58]. The bond strengths of Al_2O_3 joined using Cu, Au, and Pt interlayers have all been found to increase as the bonding temperature is increased for a fixed

holding time, and when the bonding time was increased for a fixed bonding temperature[32,34,59]. However, this is not universally true. In some cases, peak strengths are observed at intermediate bonding temperatures[37,56,60]. In these systems, higher bonding temperatures led to an increase in the residual stresses that formed during cooling, causing the bond strength to decrease. Intermediate bonding temperatures and times also tend to produce the highest bond strengths when ceramics are bonded using reactive metals. In these systems, sufficient diffusion must occur to allow a chemical bond to form at the interface. Once chemical bonding occurs, continued diffusion can lead to the formation of reaction layers along the interface, which introduce residual stresses into the bond assembly and act as a weak layer for crack propagation. When bonding Al_2O_3 with Ti interlayers in vacuum, a Ti_3Al intermetallic was found to form along the interface[61-64], which increased in thickness with increasing bonding time, resulting in progressively decreasing bond strengths[65]. Thus for components diffusion bonded by reactive metals, the bonding time and temperature must be chosen to limit the continued growth of any mechanically detrimental reaction phases, including during the usable lifetime of the bonded assembly. Because of the stringent processing conditions and long processing times, diffusion bonding is typically used for specialized applications.

2.2.2 Brazing

In brazing, an interlayer that is compositionally distinct from the materials being joined is melted at the interface and allowed to cool. Brazing allows for short processing times, less-stringent surface preparations[66] and depending on the interlayer selected, low processing temperatures and pressures. As a result, brazing has lower costs and higher throughput than diffusion bonding. Brazing relies on the molten interlayer to flow into and fill interfacial gaps and voids, a diffusionless process that can reduce the bonding time to the order of minutes or seconds. When brazing ceramic materials, metals or metal alloys are typically used as the interlayer to reduce the bonding temperature. However, molten metals typically do not wet ceramic surfaces well, which can lead to unbonded regions remaining at the interface of a brazed component, reducing the assembly strength.

Metallization of the ceramic surface is one method of improving the wetting and adhesion characteristics of the liquid phase[55,59,67,68], but this process requires multiple steps at high temperatures, which increases costs and can potentially damage sensitive-microstructure components. Active-metal brazing is another method used to alter the wetting characteristics of the braze material on the ceramic components. Alloys containing small amounts of Ti, Zr, or Hf have been developed, where the active metals can form oxides, carbides, or nitrides at the braze interface[69,70]. Care must be taken during the braze-selection process. Thicker reaction layers can be brittle or contain microstructural flaws, and if internal stresses are present, the reaction layers can act as weak layers in which the joints can fail[71,72]. CTE mismatch between the braze material and the ceramic components can lead to the formation of residual stresses during cooling, decreasing the assembly strength. The residual stresses that develop are typically large enough that it is often assumed that the residual stress is equivalent to the yield stress of the braze material[73]. In addition, above 50% of the brazes' T_{melt}, the braze material can begin to soften significantly, limiting the feasibility of brazing for assemblies that will be used at higher temperatures[74,75]. Despite these shortcomings, brazing is a rapid and

cost-effective technique for bonding ceramic components, and is often used in high-volume production.

2.3 Partial-Transient-Liquid-Phase Bonding

2.3.1 Prior Work on Transient-Liquid-Phase Bonding

Partial-transient-liquid-phase bonding (PTLP) was developed as a method to join ceramic components and is an extension of the transient-liquid-phase (TLP) bonding technique. TLP bonding was developed to join high-temperature alloys that could not be joined using more conventional methods. As is described elsewhere[76-80], the TLP bonding of a sandwich structure employs an interlayer that contains a melting-point depressant (MPD). During joining, the MPD causes the interlayer to form a liquid phase, dissolving a portion of the base metal and surface oxides in the process[80,81]. Simultaneously, the MPD begins to diffuse into the base metal. The removal of the MPD from the liquid causes a reduction in the amount of liquid, and eventually the entire interlayer isothermally solidifies. The MPD will continue to diffuse through the base metal until the bonded assembly is cooled or homogenization of the MPD in the base metal is attained. Ideally, once homogenized, the interlayer should have the same chemical composition as the base metals, allowing the joint to have properties that are indistinguishable from that of the bulk.

TLP bonding is typically used to join various high-temperature components in heat exchangers and turbine engines, in particular with Ni-base superalloys. B and Si are the typical MPDs used. B is the most common as it diffuses quickly and is effective in depressing the melting point[82]. However, the isothermal solidification time is highly dependent on the diffusion rate of B in the base alloy. To join Ni-Cr, Ni-Cr-Co, and NiAl alloys, bonding times of 24 – 72 h were required[82,83], while only 2 h were required to join pure Ni [84,85]. In addition, isothermal solidification did not prevent the formation of intermetallic phases, such as Ni_3B, near the interface. These intermetallics are typically detrimental to the mechanical properties of an assembly[86]. To prevent the formation of these intermetallic phases, even longer processing times would be required to allow for homogenization of the MPD in the bonded assembly.

To reduce the processing times for TLP bonding, a number of approaches can be taken. Improved surface preparation of the joining interfaces reduces the surface roughness and decreases the amount of liquid needed to fill interfacial gaps and voids. In turn, the decrease in the amount of liquid necessary reduces the initial amount of MPD needed, leading to shorter isothermal solidification times. However, this increases the number of processing steps and subsequently the cost. Raising the bonding temperature can accelerate diffusion of the MPD, but this typically increases the amount of liquid that is formed and can be detrimental to the bulk microstructure. Finally, an applied pressure can be added to reduce the gap width, and thus reduce the amount of liquid needed, but again this adds processing steps and equipment, which can be cost prohibitive. Ultimately, the processing time for TLP bonding is controlled by the MPD diffusivity-solubility product, and determining the most suitable processing conditions for different material combinations is a difficult endeavor.

A number of models have been developed to better determine processing conditions for TLP bonding. Early efforts focused on determining the isothermal-solidification time, which is typically the rate-limiting step. In an attempt to model the net flux rate of the MPD

across the solid-liquid interface, Lynch *et al.* determined that the solidification rate was inversely proportional to square root of the isothermal holding time, $t^{1/2}$, which was verified in subsequent studies[79,87-89]. Several analytical solutions have been developed as well[77,90]. Tuah-Poku *et al.* determined an analytical solution for the isothermal solidification time, showing that

$$t = \frac{\pi W_o^2}{16 D_s}\left(\frac{C^{\beta}}{C^{\alpha_L}}\right)$$

where W_o is the initial interlayer width, C^{β} is the solidus composition, C^{α_L} is the liquidus composition and D_s is the MPD diffusivity in the base metal[79]. When this analytical solution was compared to results from extrapolated experimental data for a Ag/Cu/Ag bonded assembly, the analytical model predicted a solidification time nearly an order of magnitude longer than was observed experimentally (1200 min vs. 200 min, respectively). This discrepancy was found in the Ag/Cu/Ag system for other analytical models as well[89].

There have been a number of possible explanations put forth as to why the analytical solutions differed from the experimentally determined isothermal solidification times. The amount of liquid may have differed from the predicted amount due to the actual gap width differing from the predicted value, or due to the formation of excess liquid, which flowed out of the gap and reduced the amount of MPD present at the interlayer. Tuah-Poku noted that during bonding, the initially planar surfaces developed grooves along the grain boundaries, which increases the interfacial area and the flux of the MPD into the bulk, potentially decreasing the solidification time[79]. Finally, none of the models accounted for the role of diffusion mechanisms other than lattice diffusion. At moderately high temperatures (T<0.7 T_{melt}), grain-boundary diffusivities are typically greater than their lattice equivalents by several orders of magnitude. For bonding Ni, several studies have shown that the solidification time decreased when smaller-grain-size Ni was bonded[91,92]. In addition, migrating grain boundaries have also been shown to increase the solute flux, and thus to decrease the isothermal solidification time[93-98]. In a study bonding single-crystal Ni, the isothermal-solidification time was found to be in agreement with the calculated values, suggesting that grain-boundary diffusion has a large effect on the solidification time, and that all the liquid was retained at the gap during bonding[92,99].

2.3.2 Partial-Transient-Liquid Phase Bonding

TLP bonding combines the strengths of both brazing and diffusion bonding as it allows for joints to be made in relatively short time periods and at relatively low bonding temperatures, while allowing the final assembly to have a relatively high use temperature. While it would be desirable to use the TLP bonding technique to join ceramic assemblies, in practice it is unfeasible due to the low diffusivities of potential MPDs in ceramic components. As a result, the TLP bonding methodology was adapted to develop partial-transient-liquid phase (PTLP) bonding using multilayer metallic interlayers to join ceramic materials. The multilayer interlayer for PTLP bonding consists of a thin, MPD cladding layer on both sides of a thicker, higher-T_{melt} core material. In contrast to TLP bonding, the MPD in PTLP bonding diffuses into the core, and not into the surrounding bulk material, as the interlayer isothermally solidifies.

Figure 2.6 shows a schematic of a simplified PTLP bonding process for an interlayer system with a lens-type phase diagram. The multilayer interlayer is placed in a sandwich-type assembly between two ceramic components, and heated to T_{join} (Figure 2.6a). The increase in temperature causes interdiffusion between the core and MPD cladding layers, forming a transient-liquid phase at the ceramic interfaces at the liquidus composition of the phase diagram. At T_{join}, the MPD continues to diffuse into the core, maintaining the solidus composition at the liquid interface (Figure 2.6b). As the total amount of the MPD is well below its solubility limit in the core, it continues to diffuse into the core layer, causing a reduction in the amount of liquid, until the interlayer has isothermally solidified (Figure 2.6c). After solidification, the MPD will continue to homogenize in the core layer until the assembly has either fully homogenized or is cooled (Figure 2.6d). The re-melting temperature of the resultant joint exceeds the original joining temperature, T_{join}. In this simplified example it is assumed that there is minimal chemical interaction between the interlayer and the ceramic. As a result, diffusion is limited to within the interlayer. In other systems different scenarios are possible, such as the MPD layer forming a transient-liquid through dissolution of the ceramic. This adds components to the relevant phase diagram, and additional complexity to the design process.

There are a number of factors that need to be taken into account during the materials selection process for PTLP bonding. In an ideal system: the MPD will combine with the core to form a liquid-phase at a relatively low temperature, the liquid phase will wet the ceramic interface, the MPD will have a high diffusivity in the core, the homogenized MPD will form a complete solid solution with the core material at the bonding temperature, and the cladding/core combination will not react with the base material to form a secondary phase at the interface. In the case where all of these criteria are met, strong bonds can be formed while minimizing processing times and bonding temperatures. The minimal joining temperature is one at which the liquid phase can form while the core and MPD also form a complete solid solution. The minimal joining time is the amount of time necessary to incorporate all of the MPD into solid solution with the core material, and is dependent on the MPD's solubility-diffusivity product in the core. However, in real systems it is not always possible to satisfy all of these requirements simultaneously. Fortunately, not all of these requirements must be met in order to have successful PTLP bonding. For example, high-bond strengths can still be achieved despite the formation of secondary phases[1]. In these cases, the interlayers must be designed to mitigate the impact of secondary-phase formation through careful control of processing conditions and the core and cladding quantities.

The minimum amount of MPD cladding needed is determined by the amount of liquid that is necessary to fill interfacial gaps and voids. The mechanical properties of the joints are partially determined by the amount and size of flaws at the interface[100,101]. The initial transient-liquid thickness must account for diffusion during heating, so that the desired amount of liquid remains to flow into and fill interfacial gaps and voids when the liquid-forming temperature is reached. On a metal substrate, all metals form an acute contact angle, $\theta_m < 90°$; however, on most ceramic substrates, most non-reactive metals form an obtuse contact angle, $\theta_c > 90°$. During PTLP bonding, the liquid phase is in contact with both a ceramic bulk and the metal core. In the ideal case where both interfaces are parallel and flat, the liquid would spread and wet the interface when $\theta_m + \theta_c < 180°$ [102]. When $\theta_m << 90°$ this

means that the liquid can spontaneously spread continuously along the interface even in cases where $\theta_c > 90°$. However, in real systems the presence of surface roughness and flaws at the interfaces can result in more stringent requirements for wetting to occur at the interface. Along the ceramic surface, such as in Figure 2.2, it may require an applied pressure to fill flaws, depending on ϕ, when $\theta_c > 90°$. Bartlow showed that depending on the specific combination of surface roughness and contact angle parameters, wetting of the interface could either be enhanced or impeded[2]. If the core–cladding combination is chosen appropriately and the liquid phase successfully flows into and fills interfacial gaps and voids, it eliminates the need for reactive metals, while allowing for less-stringent surface preparation.

Unlike TLP bonding, in PTLP bonding the ceramic is not necessarily involved in the dissolution and solidification process. This is advantageous in that it minimizes the diffusion distance for interlayer homogenization compared to TLP bonding, since diffusion is contained entirely within the interlayer. However, since the core of the interlayer remains after bonding, TLP bonded assemblies have near uniform properties across the entirety of the assembly, while PTLP bonding results in a ceramic/metal/ceramic sandwich structure. As a result, in PTLP bonding the interlayer must have a CTE similar to that of the ceramic bulk in order to minimize the formation of residual stresses during cooling or thermal cycling of the component. Ceramics are more resistant to crack propagation in compression rather than tension, so ideally any residual stresses that are present should attempt to put the ceramic component in compression. In practice, regions of both compressive and tensile stress will occur in the ceramic as long as the CTE of the ceramic and metal components are not equal[27]. Thus choosing an interlayer that minimizes the formation of residual stresses is important.

2.3.3 *Prior Work on Partial-Transient-Liquid-Phase Bonding*

PTLP bonding has been used to join both oxide and non-oxide ceramics. As a precursor to PTLP bonding, Si_3N_4 was successfully bonded by Iino and Taguchi at 950°C using Ni/Nb/Ni and Nb/Ni/Nb cladding/core/cladding interlayers, a temperature well below the typical value for diffusion bonding of Si_3N_4 [103]. Subsequently, Ti/Ni/Ti [104], Au/Ni-22Cr/Au [105] and Cu-Au/Ni/Cu-Au [106] interlayers were all successfully used to PLTP bond Si_3N_4. In mechanical testing, the latter interlayer was found to have bond strengths approaching that of bulk Si_3N_4. SiC was also successfully bonded using the Ti-Cu-Au/Ni/Ti-Cu-Au interlayer, but with fracture strengths half those of bulk SiC [107].

Glaeser *et al.* explored the potential for PTLP bonding of Al_2O_3 substrates. Cu/Pt/Cu [100] and Cu/Ni/Cu [101] interlayers were both successful in producing bonded assemblies, with respective fracture strengths of 160±55 MPa and 160±63 MPa. The cladding-core systems were chosen for their ability to form a liquid phase in equilibrium with the solid core at the joining temperature. This prevented the formation of any mechanically detrimental intermetallics during the bonding process. With a peak bond strength of 267 MPa for the Cu/Ni/Cu system, compared to the ~280 MPa strength of the Al_2O_3 bulk, the interlayer was promising but the majority of the samples failed at much lower strengths. On examination of the fracture surfaces, unbonded regions were observed.

Analogous to active-metal brazing techniques, reactive metals were added to the interlayer system to help improve the wetting angle of the liquid. It was found that at 1150°C,

the addition of 6% Cr lowers the contact angle of Cu to 67° on an Al_2O_3 substrate. Using a revised interlayer composition of Cu/(80-wt% Ni-Cr)/Cu improved the strength to 227±19 MPa, with a portion of the higher-strength bonds failing in the ceramic[106,108]. PTLP bonding of the commercially-available, active-metal Ag-Cu brazing alloys Cusil-ABA and Ticusil were also found to produce high fracture strengths. When joining a high-purity Al_2O_3 with a bulk fracture strength of 359±52 MPa, In/Cusil-ABA/In interlayers produced bonds with strengths of 276±102 MPa, while In/Ticusil/In interlayers had bond strengths of 350±45 MPa. These PTLP bonds were fabricated at temperatures between 600–700°C, well below the 800-900°C temperatures required to braze using these alloys[72].

2.3.4 Bonding of Al_2O_3 Using Nb-Based Interlayers

To take advantage of the high melting points of ceramics, when selecting materials for PTLP bonds it is desirable to have an interlayer that also has a high melting temperature. Because of their high melting temperatures, refractory metals are attractive core materials for the bonding of ceramics. Since bonded assemblies that are used at high temperatures typically go through thermal cycling, it is desirable to minimize the CTE mismatch between the ceramic bulk and interlayer in order to minimize the formation of residual stresses in the assembly. Figure 2.7 shows the CTE over a range of temperatures for a number of refractory metals, and compares them to the CTE of a selection of advanced ceramic materials. The values are a close match, increasing the appeal of refractory metals for bonding ceramic materials.

The idea of using refractory metals to bond ceramics is not new. Al_2O_3/Nb is found extensively throughout the literature as a model system to study metal/ceramic bonding[53,109-111]. These constituents have a low CTE mismatch of ~0.6×10^{-6} K^{-1} and good chemical compatibility[112]. Diffusion bonding studies involving single-crystal Al_2O_3/single-crystal Nb [112], single-crystal Al_2O_3/polycrystalline Nb [53], and polycrystalline Al_2O_3/polycrystalline Nb [113] have all been explored. In these studies, as the bonding temperature was increased the fracture strength was found to increase due to an increase in the fraction of the interface that bonded, though the mechanism for void closure was not universal[114]. Gibbesch and Elssner found that when using 2-mm-thick Nb interlayers under a 10-MPa pressure, plastic deformation caused the closure of interfacial voids and pores when bonding between 900–1500°C [31]. However, using 100–200-μm-thick, single-crystal Nb interlayers bonded at 1450°C with pressures up to 2 MPa, Reimanis found that the volume diffusion was the dominant void removal mechanism, and the rate of removal was similar for assemblies annealed with and without applied pressures[53]. The interlayers used by Reimanis *et al.* were an order of magnitude thinner than those used by Gibbesch *et al.* and as a result would have been more constrained against plastic flow, potentially explaining the change in void-removal mechanisms. While successful bonds could be formed, McKeown *et al.*[113] found that even with bonding pressures of 2.2 MPa for 6 h at 1400°C, all of their diffusion-bonded samples failed at the interface at strengths of 130±20 MPa, well below the average strength of monolithic Al_2O_3, ~260 MPa.

In an attempt to broaden the range of potential interlayer architectures available to bond ceramic components, liquid-film-assisted joining (LFAJ) was developed. LFAJ is similar to PTLP bonding; however, in LFAJ the liquid phase does not isothermally solidify and

instead solidifies at the interface during cooling. LFAJ has been used to successfully bond Al_2O_3 using Cu/Nb/Cu interlayers. During bonding, the Cu dewets and acts as a diffusion path for the Nb to bond with the Al_2O_3, helping to increase the bonded area at the interface. Decreases in the Cu cladding thickness from 3.0 μm to 1.5 μm decreased the overall bond strength[102,115], most likely due to insufficient liquid to fill interfacial gaps and voids. The bonding temperature had a large effect on the fracture strength, as assemblies bonded at 1150°C had fracture strengths ~81 MPa, while those bonded at 1400°C had fracture strengths of ~241 MPa. However, over 30% of the bonds failed at the interlayer[116].

More recently, high-purity Al_2O_3 bonds that failed exclusively in the ceramic bulk have been fabricated using Ni/Nb/Ni interlayers. Ni-Nb has a eutectic temperature of 1184°C, as seen in Figure 2.8, which is well below the typical diffusion-bonding temperatures of 1400–1700°C for Al_2O_3/Nb diffusion bonding. At 1280°C, Nb can incorporate 4.5-at% Ni in solid solution, and at temperatures ≥1280°C, the liquid phase has a composition of ≥53-at% Nb, meaning that the minimum liquid-film thickness will be double that of the Ni cladding thickness. As a result, less Ni is needed to produce the quantity of liquid needed in order to fill in any interfacial flaws and voids, which will lead to reduced isothermal solidification times. In addition, Ni is an anomalously fast diffuser in Nb, reducing solidification times[45,117,118]. While pure Ni has a contact angle of ~110° on Al_2O_3 [7,17-24], 61-at% Ni-Nb alloy was found to have a contact angle of ~90° [3]. Because of this, the liquid phase should flow easily along the metal/ceramic interface during PTLP bonding, and should fill any interfacial flaws on the bonding surfaces. In fracture tests of Al_2O_3 PTLP bonded at 1400°C using Ni/Nb/Ni interlayers under a 2.4-MPa pressure, the resultant bonds were found to fail exclusively in the bulk ceramic, and have bond strengths of 510±120 MPa, which was equivalent to the strength of the bulk material, 530±90 MPa, using isothermal holding times as short as 5 min [3]. Optical microscopy revealed no evidence of flaws and voids remaining at the interface. Microchemical analysis of the bonded assembly revealed that ~80% of the Ni-Nb liquid was extruded from the interface during bonding, allowing the interlayer to form a solid solution during the bonding process, with no presence of intermetallic Ni_6Nb_7 at the interface.

Reynolds[119,120] further explored the role of processing pressure on the fracture strength of Al_2O_3 PTLP bonded using Ni/Nb/Ni interlayers. Bonding pressure was found to have a large influence on the homogenization of the interlayer. Using a 6.7-kPa pressure, it was found that none of the liquid phase was extruded during bonding; this resulted in a five-fold increase in liquid volume remaining at the interface compared to bonds produced using a 2.4-MPa pressure. As a result, a multiple-μm-thick layer of Ni_6Nb_7 formed at the bond interface. Where bonds manufactured with a 2.4-MPa bonding pressure failed exclusively in the ceramic bulk, a number of 6.7-kPa bonds failed at the interface itself due to the presence of the Ni_6Nb_7 layer. When bonding hot-isostatically-pressed (HIP), high-purity Al_2O_3, the average fracture strengths of the 6.7-kPa bonds decreased compared to 2.4-MPa bonds. In contrast, the fracture strengths were comparable using pressures of both 2.4 MPa and 6.7 kPa when bonding non-HIPed Al_2O_3. Halving the initial thickness of the Ni cladding was found to reduce the amount of Ni_6Nb_7 that formed at the interlayer, and when bonding HIPed Al_2O_3 the strengths of 2.4-MPa and 6.7-kPa bonds were comparable. However, thinner cladding layers were found to introduce more risk of failure, as one sample bonded at 6.7 kPa had a significantly reduced strength compared to the others. Upon further examination it was found

that the interface of that sample had large regions that remained unbonded after PTLP bonding was completed, suggesting that insufficient liquid phase was present at the interface to promote strong bonding. The amount of liquid necessary to fill the interfacial gaps and voids varies and is in part dependent on the roughness of the interfacial surfaces, which is difficult to quantify using current roughness measurement techniques[1].

While Ni/Nb/Ni interlayers have proved successful in producing high-strength Al_2O_3 bonds in short bonding times, it is evident that interlayer design and processing conditions play a large role in the final strength of the bonded assemblies. Ni/Nb/Ni interlayers are unique in that both the wetting properties and CTE of the interlayer are highly favorable for the production of strong ceramic bonds. This will not be true for all ceramic systems. In order to expand the PTLP bonding to a wider range of ceramic systems, a better understanding of how the processing conditions, the interlayer CTE, the interfacial wetting properties and the homogenization microstructure interact to ultimately determine the fracture strength of the bonded assembly is needed. By understanding which of these factors most influences the final strength of bonded assemblies, a better template can be developed to guide the design of future interlayer systems for the PTLP bonding of ceramic materials.

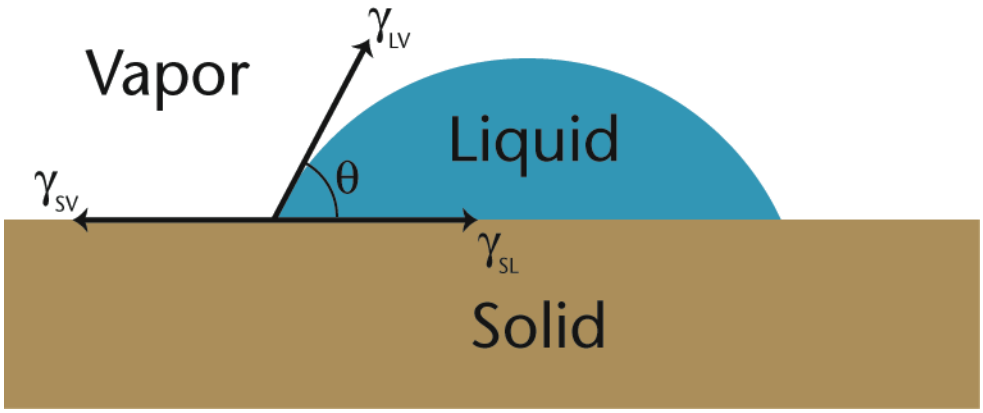

Figure 2.1: Triple-point intersection showing the dependence of liquid contact angle on the surface energies of the liquid-solid, liquid-vapor, and solid-vapor interfaces.

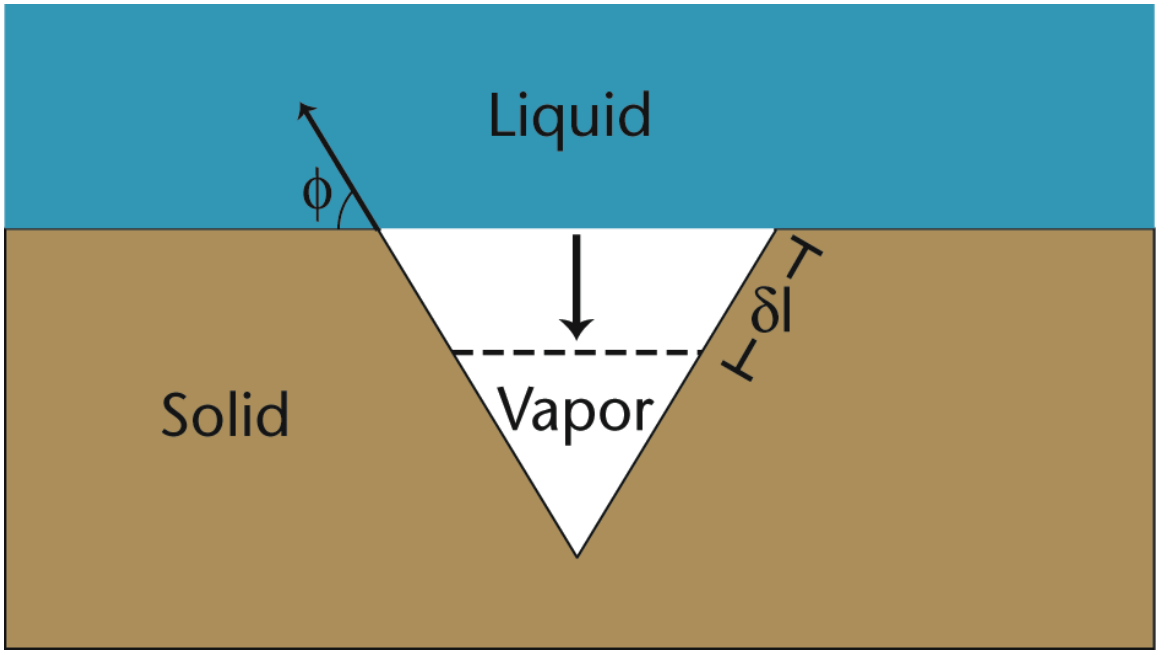

Figure 2.2: A liquid film entering a saw-tooth-shaped flaw.

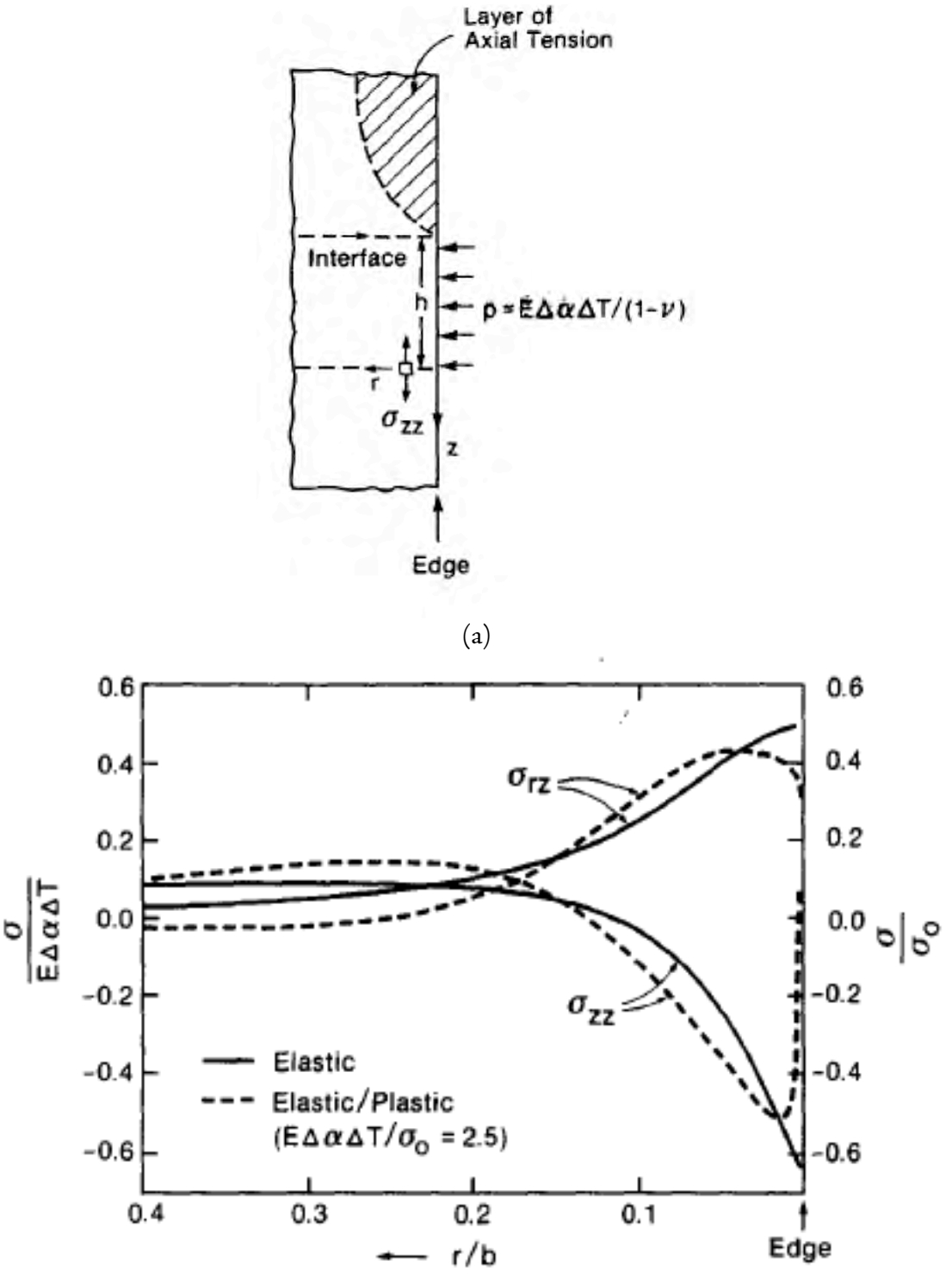

Figure 2.3: In a sandwich bond of two ceramics using a metal interlayer, where the $CTE_{metal} > CTE_{ceramic}$, (a) shows that a region of tension will exist in the ceramic component near the sample edge. (b) moving inward from the edge of the cylinder, the magnitude of the stresses decreases by a factor of 2-3× [27].

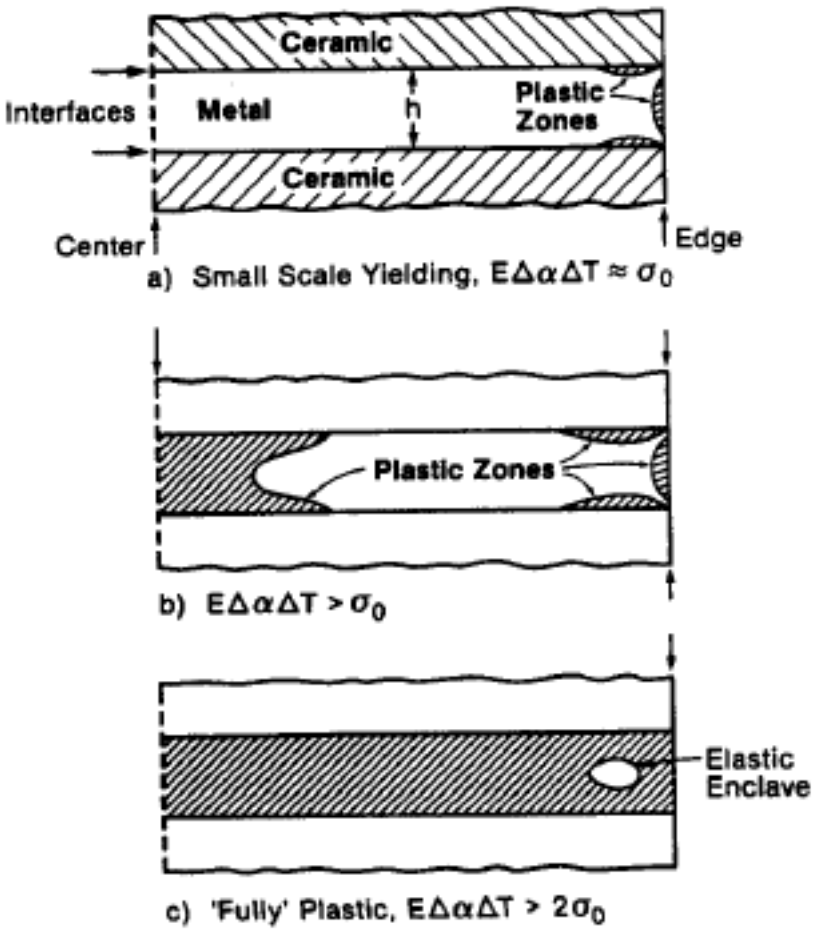

Figure 2.4: Induced plasticity in interlayer due to residual stresses (a) when the residual stress is equivalent to the uniaxial yield stress (b) when the residual stress is greater than the uniaxial yield stress, and (c) when the residual stress is greater than twice the uniaxial yield stress[27].

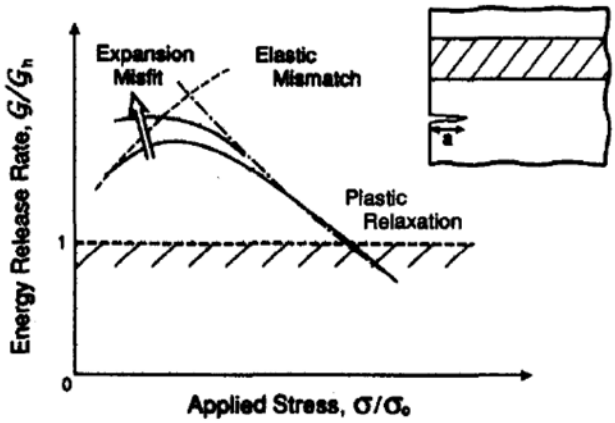

Figure 2.5: As the applied stress increases, G/G_h, initially increases due to CTE mismatch, before decreasing due to plastic deformation reducing the presence of stress concentrations within the interlayer[28].

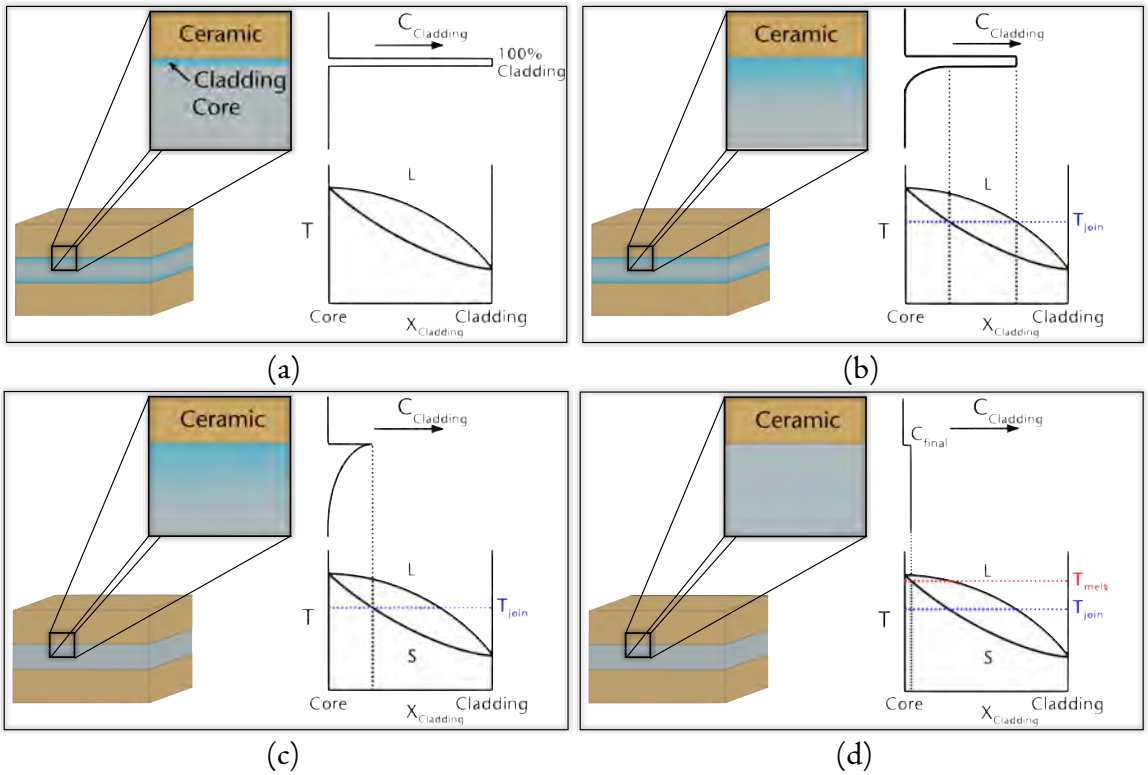

Figure 2.6: Schematic of PTLP bonding. (a) Initial assembly with multilayer interlayer consisting of a MPD cladding and a core between two ceramic components; (b) Assembly is heated to T_{join}, causing the cladding to melt; (c) As the MPD diffuses into the core, the joint isothermally solidifies. (d) The homogenized interlayer has a solidus temperature significantly higher than T_{join}.

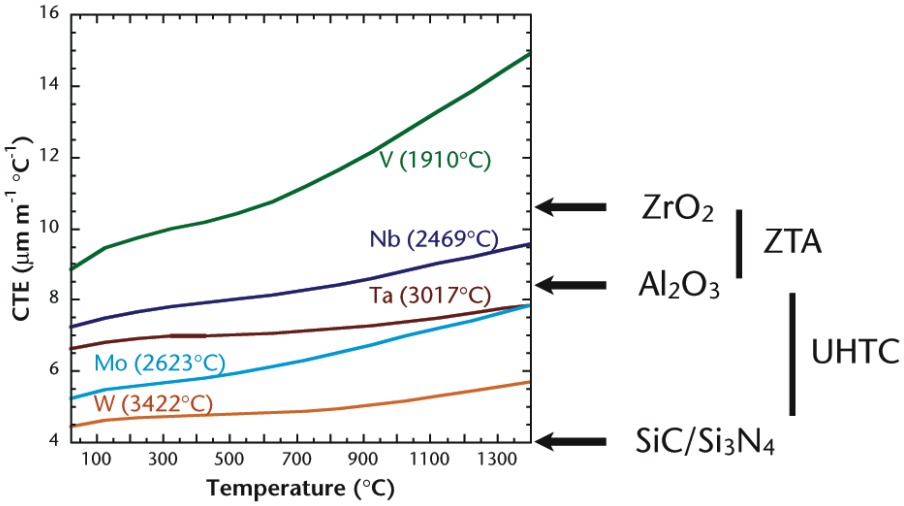

Figure 2.7: CTE vs. T for a number of refractory metals compared to the average CTE for a number of advanced ceramics, including various ZrO_2-toughened Al_2O_3 (ZTA) and ultra-high-temperature ceramics (UHTC)[121-124].

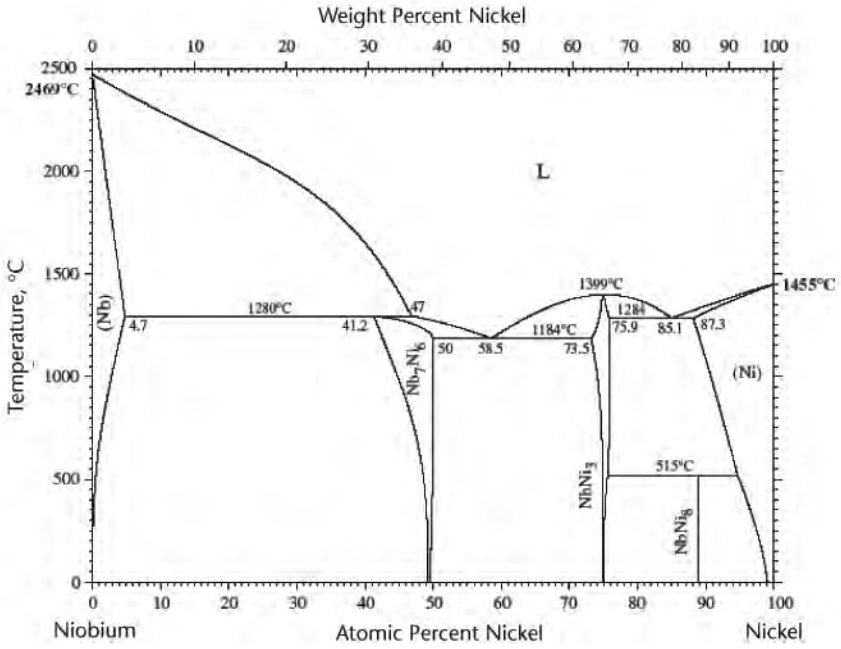

Figure 2.8: Ni-Nb binary phase diagram[125].

3. Experimental Approach and Procedures

3.1 Approach

It has been demonstrated that high-strength Al_2O_3 assemblies can be formed through PTLP bonding when the interlayer and processing conditions are properly selected. The use of Ni/Nb/Ni interlayers resulted in Al_2O_3 assemblies that failed exclusively in the bulk ceramic at bend strengths >500 MPa [3]. However, selecting an appropriate interlayer is a complex process that depends on a large number of factors. The wetting ability and the diffusivity-solubility product of the MPD cladding, the interlayer melting temperature, and the residual stresses induced during cooling as a result of CTE mismatch between the interlayer and the bulk ceramic all play an important role in the formation of successful PTLP bonds. Interactions within the interlayer itself further complicate the material-selection process. Changes in the initial core-layer composition alter the composition of the liquid that forms at the interface due to the dissolution of core material into the liquid. Redistribution of the cladding constituent and interlayer homogenization can alter the CTE of the entire interlayer.

As discussed in Section 2.3.4, the Ni/Nb/Ni interlayer system is unique in a few respects. Nb has a similar CTE to Al_2O_3 for the temperature range 25°C to 1400°C, as shown in Figure 3.1. The Ni-Nb liquid phase that forms during the bonding process has a relatively low contact angle on Al_2O_3, allowing the liquid to spread along the interface easily. This is fortuitous because the use of a pure-Nb core both minimizes the CTE mismatch and improves the wetting properties of the liquid-phase cladding when bonding Al_2O_3. However, for the majority of advanced ceramic materials, an equivalent core material to Nb does not exist that both minimizes CTE mismatch and gives the favorable wetting characteristics at the interface. Thus, when using a binary cladding/core interlayer, the effectiveness of PTLP bonding is compromised.

If the number of components employed in the interlayer is increased, the ability to tailor the interlayer to the system it is bonding will increase as well. Since a number of refractory metals form complete solid solutions with one another[126], it is possible to tailor the interfacial and core compositions by employing a surface-modified core layer during PTLP bonding. A surface-modified core is analogous to the homogenous refractory cores that were described in Section 2.3.2, with the exception that it has a thin, several-μm-thick coating of a second refractory metal B on both sides of the core. The MPD cladding, component A, is then deposited on the exterior of the surface-modified core. The processing for PTLP bonding using a surface-modified core is identical to that described in Section 2.3.2. Figure 3.2a shows the assembly prior to bonding. During bonding, component A will redistribute across the core, while the distribution of component B can range from homogenized to largely unchanged depending on the difference between the core and cladding diffusion rates[127]. An example of a final interlayer composition of components A and B is shown in Figure 3.2b. The presence of component B will predominately influence the composition and solidification of the liquid phase, while the composition of bulk core will influence the thermal stresses that arise from CTE mismatch. The benefits of varying the interface and core compositions independently are numerous. It allows for the composition of the interfacial liquid to be manipulated without large alterations to the interlayer CTE. It provides a method to explore the individual contributions of the interface and core to the overall fracture strength. It

explores the microstructural evolution of non-binary PTLP bonded assemblies. Finally, it presents a path for the extending PTLP bonding to a larger range of ceramic systems.

In this study, Al_2O_3 assemblies were bonded using different surface-modified cores and a Ni cladding to determine the effect of the interface and core compositions on the bond strength. The contribution of the core metal to ultimate bond strength was examined by creating surface-modified cores with V or Mo as the bulk of the core and Nb as the surface component. The notation, Ni/Nb/V/Nb/Ni, denotes the use of a Nb-surface-modified V core with a Ni cladding. These assemblies have a Ni-Nb-rich liquid at the interface, but with nominally the same CTE match as using a homogeneous V or Mo foil. To explore the contribution of the interfacial chemistry to the bond strength, the surface-modifying component was varied for a given core composition. For example, bonds fabricated using a Mo-surface-modified Nb core with a Ni cladding would be noted Ni/Mo/Nb/Mo/Ni. By comparing the fracture strengths of assemblies fabricated using a surface-modified core to those using a homogeneous core, insight can be gained into the interplay between interfacial adhesion, microstructural evolution and residual stresses in ceramic assemblies, which can be used to develop successful PTLP bonding systems for a wider range of advanced ceramics.

3.2 Substrates

3.2.1 Polycrystalline Substrates

Polycrystalline SSA-999W Al_2O_3, >99.9% pure and 98% dense with an average grain size of 1 μm, was obtained from Nikkato Corporation (Osaka, Japan). In addition, polycrystalline ZrO_2-toughened Al_2O_3 (ZTA), 15-wt% ZrO_2 with a grain size of 1.5 μm, was obtained from AstroMet (Cincinnati, OH). Both materials were in the form of blocks, 20 mm × 20 mm × 20 mm. One face of each block was ground flat using a succession of 75-μm and 30-μm grinding plates (South Bay Technologies, San Clemente, CA) on a Buehler grinding wheel (Evanston, Illinois). The ground face of the block was polished on a Logitech (Glasgow, Scotland) mechanical polisher using successively finer diamond suspensions (South Bay Technologies, San Clemente, CA) – 9 μm, 6 μm, 3 μm, 1 μm – and a colloidal-silica suspension (Struers, West Lake, OH). The blocks were ultrasonically cleaned in solutions of distilled water and soap, distilled water, acetone, and isopropanol for 15 min each, before being dried with a hot-air gun. Finally, they were air-annealed (CM elevator furnace, Bloomfield, NJ) for 1 h at 1000 °C to remove any residual organics.

3.2.2 Foils

For bonding experiments, 125-μm-thick foils of Nb (99.9-wt% pure), 125-μm-thick and 25-μm-thick foils of Mo (99.9-wt% pure), and 125-μm-thick and 12.5-μm-thick foils of V (99.8-wt% pure), were obtained from the Goodfellow Corporation (Malvern, PA). The foils were cut to the desired dimensions using scissors, and then flattened between two polished steel plates. The foils were washed with soap and water, cleaned ultrasonically in isopropanol, and dried with a hot-air gun.

For annealing foils, the samples were loaded in a 99.98-wt% Al_2O_3 crucible. SSA-999W Al_2O_3 blocks were used as a deadweight. The sample was placed in a vacuum furnace (Centorr, Suncook, NH) with a W element and run at high vacuum ($\leq 8 \times 10^{-5}$ Torr).

Heating and cooling rates of 30°C/min, were used to minimize microstructural evolution effects occurring outside of the isothermal-soak regime.

3.3 Deposition

3.3.1 Sputtering

To coat foils with a refractory-metal cladding, a Perkin Elmer 2400 sputtering system was used. The cleaned foils were placed inside the unit, and pumped down to a vacuum of $\leq 8 \times 10^{-5}$ Torr. During sputtering, the chamber was pressurized with 10 mTorr of Ar gas. Ti was initially sputtered for 2 min away from the foils in order to getter any remaining O. The foils were then moved under the desired target and either Nb or Mo was deposited at 700W. Once coating was completed, the chamber was evacuated, the foils were flipped, and the process was repeated to coat the other side.

3.3.2 Physical Vapor Deposition

When substrates or foils needed to be coated with a Ni cladding, a bell-jar-type physical-deposition system (Mikros Inc., Portland, OR) was used. A high vacuum ($\leq 8 \times 10^{-5}$ Torr) was maintained throughout the deposition process. When attempting to deposit Ni directly onto the Al_2O_3 substrates, the Ni film spalled off. As a result, Ni had to be deposited onto the core foil in a two-step process. The foil was placed on a platform so that one side was exposed, and 99.98-wt% Ni wire (Goodfellow Corporation, Malvern, PA) was cut into ~0.15 g pieces to be loaded into Al_2O_3-coated, W boats. Use of Al_2O_3-coated boats was necessary since liquid Ni reacts with the heated W and would otherwise cause the boat to fail. The amount of Ni used depended on the desired film thickness. It had been determined that 0.6 g of Ni would yield a final film thickness of ~2 μm. The film thickness varied linearly with the initial amount of Ni, so for a ~1-μm coating, 0.3-g Ni was used. After deposition, the foil was flipped so that its opposite side was exposed, the boats were reloaded, and the coating process repeated.

3.4 Bonding

3.4.1 Hot Press

For TLP-bonding experiments with an applied pressure, summarized in Table 3.1, a foil was placed between the polished faces of two substrates and the assembly was loaded into a graphite-element hot press (Thermal Technologies Inc., Santa Rosa, CA). The bonds were processed under high vacuum ($\leq 8 \times 10^{-5}$ Torr), and at a constant pressure throughout the bonding cycle. Heating was done at 4°C/min until the soak temperature was reached, and then cooling occurred at 2°C/min. Occasionally during heating, the samples had to be temporarily held at a temperature lower than the soak temperature in order to maintain the pressure below 8×10^{-5} Torr, but only when the temperature was below 1050°C to ensure that diffusion within the core layer was not appreciably altered.

3.4.2 Vacuum Furnace

For bonds made using minimal pressure, the samples were loaded in a 99.98-wt% Al_2O_3 crucible, with a smaller Al_2O_3 crucible containing W rods on top as a deadweight. The sample was placed in a vacuum furnace (Centorr, Suncook, NH) with a W element and run

at high vacuum ($\leq 8 \times 10^{-5}$ Torr). Heating and cooling rates were 4°C/min and 2°C/min, matching those used in hot-press experiments.

3.5 Mechanical Testing

Bonded polycrystalline-Al_2O_3 assemblies were processed into 16 beams to be tested in 4-point bending. The bonded assembly was cut into four, 5-mm-thick plates using a Struers Accutom-2 high-speed saw (Struers, West Lake, OH) using a M0-15 diamond blade (Struers, West Lake, OH). The plates were ground flat on both sides using a succession of 75-μm and 30-μm grinding plates (South Bay Technologies, San Clemente, CA) on a Buehler grinding wheel (Evanston, Illinois) until the plates were 3-mm thick. They were then polished on a mechanical polisher (Logitech PM4, Glasgow, Scotland) using successively finer diamond suspensions (South Bay Technologies, San Clemente, CA) – 9 μm, 6 μm, 3 μm, 1 μm – and a colloidal-silica suspension (Struers, West Lake, OH). Each plate was cut into four, 3 mm × 3 mm × 40 mm beams using the surface grinder. The polishing minimizes cracks and flaws along the surface of the beams that act as stress concentrators, which can initiate premature failure of the beam during testing. Since the sharp edges of the polished face are also stress concentrators, the edges of the polished face on each beam were beveled by hand on a 3000-grit grinding wheel and polished using colloidal silica to eliminate edge effects during bend testing.

The prepared beams were ultrasonically cleaned in successive solutions of soap and water, distilled water, acetone, and isopropanol for 15 min each, before drying with a hot-air gun. Bend testing was performed on an Instron 1122 (Canton, MA) tensile-testing unit in compression mode at a crosshead speed of 0.5 mm/min. The bend jig had an outer span of 25 mm and an inner span of 9 mm, and was fully articulating. The beams were oriented so that the polished face was in tension during bending.

3.6 Optical Microscopy

Optical microscopy was performed on the beams both before bend testing, to examine the tensile surface for any stress-concentrating flaws, and after bend testing using reflected light. To examine the fracture surfaces of beams that failed at the interface, the beams were mounted vertically using putty.

3.7 Electron-Probe MicroAnalysis

Electron-probe microanalysis (EPMA) was employed using a Shimadzu EPMA-1600 to determine the compositional profile across the interlayer. Beams were cut using a low-speed diamond saw so that ~5 mm of Al_2O_3 remained on either side of the bonded interface. The samples were mounted in an epoxy resin (Buehler EPO-Kwick), ground flat using a Struers Pedepin (Copenhagen, Denmark), polished on a nylon pad using progressively smaller diamond pastes –15 μm, 6 μm, 3 μm, 1 μm – on the Syntron vibratory polisher (Homer City, PA), and finished using a colloidal-silica suspension. A line scan was taken across the polished interlayer with a step size of ~3 μm between points. The spot size was ~2 μm in diameter. Because the spot size was approximately the same as the initial thickness of the cladding, the measured compositions of smaller features may not have been from a single homogeneous phase or material, but instead an average composition across a grain or phase boundary. Thus,

the EPMA profiles were interpreted in conjunction with an optical micrograph of the sample in order to determine the validity of the results.

3.8 Wetting Experiments

To determine the contact angle of different Ni alloys expected at the interface of the PTLP bonds, sessile-drop wetting experiments were performed. The Ni alloys fabricated were chosen to mimic the compositions expected to exist during the bonding cycle.

3.8.1 Substrates

Polycrystalline Al_2O_3 and ZTA described in Section *3.2.1* were cut into plates ~20 mm × 20 mm × 3 mm, and then ground and polished using the same procedure as previously described. The plates were then cut into 5 mm × 5 mm × 3 mm pieces using a low-speed diamond saw. For Y_2O_3-stabilized ZrO_2 (YSZ), pre-polished single crystals were obtained from Crystec (Berlin, Germany). Before use, each piece was ultrasonically cleaned in solutions of distilled water and soap, distilled water, acetone, and isopropanol for 15 min each, before being dried with a hot-air gun. Finally, they were air-annealed (CM elevator furnace, Bloomfield, NJ) for 1 h at 1000 °C to remove any residual organics.

3.8.2 Alloys

The composition of the liquid phase expected during TLP bonding is dependent on the phase diagram of the specific core/cladding combination being used. To determine the wetting properties of the expected liquid phase, alloys were prepared for use in sessile-drop wetting experiments. The starting powders used for the alloys were: 45-μm Ni powder (99.8-wt% pure) and 60-μm Mo powder (99.9-wt% pure) from Alfa Aesar (Ward Hill, MA), 45-μm V powder (99.7-wt% pure) from Goodfellow Corp (Huntingdon, England), 45-μm Nb powder (99.8-wt% pure) from Aesar (Seabrook, NH). The individual components were massed to ±0.001 g using a digital scale (Mettler Toledo, Greifensee, Switzerland) and dry rolled in a ball mill for several hours. The mixed powders were placed in an Al_2O_3 crucible (CoorsTek Inc., Golden, CO) and melted in an Ar – 2-wt% H_2 atmosphere (Centorr, Suncook, NH). The alloys produced are shown in Table 3.2. For wetting experiments involving pure metals, Ni wire (99.98-wt% pure) from Goodfellow Corp (Huntingdon, England) and Co wire (99.995-wt% pure) from Alfa Aesar (Ward Hill, MA) were used.

3.8.3 Wetting Furnaces

To determine the role of Nb on contact angle, sessile-drop experiments where the contact angle was measured *in situ* at the holding temperature were performed using a range of Nb alloys on different ceramic substrates. For each experiment, an ~0.2-g piece of alloy was placed on top of a polished substrate described in Section *3.8.1* in high vacuum ($\leq 8 \times 10^{-5}$ Torr). Due to constraints on availability, two different wetting furnaces were employed. Table 3.3 shows the holding times and temperatures for experiments performed in a Mo-element vacuum furnace using the maximum heating and cooling rate possible, 30°C/min. Table 3.4 shows the holding times and temperatures for experiments performed in a C-element vacuum furnace using the maximum heating and cooling rate possible, 15°C/min.

For both furnaces, a transparent window allowed digital photographs of the samples to be taken at the soak temperature. The contact angles of the solidified droplets were determined using ImageJ (Wayne Rasband, National Institute of Health) software.

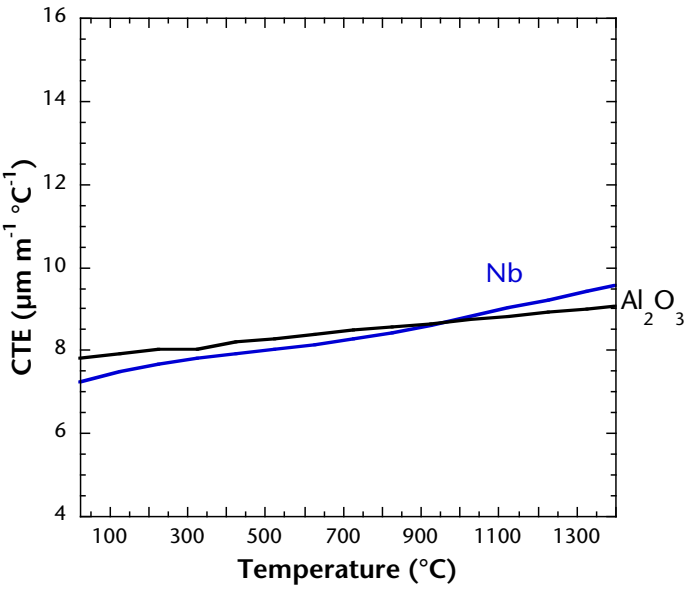

Figure 3.1: CTE of Nb and Al_2O_3 between room temperature and 1400°C [122,123].

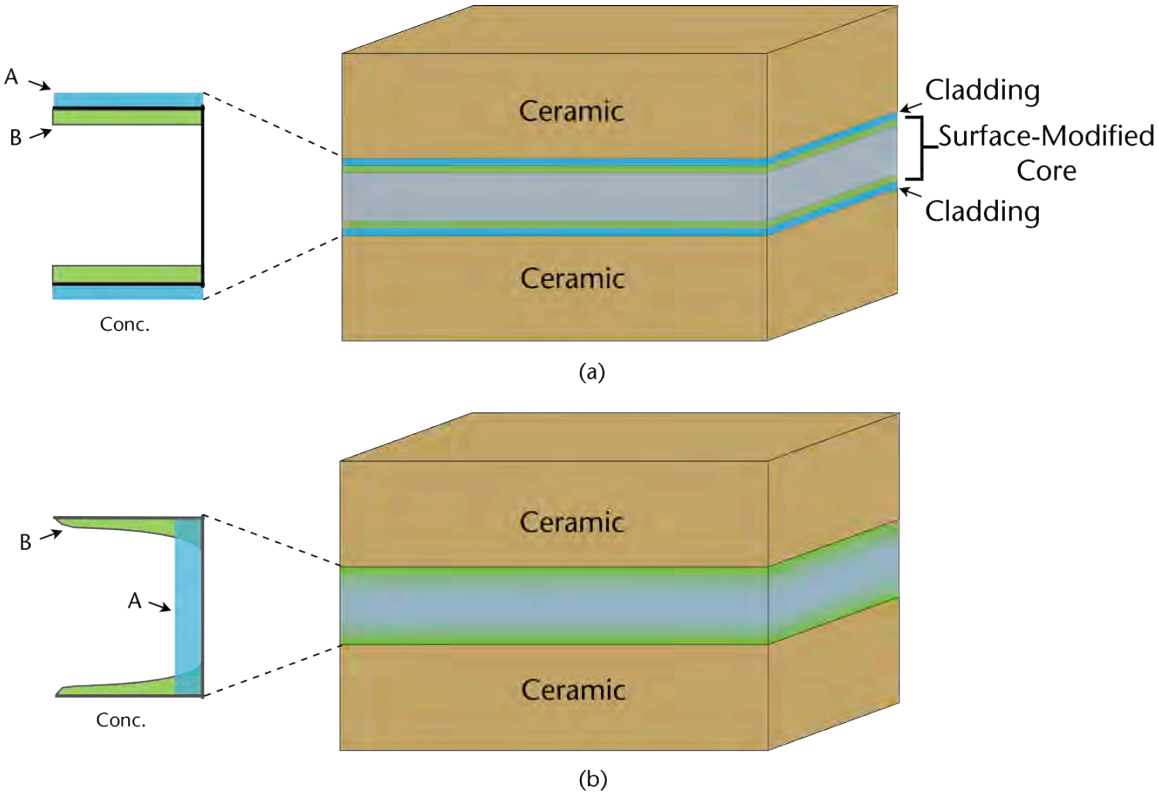

Figure 3.2: PTLP bonding using a surface-modified core a) prior to bonding, cladding A and the core-surface-modifier B are concentrated at the interface b) after bonding component A has homogenized across the interlayer, while component B remains concentrated at the interface.

Table 3.1: Bonds fabricated in hot press

Substrate	Core	Outer Cladding	Applied Pressure (kPa)	Soak T (°C)	Soak time
ZTA	125-μm Nb	2-μm Ni	6.7	1400	6 h
ZTA	125-μm Nb	2-μm Ni	6.7	1400	5 min
ZTA	125-μm Nb	2-μm Ni	2400	1400	6 h
ZTA	125-μm Nb	2-μm Ni	2400	1400	5 min
999W Al_2O_3	125-μm Mo	2-μm Ni	2400	1400	30 min
999W Al_2O_3	2-μm Nb/125-μm Mo	2-μm Ni	2400	1400	6 h
999W Al_2O_3	125-μm V	2-μm Ni	2400	1400	6 h
999W Al_2O_3	2-μm Nb/125-μm V	2-μm Ni	2400	1400	6 h
999W Al_2O_3	1-μm Nb/125-μm V	1-μm Ni	2400	1400	6 h
999W Al_2O_3	3-μm Mo/125-μm V	1-μm Ni	2400	1400	6 h
999W Al_2O_3	1-μm Mo/125-μm Nb	1-μm Ni	2400	1400	6 h
999W Al_2O_3	3-μm Mo/125-μm Nb	1-μm Ni	2400	1400	6 h
999W Al_2O_3	1-μm Nb/125-μm Mo-V	1-μm Ni	2400	1400	6 h
999W Al_2O_3	125-μm Nb	1-μm Ni	2400	1400	6 h

Table 3.2: Alloys fabricated for sessile-drop experiments

Composition (at%)	Ramp Rate (°/min)	Soak T (°C)	Soak Time
99 Ni: 1 Nb	30	1550	2 h
39 Ni: 61 Nb	30	1600	12 h
54 Ni: 46 V	30	1300	90 min
42 Ni: 58 Mo	30	1620	90 min
62 Ni: 19 Mo: 19 Nb	30	1620	90 min

Table 3.3: Processing conditions for Mo-heating-element sessile-drop experiments

Alloy (at%)	Substrate	Ramp Rate (°/min)	Soak T (°C)	Soak Time
54 Ni: 46 V	999W	30	1400	30 min
42 Ni: 58 Mo	999W	30	1400	30 min
62 Ni: 19 Mo: 19 Nb	999W	30	1400	30 min

Table 3.4: Processing conditions for C-heating-element sessile-drop experiments

Alloy (at%)	Substrate	Ramp Rate (°/min)	Soak T (°C)	Soak Time
39 Ni: 61 Nb	ZTA	15	1400	30 min
39 Ni: 61 Nb	{100} YSZ	15	1400	30 min
39 Ni: 61 Nb	{111} YSZ	15	1400	30 min
99 Ni: 1 Nb	999W	15	1500	30 min

4. Results and Discussion

4.1 Sessile-Drop Wetting Studies

For PTLP bonding, the ability of the interlayer's liquid phase to flow along the interface and fill strength-reducing gaps and voids is critical to producing reliable and robust bonds. As described in Section 2.3.2, sessile-drop experiments can give insight into whether a particular molten alloy will effectively spread along the interface of a PLTP bond. Lower contact angles typically lead to higher bond strengths[29]. For Al_2O_3 bonded using Ni/Nb/Ni interlayers, a eutectic 59-at% Ni-Nb liquid forms beginning at 1184°C, as shown in Figure 2.5. To better understand the wetting characteristics of this eutectic liquid, sessile-drop experiments have been performed, and the contact angles measured, both *in-situ* and post-mortem. The results have shown that on polished polycrystalline and c-sapphire substrates 61-at% Ni-Nb has a contact angle of ~90° [1,3,119]. This is significantly lower than the contact angle of pure Ni, ~110°, on the same substrates[7,17-24]. This significant decrease in contact angle raises the question of what effect Nb will have on the contact angle of other alloys and on other oxide ceramics, and whether the effect is limited to Nb-based alloys or would extend to other refractory-based alloys as well.

To further explore the effect of Nb additions on contact angle, a number of Nb-based and other refractory-based alloys were fabricated for sessile-drop experiments. The alloy compositions, substrates tested, and results are summarized in Table 4.1. The results give more insight into the role of Nb on contact angle for oxide substrates. First, a small quantity of Nb can significantly influence the contact angle of Ni-Nb alloys on Al_2O_3 substrates. Compared to the contact angle of pure Ni, ~110°, 1-at% Nb-Ni has a contact angle of 97° on polycrystalline Al_2O_3. Second, Ni-Nb alloys had relatively low contact angles, ~90°, on ZrO_2 and ZrO_2-toughened Al_2O_3 (ZTA). Third, additions of other core layer metals, Mo and V, to Ni did not cause any decrease in contact angle relative to that reported for pure Ni on Al_2O_3. In the case of the Ni-Mo alloy the contact angle actually increased to 121°. Finally, the addition of Nb to Ni-Mo alloys decreased the contact angle on Al_2O_3 to 88°, equivalent to that of a 61-at% Ni-Nb alloy.

The ability of Nb to reduce the contact angle of metal alloys on Al_2O_3 and other oxides in sessile-drop experiments can be exploited when designing interlayers for PTLP bonding. The ability of Nb alloys to have a contact angle ≤90° without the formation of a reaction layer at the alloy/ceramic interface is of particular note, as such liquids have a substantially better chance of filling interfacial gaps and voids along the bonding interface. On rough surfaces, Wenzel[11] found that the apparent contact angle is greater than the actual contact angle when the liquid phase is non-wetting, or less than the actual contact angle when the liquid wets the surface. Others have demonstrated that for a liquid phase flowing between two parallel surfaces, when the surface roughness increased for one of the surfaces, the liquid's ability to wet the interface could be either reduced or enhanced depending on its contact angles on the two surfaces[2,113]. For liquids that had contact angles <90° on the roughened surface, the ability for the liquid to flow along the interface remained nominally constant (when the contact angle was <90° on the second surface as well) or increased (when the contact angle was >90° on the second surface). By contrast, for liquids with contact angles that were >90°, the ability to flow along the interface remained nominally constant (when the contact angle was >90° on the second surface), or increased (when the contact angle was <90°

on the second surface). Since the liquid phase in PTLP bonding involves one metal/ceramic interface (contact angles for non-reactive metals are typically ≥90° [9,128]) and a metal/metal interface (contact angles ≤60° [9]), lowering the metal-ceramic contact angle increases the ability of the liquid phase to spread along the interface.

Since Nb forms complete solid solutions with other refractory alloys, Nb can be added to the interlayer on an as-needed basis. Since core-layer dissolution occurs, incorporation of Nb into the liquid is expected to reduce the contact angle of the TLP layer. Because only small quantities of Nb are needed to appreciably lower the contact angle, the addition of Nb can be designed to have a minimal impact on the CTE of the interlayer. Finally, since Nb-alloys also have relatively low contact angles on ZrO_2 and ZrO_2-containing substrates, it is possible that PTLP bonding using Nb-containing interlayers can result in strong and reliable bonds for these materials as well.

4.2 PTLP Bonding of ZTA

As a method to determine whether Ni/Nb/Ni interlayers could be successfully employed to bond ceramics other than high-purity Al_2O_3, attempts were made to join ZTA. ZTA was chosen for a number of reasons. First, it is 85-wt% Al_2O_3, so the CTE for ZTA is similar to that of both Al_2O_3 and Nb. Second, as shown in Section 4.1, the overall wetting characteristics of the Ni-Nb liquid on ZTA are comparable to those of Ni-Nb on pure Al_2O_3 – both have a contact angle ~90°. Third, bulk ZTA has a higher bend strength than that of Al_2O_3, the manufacturer reports it as 750 MPa, which would potentially allow the upper bend strength limit using a Ni/Nb/Ni interlayer to be quantified. To date, nearly all of the PTLP bonded Al_2O_3 bonded using Ni/Nb/Ni interlayers and a 2.4-MPa bonding pressure have failed in the ceramic. Thus, in those assemblies, it is the properties of the bulk ceramic that are strength limiting, not the bonded interlayers. By increasing the fracture strength of the bulk material, in this case by using ZTA, it is hoped that interfacial fractures can be induced, giving a quantifiable measurement of the interfacial bond strength.

ZTA was bonded using 2-μm Ni/Nb/2-μm Ni interlayers. The fracture strengths of bonds fabricated using different pressures were compared to those of HIPed 999S Al_2O_3 published previously[1,3,119]. When the Al_2O_3 was bonded using 2-μm Ni/Nb/2-μm Ni interlayers and 2.4-MPa pressure, it was observed that nearly all fractures occurred in the bulk material. For the samples that did fracture interfacially, they did so at the highest bond strengths. When compared to bend tests of monolithic Al_2O_3, the fracture strengths of the bonded Al_2O_3, including interfacial fractures, were comparable. After undergoing the same processing conditions, 6 h at 1400°C with a 2.4-MPa pressure, the fracture strength for the monolithic Al_2O_3 was 560±83 MPa, compared to 523±63 MPa for the joined 999S Al_2O_3 assembly[1].

In contrast, Figure 4.1 shows that the ZTA bonded under the same processing conditions had several interfacial fractures that were the lowest-strength bonds in the sample set. Comparing only the fractures occurring in the bulk ceramic, the average strength of the ZTA and 999S samples were nearly identical, 517±56 MPa and 523±63 MPa, respectively. However, the interfacial failures that occurred in the ZTA bonds had an average fracture strength of 266±41 MPa – nearly five standard deviations away from the ceramic failure average strength.

It is unclear why some samples failed interfacially, and why their fracture strengths were so low. The CTE of ZTA and Al_2O_3 are comparable, so residual stresses formed during cooling are minimal. As with the previously studied Al_2O_3 bonds, optical microscopy of the interlayer revealed minimal presence of a Ni-Nb intermetallic formation along the metal/ceramic interface, as shown in Figure 4.2. On the interfacial fracture surfaces, shown in Figure 4.3, there is little presence of any intermetallic. However, on the metal fracture surface a number of grains were pulled out from the ceramic fracture surface. These types of pulled-out regions only appear along the tensile edge of the fracture surface, as shown in Figure 4.4, and were ~10 μm in diameter. This could account for the localized grain pullout only along the tensile face near the surface and would also introduce a flaw at the interface, allowing the crack to propagate and resulting in interfacial failure.

The ZTA consists of an Al_2O_3 matrix with discrete, dispersed ZrO_2 phase throughout. The ZrO_2 has been stabilized with 5-wt% Y_2O_3. As a result, a majority of the ZrO_2 phase is in a metastable tetragonal phase in an Al_2O_3 matrix[129]. A number of chemical and mechanical changes could have occurred to the ZTA during the bonding process. The low p_{O_2} of the bonding atmosphere can cause a reduction reaction in the ZrO_2 phase near the bond interface. The diffusion rate of O in Al_2O_3 is low. Over the entire bonding cycle the grain-boundary diffusion distance, $\sqrt{Dt}$, is only ~1 μm, and lattice diffusion in negligible. However, within the Y_2O_3-doped ZrO_2 phase O diffuses very rapidly, $\sqrt{Dt}$ = 5 mm for the bonding cycle. Thus ZrO_2 particulates in contact with the interface can have significant quantities of O removed, causing a reduction of strength.

During cooling, the near-surface stress state is such that the ZrO_2 phase undergoes a phase transformation to monoclinic, resulting in a volume change in the ZrO_2, and potentially introducing microcracks into the ZTA [130]. The process of grinding and polishing the ZTA surface can also induce the phase transformation, potentially causing microcracks to form[131]. Microcracks would weaken the near-interfacial layer of ZTA, and would introduce an added stress near the interface. A combination of microcracking and chemical reduction of the ZrO_2 would cause regions of weakened grains to be present near the interface, making grain pullout more likely.

SEM images of the tensile surface show that regions of increased porosity exist ~20 μm into the ZTA, perpendicular to the interface, as seen in Figure 4.5. This micrograph is of a sample that had already undergone mechanical testing. Two potential mechanisms are plausible. Green *et al.*[131] found that the compressive surface stresses that occur from grinding are at a maximum ~20 μm from the ground surface, at the same location as the band of porosity was observed. Annealing of the region during bonding could result in stress-relaxation. However, as mentioned previously the diffusion distance of O in Al_2O_3 is very short, ~1 μm, which is much smaller than the size of the pores. This makes diffusion-based mechanisms unlikely. The other explanation is that they are regions of microcracking that form during bend testing. Since the flaws are located at a region of maximum stress, this is a plausible explanation. In SEM images of as-received ZTA, no such regions of porosity existed. As no micrographs of the interlayer were taken between bonding and testing, further work would be needed to determine the exact mechanism of the flaw formation.

As seen in Figure 4.6, the strength of the ZTA bonds fabricated using a 6.7-kPa applied pressure were comparable to those of 999S Al_2O_3 bonded using a 2.4-MPa pressure,

and higher than the ZTA bonded using a 2.4-MPa pressure. However, while only the lowest strength ZTA bonds bonded with a 2.4-MPa pressure failed at the interface, the majority of the 6.7-kPa-applied-pressure ZTA bonds failed at the interface across all strengths. The difference in fracture types is due to the presence of a Ni_6Nb_7 intermetallic phase that forms at the interface when samples are bonded at lower bonding pressures, as seen in Figure 4.7. The EPMA scan across the interlayer in Figure 4.8 shows the regions of high Ni content near the interfaces of the bond, which is indicative of Ni_6Nb_7 formation. The intermetallic phase forms at lower bonding pressures because, during the bonding process, the Ni-rich liquid phase is not squeezed out of the interface as it is in the case of the 2.4-MPa bonds. In prior work, bonds fabricated under a 2.4-MPa pressure were found to have ~80% of the liquid phase extruded from the interface during bonding[3,120].As a result, more Ni remains at the interface during bonding, and not all of it is incorporated into the Nb core. Larger quantities of Ni_6Nb_7 intermetallic present near the tensile face of a sample have been associated with lower fracture strengths[119].

Previously, when Al_2O_3 bonds had been fabricated under a 6.7-kPa pressure, it was found that a number of the bonds failed interfacially[1,119]. Figure 4.9 compares the fracture strengths of the ZTA bonds to those of 999S Al_2O_3 bonded at both 2.4 MPa and 6.7 kPa of pressure. The Al_2O_3 samples bonded using 2-μm Ni/Nb/2-μm Ni under a 6.7-kPa pressure had a lower average strength than ZTA bonded using the same interlayer and conditions. However, Al_2O_3 samples bonded using 1-μm Ni/Nb/1-μm Ni interlayer had comparable strengths to the ZTA samples bonded with a 2-μm Ni/Nb/2-μm Ni interlayer. The physical-vapor deposition system used to deposit the Ni coatings was only accurate to a thickness ±0.5 μm, so it is reasonable to assume variations in the initial Ni coating thickness occurred. Importantly, it was found that at an applied pressure of 6.7 kPa, both ZTA and Al_2O_3 could produce bonds that were equivalent in strength to their 2.4 MPa counterparts.

It is unclear why there was a discrepancy between the manufacturer's reported 4-point bend strength of 750 MPa for the material, and the average bend strength of ceramic fractures in the ZTA bonds manufactured under both 2.4 MPa (517±56 MPa) and 6.7 kPa (491±80 MPa) of applied pressure. There was no appreciable change in the grain size of the ZTA during the bonding process, which remained ~1.5 μm on average for the as-received ZTA, and samples bonded at both 2.4-MPa and 6.7-kPa applied pressure. As discussed previously, while a region of transformed ZTA is expected to exist near the bonded interface, all ceramic failures occurred ≥1 mm from the interface, so the near-interface transformed region would not affect the overall strength in the case of a ceramic failure. When the bonded assemblies were being prepared for mechanical testing and cut into beams, the exterior of the bulk ZTA was removed, so chemical reduction of the exterior is not expected to be a factor. There was no correlation between original location of the beam in the bonded assembly and the final fracture strength.

The manufacturer of the ZTA was not able to provide information about the whether ZrO_2 was initially a cubic, tetragonal and monoclinic phase, or whether the ZrO_2 regions were initially agglomerations of a mixture of ZrO_2 phases. Coarsening of tetragonal ZrO_2, which could have occurred during the bonding process, would lead to a lower energy barrier for the tetragonal-to-monoclinic phase transformation, causing a higher fraction of monoclinic phase to exist after bonding[132,133]. Higher fractions of the monoclinic phase change the toughening

mechanism from predominantly transformation toughening to microcracking, which can also lead to degradation of the material strength[130,134-136]. In order to properly compare the fracture strengths of the bonded ZTA to that of the bulk material, it would be necessary to test the bend strength of monolithic ZTA beams, both as-received and after annealing under the bonding conditions, which was not feasible for the present study. However, when using a 2.4-MPa applied pressure, both the ZTA and Al_2O_3 bonds failed in the ceramic at the highest strength, indicating maximum bond strength has not yet been reached and even higher bond strengths may be possible when joining stronger bulk materials.

Overall, ZTA assemblies bonded using Ni/Nb/Ni interlayers were comparable in strength and in microstructural evolution to high-strength HIPed 999S Al_2O_3 assemblies similarly bonded. While the bulk ZTA and Al_2O_3 are substantially similar in composition and microstructure, this is nevertheless confirmation that PTLP bonding using refractory-metal cores can be successful beyond the high-purity Al_2O_3 systems. In addition, in preliminary experiments bonds of {100} YSZ have been fabricated successfully using Ni/Nb/Ni interlayers as well. These bonds were qualitatively robust and could not be broken by hand. These results bode favorably for the expansion of PTLP bonding to other ceramic systems.

Table 4.1: Sessile-drop experiments using refractory-metal-based alloys.

Alloy (at%)	Substrate	Soak T (°C)	Soak Time	Contact Angle (°)
99 Ni: 1 Nb	999W	1500	30 min	97
61 Ni: 39 Nb	ZTA	1400	30 min	91
61 Ni: 39 Nb	{100} YSZ	1400	30 min	87
61 Ni: 39 Nb	{111} YSZ	1400	30 min	97
54 Ni: 46 V	999W	1400	30 min	111
42 Ni: 58 Mo	999W	1400	30 min	121
62 Ni: 19 Mo: 19 Nb	999W	1400	30 min	88

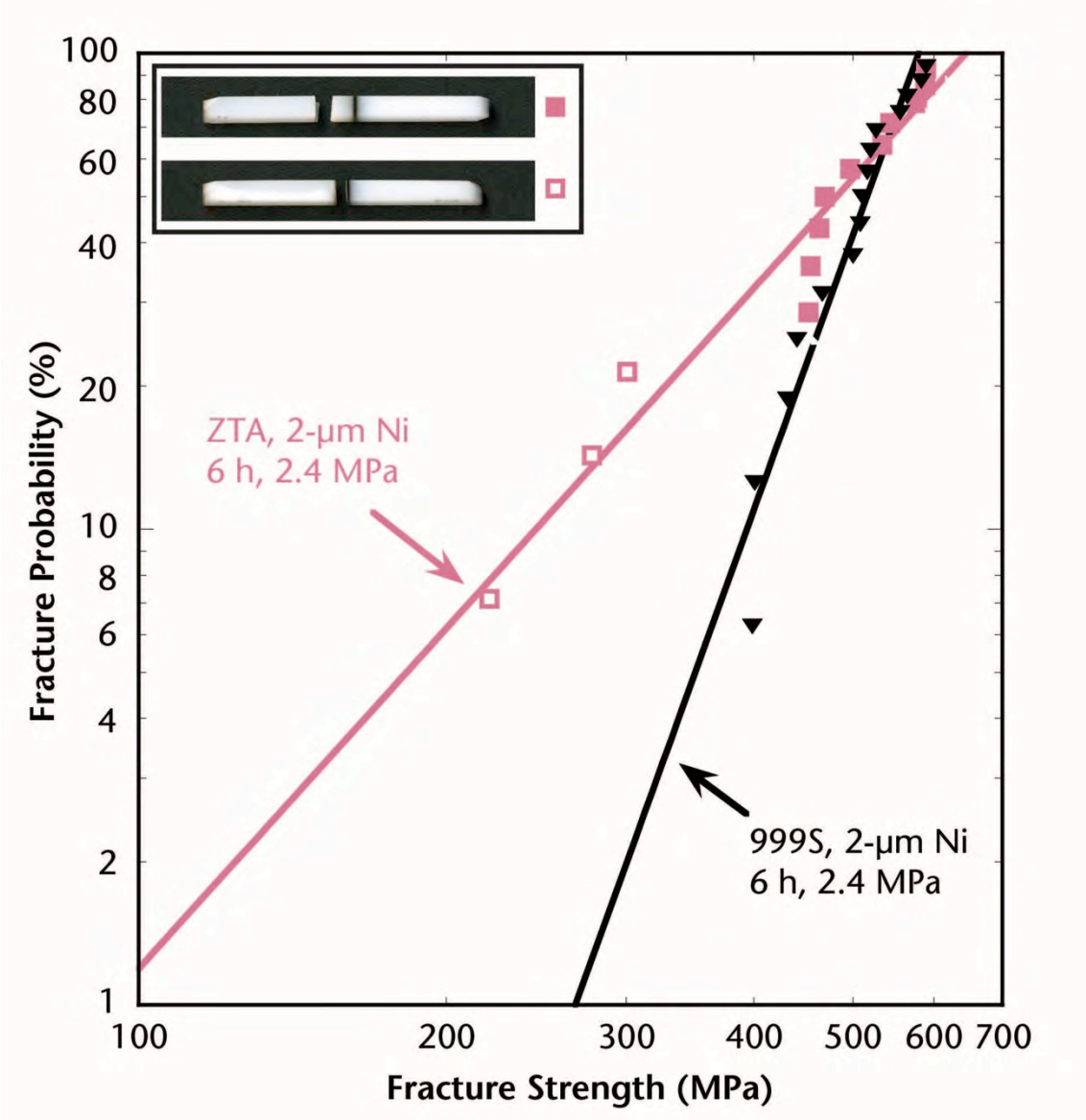

Figure 4.1: Fracture strength of ZTA and 999S Al_2O_3 bonded using Ni/Nb/Ni interlayers and a 6.7-kPa deadweight pressure. Open data points represent interfacial fractures, while filled data points represent fractures that occurred in the ceramic.

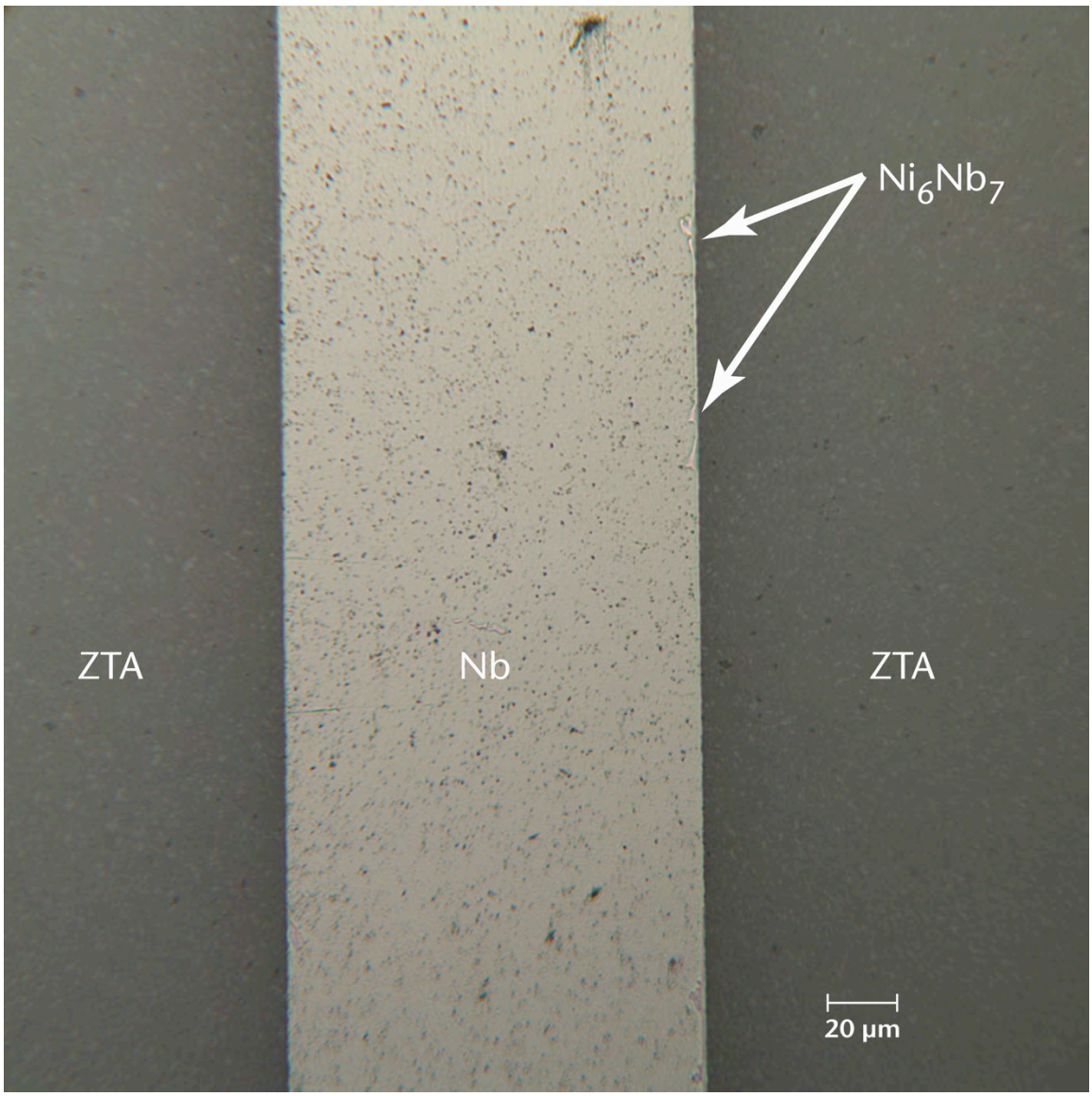

Figure 4.2: ZTA bonded using an interlayer of a 2-µm Ni/Nb/2-µm Ni bonded at 1400°C for 6 h under a 2.4-MPa pressure. There is minimal presence of a Ni_6Nb_7 intermetallic along the interface.

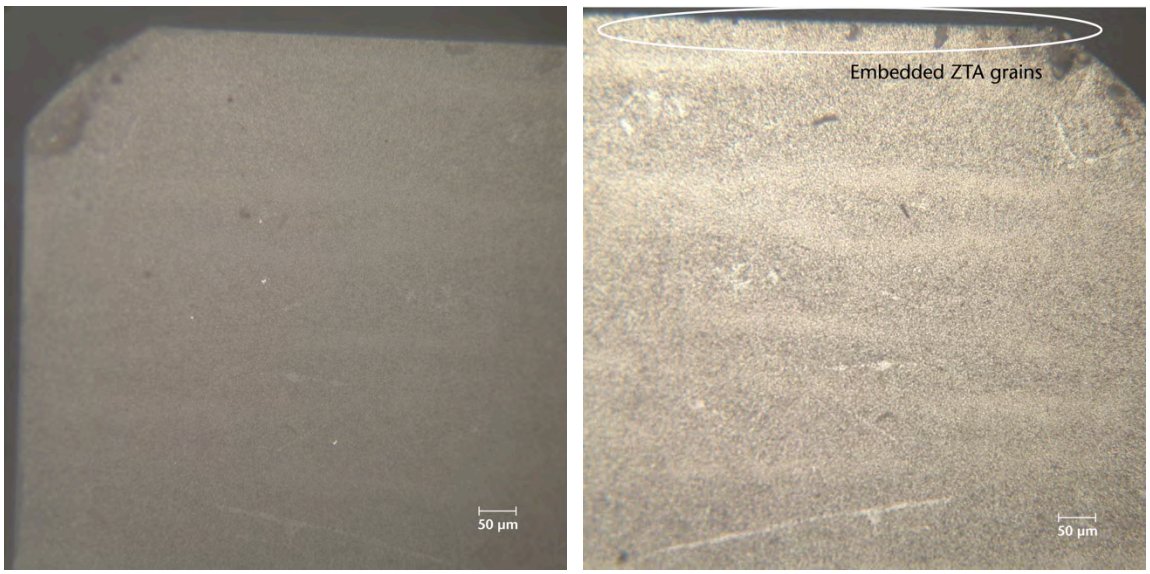

(a) (b)

Figure 4.3: (a) ceramic and (b) metal fracture surfaces of ZTA bonded using Ni/Nb/Ni interlayer at 1400°C under a 2.4-MPa pressure. Tensile face is at the top of the images. Fracture occurred at the metal/ceramic interface, with minimal metallic phase remaining on the ceramic interface. Note the ceramic grains that are along the tensile face of the metal surface.

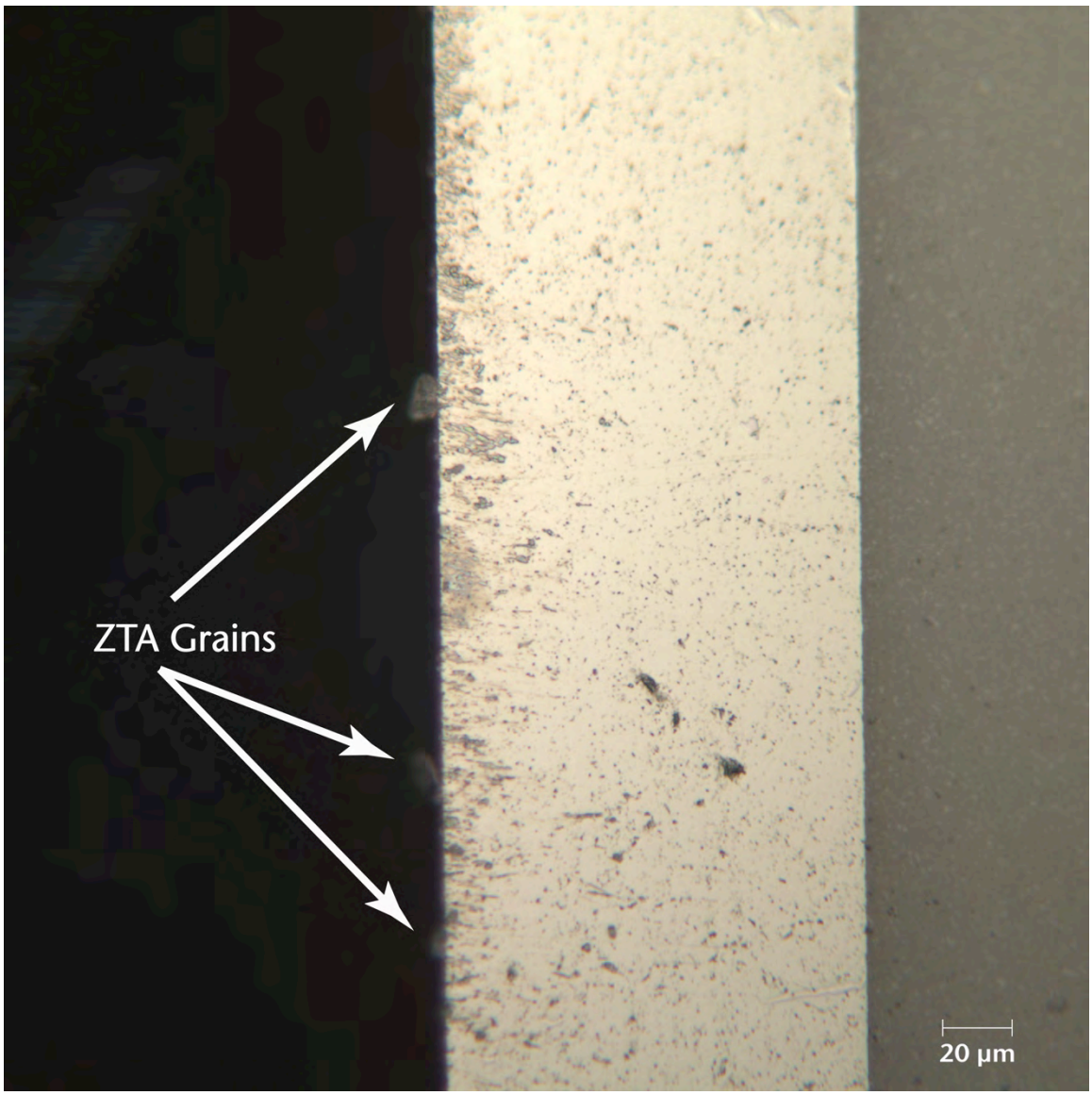

Figure 4.4: A number of ZTA grains remained attached to the metal interface after fracture. Most of the pulled-out grains were found embedded near the edge where fracture initiated.

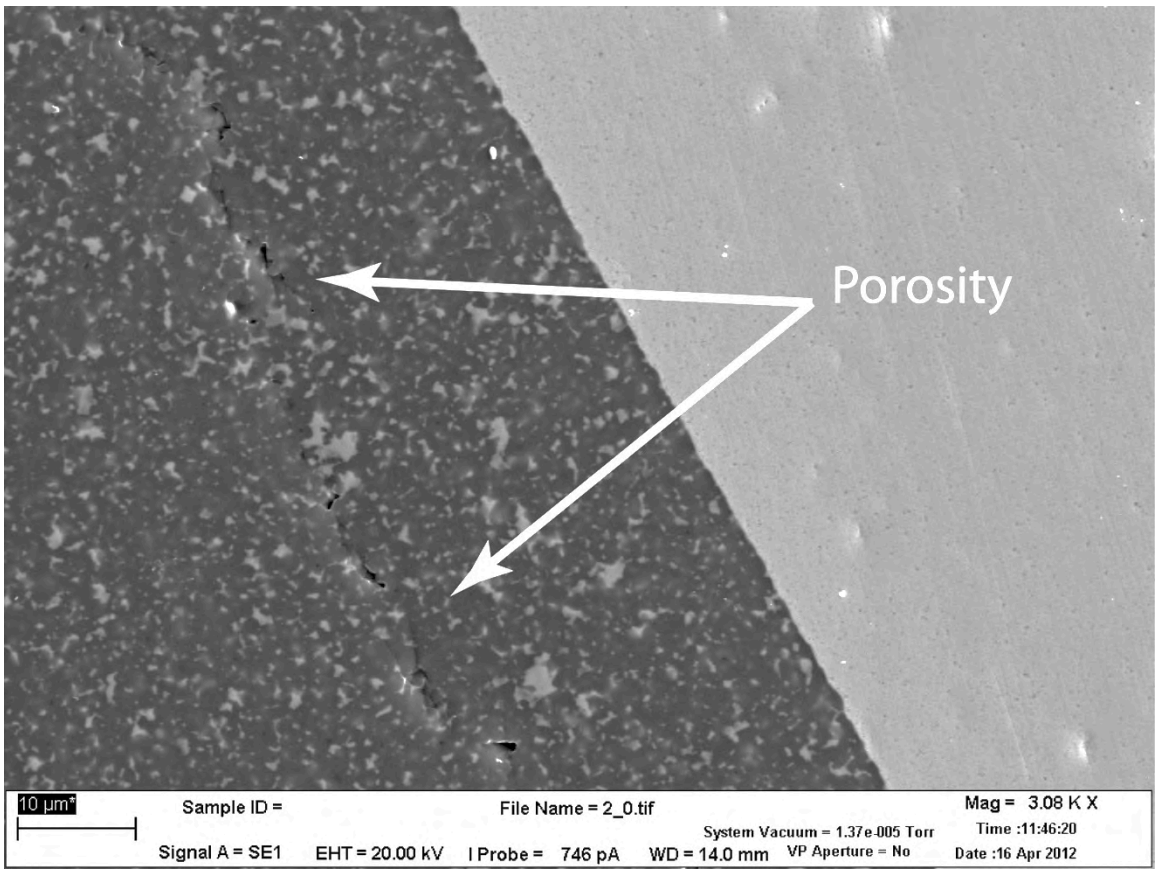

Figure 4.5: Tensile surface of ZTA/Ni/Nb/Ni/ZTA bonded for 6 h at 1400°C using a 2.4-MPa applied pressure. Regions of porosity parallel the interface with ~20 µm between them.

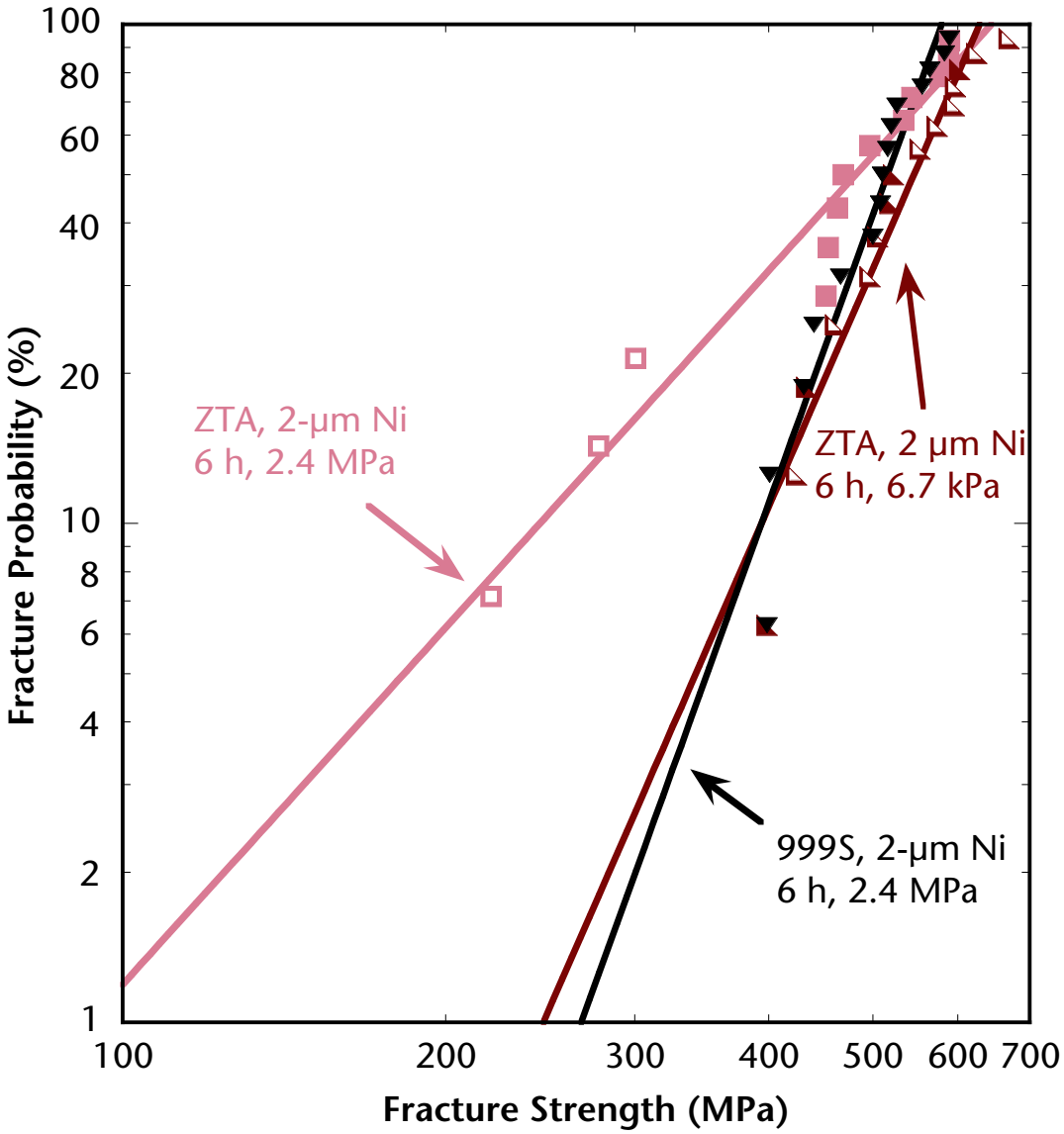

Figure 4.6: Fracture strength of ZTA bonded using Ni/Nb/Ni interlayer with either a 6.7-kPa or 2.4-MPa pressure. Open data points represent interfacial fractures, while filled data points represent fractures that occurred in the ceramic.

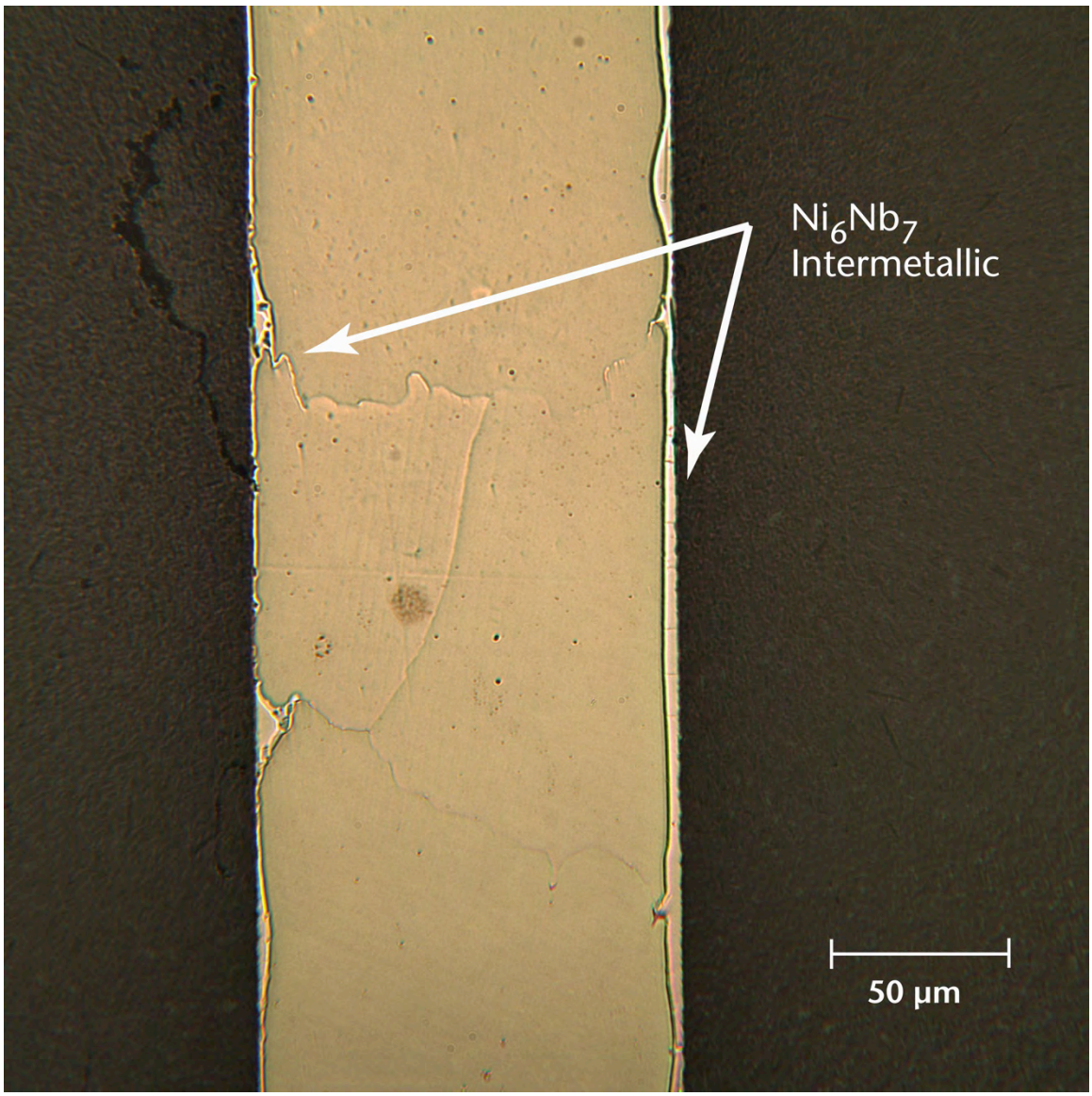

Figure 4.7: Optical image of ZTA bonded with a Ni/Nb/Ni interlayer using a 6.7-kPa pressure for 6 h at 1400°C. A Ni_6Nb_7 intermetallic phase is present at the ZTA/Nb interface.

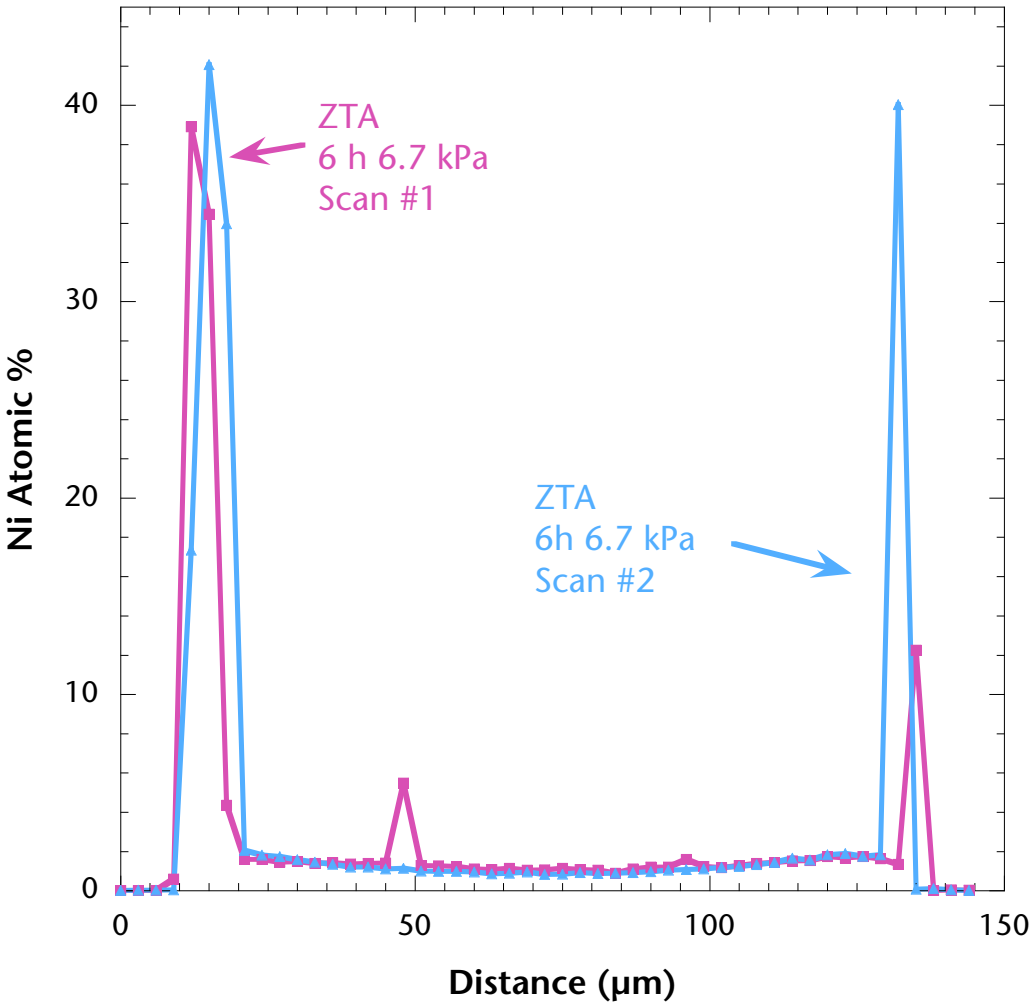

Figure 4.8: EPMA of ZTA bonded for 6 h at 1400°C under a 6.7-kPa pressure. The areas of high Ni content indicate the presence of the Ni_6Nb_7 intermetallic phase.

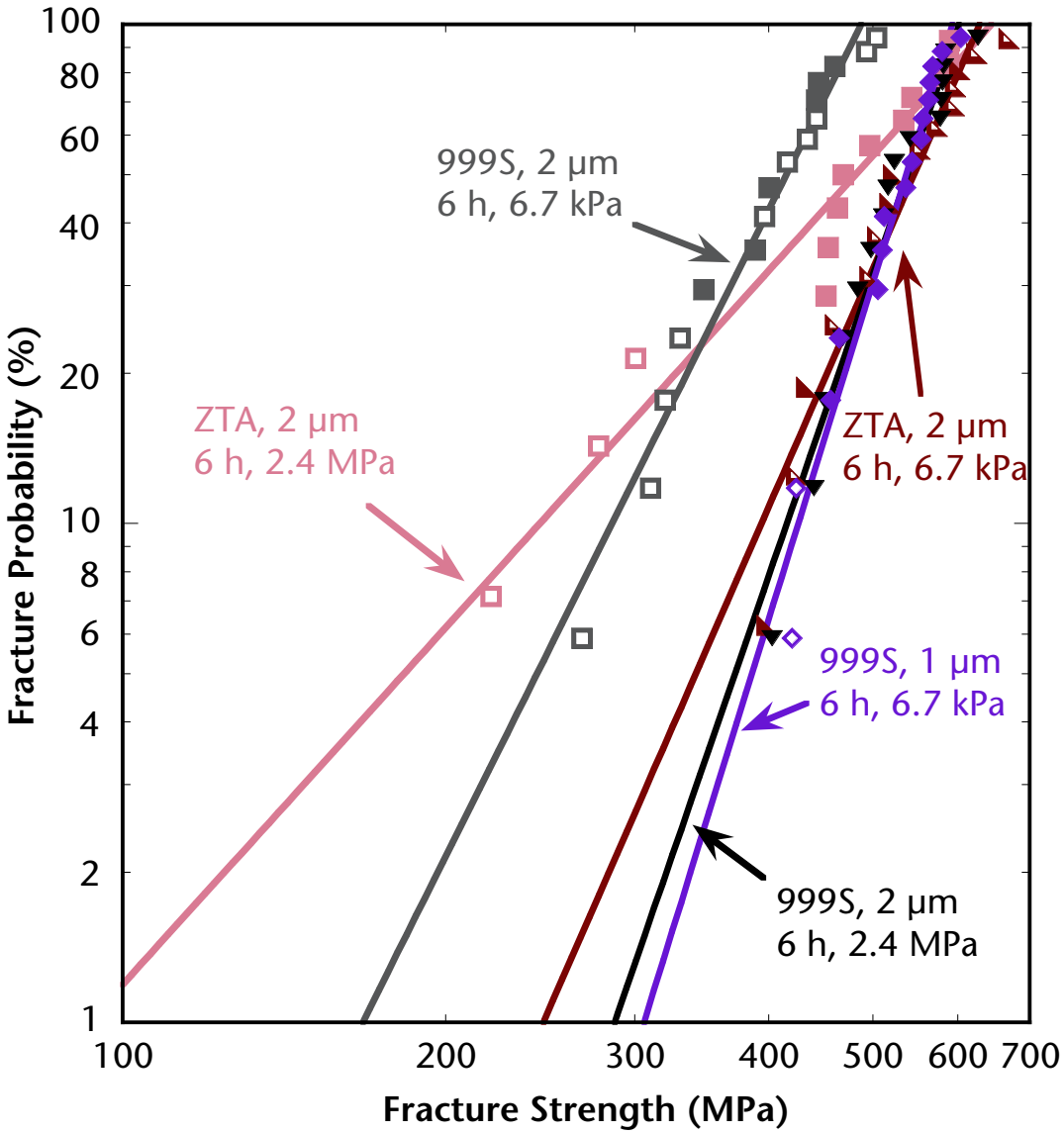

Figure 4.9: Fracture strengths of ZTA vs. 999S when bonded at 1400°C. Open data points represent interfacial fractures, while filled data points represent fractures that occurred in the ceramic.

4.3 Modified Cores for PTLP Bonding

In general, to successfully PTLP bond many ceramics a two-component cladding/core system may not be ideal. While the Ni/Nb/Ni interlayer works very well when used to bond Al_2O_3, the system is rather unique. Ni-Nb liquid has unusual wetting properties on Al_2O_3, while the CTE of Al_2O_3 closely matches that of Nb. For a majority of ceramics, the refractory alloy best suited to minimize residual stresses due to CTE mismatch will not necessarily be the best composition to promote interfacial adhesion. In order to match the core's CTE to that of the bulk ceramic, while also ensuring favorable wetting conditions at the interface, will require the use of modified-core interlayers. Modified-core interlayers have the same core/cladding design as binary interlayers, but employ cores made from alloys of multiple refractory metals, or cores that have surface-coatings. Using modified-core interlayers should allow the interlayer properties to be controlled more closely, ultimately leading to stronger PTLP-bonded materials. To explore the feasibility of modified-core interlayers, high-purity 999W Al_2O_3 was bonded using several different modified-core interlayers, and the results compared to binary core/cladding interlayers.

4.3.1 PTLP Bonding of Al_2O_3 using Binary Interlayers

4.3.1.1 Ni/Nb/Ni Interlayers

As a control group, high-purity 999W Al_2O_3 was PTLP bonded using three different binary interlayers. For all three interlayers, Ni was used as the cladding component. For the core material, the refractory metals Mo, Nb, and V were used. Of the refractory metals available, Mo, Nb, and V were selected due to the similarities between the Ni-Mo, Ni-Nb, and Ni-V phase diagrams, seen in Figure 4.10. In all three phase diagrams: a eutectic liquid forms at <1400°C, no intermetallic phases are thermodynamically stable at 1400°C, and at the bonding temperature there is 2 – 20-at% solubility of Ni in the refractory-metal phase. This allowed the same processing conditions to be used for all three systems. All bonds were fabricated at 1400°C and under a 2.4-MPa applied pressure.

As reported elsewhere[3,137], bonds fabricated using 2-μm Ni/Nb/Ni interlayers failed in the bulk ceramic, as shown in Figure 4.11. The gray box in the figure indicates the bend strengths for monolithic 999W Al_2O_3 processed under the same conditions. The bonded samples had equivalent fracture strengths to those of the monolithic samples. Similar to the ZTA and 999S Al_2O_3 samples discussed in Section 4.2, the interlayer had minimal amounts of Nb_7Ni_6 intermetallic that formed along the metal/ceramic interface due to extrusion of the Ni-Nb liquid phase during bonding. However, sufficient liquid remained to fill interfacial flaws in the Al_2O_3, as seen in Figure 4.12. The liquid's ability to flow into and fill flaws has been attributed to the reduction in contact angle of the Ni-Nb liquid on Al_2O_3. The contact angle decreases from 110° for pure Ni to 90° when Nb is included. In addition, as discussed in Sections 2.3.4 and 4.2, the CTE of Nb and Al_2O_3 are very similar, minimizing the formation of residual stresses during the cooling from the bonding temperature[3,137]. The elastic residual stress in the Nb interlayer was calculated to be ~17 MPa, within the standard of error of the final bond strengths. In addition, Nb is ductile at room temperature, allowing it to deform during fracture, minimizing any stress concentrations that arise due to elastic mismatch during bend testing.

4.3.1.2 Ni/Mo/Ni Interlayers

While the use of Ni/Nb/Ni interlayers resulted in strong, reliable, and robust bonding of Al_2O_3, PTLP bonding using Ni/Mo/Ni interlayers did not. As shown in Figure 4.13, the fracture strength of Al_2O_3 bonded with a 2-μm Ni/Mo/2-μm Ni interlayer was an order of magnitude below that of Al_2O_3 bonded using 2-μm Ni/Nb/2-μm Ni interlayers. The average fracture strength using Ni/Mo/Ni interlayers was 20±7 MPa, while the fracture strength using Ni/Nb/Ni interlayers was 341±28 MPa. Of the original 16 samples bonded using Ni/Mo/Ni interlayers, only 5 survived the fabrication process, and all of those failed at the interface during bend testing.

There are a number of reasons why the Ni/Mo/Ni interlayer system would produce such low fracture strengths. While the phase diagrams for the Ni-Nb and Ni-Mo are similar – at 1400°C, both Ni-Nb and Ni-Mo form a liquid phase, the solubility of Ni in Nb is ~4.5 at% and in Mo is ~2 at%, and no intermetallic phases form in either system – the metal phase diagrams are only a good starting point for determining the viability of a PTLP bonding interlayer. Phase diagrams that include the ceramic – in this case Ni-Mo-Al-O – the wetting properties of the liquid phase, the diffusion mechanism of the MPD, the CTE mismatch, and the mechanical properties of the interlayer all play a role. By these metrics, the Ni/Nb/Ni and Ni/Mo/Ni are found to have a number of crucial differences.

In contrast to the majority of ceramic/metal bonds, Mo has a lower CTE, ~6.4×10^{-6} K^{-1}, than Al_2O_3, ~8.4×10^{-6} K^{-1} between room temperature and 1400°C. In Mo-Al_2O_3 assemblies, if no plastic deformation took place, the residual mismatch stress in the Mo interlayer parallel to the interface, $E\Delta\alpha\Delta T$, was calculated to be ~905 MPa, not including geometric effects. The uniaxial yield stress, σ_0, for pure Mo is ~700 MPa [138], so since $\sigma_0 < E\Delta\alpha\Delta T < 2\sigma_0$, some small-scale plasticity would be expected in the interlayer upon cooling based on Figure 2.4.

Figure 2.4 assumes that the metal interlayer is a ductile phase; however, Mo becomes markedly less ductile near room temperature. The ductile-brittle transition temperature (DBTT) for Mo is ~20–250°C, depending on the impurities present, grain size, and strain rate[139,140]. The presence of O impurities along Mo grain boundaries has been found to decrease the ductility of Mo [141]. While Ni-Mo-O phase diagrams indicate that Ni-Mo solid solutions have effectively no O solubility, the liquid Ni-Mo phase is able to dissolve both O and Al [142-144], suggesting that a small amount of the interfacial Al_2O_3 is incorporated into the liquid phase at 1400° during bonding. This in turn would be a source for O to penetrate the grain boundaries of the interlayer. In addition, the DBTT increases with increasing grain size, and when Ni diffuses along Mo grain boundaries it induces grain-boundary migration, increasing the grain size of the bonded Mo interlayer. These factors combined would suggest that the DBTT for the Mo interlayer would be greater than room temperature. As a result, minimal plastic deformation can occur to reduce the interfacial stresses due to CTE mismatch and elastic mismatch in Ni/Mo/Ni bonds.

With such little plasticity occurring, an assumption of elastic stress states in both the ceramic and metal components is reasonable. In the case of elastic deformation when $CTE_{Metal} > CTE_{Ceramic}$, finite-element analysis by Cao *et al.*[27] found that the equivalent stress near the edge of the bonded assembly had a maximum of $1.1\times E\Delta\alpha\Delta T$. For a more exact

value, finite-element analysis is needed for the case where $CTE_{Metal} < CTE_{Ceramic}$. Finally, it has been shown that during bend testing it is energetically favorable to initiate interfacial fractures at the edge of the bonded assembly, which is not true when $CTE_{Metal} > CTE_{Ceramic}$ [28]. When such edge cracks do initiate, they are in the stable growth regime, similar to indentation cracks, and have no barrier to propagation. This causes bonds where $CTE_{Metal} < CTE_{Ceramic}$ to be less resistant to interfacial failures[27]. The high interfacial stress and the low resistance to interfacial cracking are the likely causes of the bond failures during machining.

The microstructural evolution of the interlayer determines the composition of the interface, which played a role in the low bond strengths. Figure 4.14 shows a micrograph of the bonded Ni/Mo/Ni interface after bend testing; complete interfacial fracture occurred along the opposing face of the Mo core. A secondary phase, the intermetallic Ni_7Mo_7 is present along the interface between the Mo core foil and the Al_2O_3 substrate. From Figure 4.14 alone, it is difficult to determine if it is a continuous phase, but it is evident that the thickness of the Ni_7Mo_7 phase varies significantly along the interface. Figure 4.15 shows a similar fracture specimen that had been mounted in epoxy and polished. The shrinkage of the epoxy and mechanical polishing caused the previously intact interface to delaminate. Fracture occurred both through and along the Ni_7Mo_7 phase. Looking at the fracture surfaces shown in Figure 4.16 and Figure 4.17, the intermetallic phase is continuous over the majority of the metal interface. Voids are present on the metal fracture surface, and no metal pullouts were observed on the ceramic half of the fracture surface, meaning that the voids were present while the assembly was still bonded, prior to testing. Near the tensile edge of the sample, these voids can initiate bond failure.

Minimal amounts of the intermetallic remained on the ceramic fracture surface, as shown in Figures 4.16 and 4.17. This indicates that the interface between Ni_7Mo_7 and the Al_2O_3 was the weak point for fracture, and not the intermetallic phase itself, as was the case with interfacial failures of Ni/Nb/Ni bonded assemblies fabricated under a reduced, 6.7-kPa pressure[119]. An EPMA scan of Figure 4.15 was taken perpendicular to the interface across the interlayer. The results are shown in Figure 4.18. In the scan, there is no indication of the intermetallic phase at the interface. This is most likely due to the fractured nature of the interfacial phase from mounting and polishing the sample prior to EPMA.

As the EPMA results in Figure 4.18 show, the Ni that was absorbed into the Mo core was nearly able to homogenize across the interlayer during the bonding cycle, with an average concentration of 1.2-at% Ni. Since the Ni effectively homogenized during bonding, it is reasonable to assume that it saturated the Mo interlayer as well. 1.2-at% Ni is the solubility limit of Ni in Mo at ~1100°C. During cooling from 1400°C, a portion of the Ni would diffuse back out of the interlayer to the metal/ceramic interface and grain boundaries due to the low cooling rate of 2°C/min, and the decreasing Ni solubility with decreasing temperature. The concentration of Ni homogenized in the core only accounts for 40% of the Ni originally in the cladding layer, leaving 60% of the Ni that either remained at the interface as part of the Ni_7Mo_7 phase, or was extruded during the bonding process.

Figure 4.18 also compares the observed EPMA profile with one that was calculated based on the bonding conditions and the lattice diffusion of Ni in Mo. At 1400°C, Ni has a relatively low lattice diffusivity in Mo, $\sim 2.4 \cdot 10^{-12}$ cm^2/s, compared to that of Ni in Nb,

$\sim 4 \cdot 10^{-10}$ cm^2/s [127]. So when only lattice diffusivity is assumed, the interlayer is not expected to homogenize. This disagrees with the observations in Figure 4.15, but this is not unexpected. In Ni-Mo systems, the Ni-Mo liquid phase that forms completely wets the higher energy Mo grain boundaries[145], rapidly distributing Ni through the polycrystalline Mo foil. There is a large body of literature that demonstrates the usefulness of Ni in the sintering of Mo powders[146-149]. Evidence of the grain boundary wetting is present in Figure 4.14, where the unusual shape of the Ni_7Mo_7 indicates where the liquid resided at the near-interface grain boundaries, causing them to groove. As grain boundary wetting becomes favorable, the Ni-Mo liquid penetrates very rapidly, at nearly 1 μm/s [148]. Once the grain boundaries are wet, Ni diffuses into the Mo core from both the interface and the Mo grain boundaries. As a result, Ni will homogenize more rapidly and completely than expected for redistribution by lattice diffusion alone.

The Ni-Mo liquid film that forms along the grain boundaries also induces grain boundary migration, coarsening the Mo grains much more quickly than if no liquid phase is present. The phenomenon, known as liquid film migration (LFM), will cause the grain boundaries to sweep across the interlayer, with multiple grain boundaries passing over the same location. As the boundaries sweep by, they deposit Ni in the interior of the Mo grains. The excess Ni remains at the interface forming Ni_7Mo_7 secondary phase at the grain boundaries upon cooling[145]. An example of these grain-boundary secondary phases can be seen in Figure 4.14. The Ni profile in Figure 4.18 is not smooth, suggesting that there are concentration discontinuities across the interlayer. Due to the grain-boundary wetting and LFM, intermetallic phases are formed along the grain boundary during cooling, as seen in Figure 4.14. The EPMA has a spot size of ~2 μm, and some of the intermetallic volume can fall into the scanned area, changing the measured composition. The LFM that occurs explains the discrepancy between the profiles expected from lattice-diffusion-controlled Ni redistribution and the actual measured composition profiles in the Ni/Mo/Ni interlayers after bonding.

While LFM and grain-boundary migration cause Ni to redistribute rapidly in Mo, and the Ni-Mo and Ni-Nb phase diagrams suggest that each system can be used in the PTLP bonding of Al_2O_3, the Ni-Mo system has a number of unfavorable characteristics that lead to the formation of weak bonds. At room temperature, Mo has a high effective yield stress and low ductility, making it difficult to dissipate thermal and elastic stresses during bonding and mechanical testing. Since $CTE_{Metal} < CTE_{Ceramic}$ in Mo/Al_2O_3 systems, it is energetically favorable for cracks to form along the metal/ceramic interface, reducing the fracture resistance of Ni/Mo/Ni bonds. Ni_7Mo_7 intermetallics form a nearly-continuous film along the ceramic/metal interface, which provides a minimum-energy fracture path and allows for the formation of strength-reducing voids during solidification, as seen in Figure 4.14. As a result, Al_2O_3 PTLP bonded using Ni/Mo/Ni interlayers had bond strengths an order of magnitude lower than those of Al_2O_3 bonded using Ni/Nb/Ni interlayers.

4.3.1.3 Ni/V/Ni Interlayers

As seen in Figure 4.10, the Ni-V phase diagram is similar to that of the Ni-Nb system. Like Mo, V also has a large difference in CTE when compared to Al_2O_3. However, unlike Mo, V has a larger CTE than Al_2O_3, its ductile-to-brittle transition temperature is well

below room temperature, and it has a much higher solubility for Ni, Al, and O across all temperatures.

The 2-μm Ni/V/2-μm Ni interlayers were much more successful than 2-μm Ni/Mo/2-μm Ni interlayers for PTLP bonding of Al_2O_3. Figure 4.19 shows the bend strengths of bonds fabricated using Ni/V/Ni interlayers with a 2.4-MPa applied pressure compared to the strengths of those made with Ni/Mo/Ni and Ni/Nb/Ni interlayers. The average fracture strength using Ni/V/Ni interlayers was 245±54 MPa, an order of magnitude higher than the fracture strengths of bonds fabricated using Ni/Mo/Ni interlayers. Four of the bonds failed in the ceramic, with an average strength of 327±15 MPa, which is comparable to the strength of monolithic Al_2O_3, 339±47 MPa. However, the majority of the bonds failed interfacially, and at strengths well below those of monolithic Al_2O_3 and bonds using Ni/Nb/Ni interlayers.

Several different factors can contribute to the lower fracture strengths of Ni/V/Ni bonds. The residual stresses in the V foil are an order of magnitude higher than those in a Nb interlayer. Between room temperature and 1400°C, the CTE for V is ~11.7×10^{-6} K^{-1}, larger than the CTE of Al_2O_3, ~8.4×10^{-6} K^{-1}. Using this the elastic stress in plane with the interface is estimated to be $E\Delta\alpha\Delta T$ = 560 MPa. The yield stress for V is ~300 MPa [138], ~0.5× the estimated elastic stress, so according to Figure 2.4, the interlayer is expected to plastically deform. The DBTT temperature is <–80°C [150] and the O solubility in V is >3 at% even at room temperature, so no O grain-boundary embrittlement is expected to occur. Thus, the V is sufficiently ductile to plastically deform. As a result, the equivalent stress in the interlayer is assumed to be equal to the yield stress of V, σ_0 ~ 300 MPa. When $CTE_{metal}>CTE_{ceramic}$ in ceramics bonded with a thin metal interlayer, He *et al.*[28] found that a thin band of tensile stress is imposed in the ceramic perpendicular to the interface at the edge of the bonded structure. This tensile stress, σ_r, has a maximum magnitude that is 0.6-0.7× σ_0, σ_r ~ 200 MPa. In theory, if a critical-sized flaw for fracture was located in this band, the material would be expected to fail in the ceramic at a bend stress of ~150 MPa, 200 MPa lower than the strength of monolithic Al_2O_3. The thickness of this tensile stress band is equal to the thickness of the interlayer itself, ~125 μm, and the magnitude of the tensile stress diminishes rapidly on either side of this band. Assuming a penny-shaped flaw, the critical flaw size for the failure of a typical Al_2O_3 monolithic beam is ~25 μm, meaning that at a minimum, a 50-μm diameter flaw would need to reside entirely within the tensile residual stress band in order to fail at a bend stress of 150 MPa. While no information was available on the flaw-size distribution for the material, the fact that all four of the ceramic fractures had fracture strengths within a standard deviation of the monolithic Al_2O_3 fracture strength provides anecdotal evidence that σ_r has minimal influence on the fracture strengths of Al_2O_3 bonded using Ni/V/Ni interlayers. A larger number of ceramic fractures of Ni/V/Ni bonded Al_2O_3 would be needed to more conclusively determine the role of σ_r on the fracture strength of Ni/V/Ni bonds.

When $CTE_{metal}>CTE_{ceramic}$, Cao[27] has shown that cracks originating and propagating along the ceramic/metal interface are energetically unfavorable. However, this assumes that the interfacial adhesion between the metal and ceramic are is at least as high as the ceramic and metal self-adhesion. In the Ni/V/Ni bonds, the large number of interfacial failures suggests that the interfacial adhesion was relatively low, and thus the energetically favorable path for crack propagation. Figure 4.20 shows a micrograph perpendicular to the Al_2O_3-V interface.

Similar to the Ni/Nb/Ni system, there is no continuous intermetallic layer along the interface. However, Figure 4.21 shows a number of flaws at the interface after bonding, which can help to weaken the interface.

In images of the fracture surface, shown in Figure 4.22, small discontinuous regions of intermetallic are present only on the V fracture surface, not on the ceramic side. The Ni-V intermetallic phase, thought to be Ni_3V_7, exhibits minimal ductility and has high hardness[151,152], which would inhibit the relaxation of any stress concentrations present at the interface. The lack of any metal phase on the ceramic fracture surface is further evidence that the interface itself was the weakest part of bonded assembly. The presence of an intermetallic was not expected however, due to Ni having a higher solubility-diffusivity product in V than in Nb, which was expected to lead to rapid Ni redistribution in the V core during bonding. While the lattice diffusivity of Ni in V, $\sim 8 \cdot 10^{-10}$ cm^2/s, is similar to that of Ni in Nb, $\sim 4 \cdot 10^{-10}$ cm^2/s, the solubility of Ni at 1280°C is much higher in V, ~29 at%, than in Nb, ~4.5 at%. As a result, using lattice diffusion alone, the interlayer was expected to homogenize. The EPMA scan across the V interlayer indicates that the Ni completely homogenized during the bonding process, as shown in Figure 4.23.

A simple lattice diffusion calculation suggests that Ni diffusion occurs so quickly that by the time the peretectic temperature of, 1280°C, is reached, ~90% of the Ni has already been incorporated into the V core, and that by 1320°C, all of the Ni has been incorporated into the core layer. However, this calculation does not take into account the expected formation of V-Ni intermetallic phases below 1280°C, all of which will have a different interdiffusion rate for both Ni and V. Below 1220°C, Ni_xV_y phases will form along the interface between the Ni cladding and the V core. Since the melting points of the Ni_xV_y phases are well below that of V, the diffusion rate of Ni in Ni_xV_y is not expect to be the rate-limiting factor in the incorporation of Ni into the V core. The most likely of these phases to form, Ni_3V_7, is 30-at% Ni, which would incorporate more Ni from the cladding layer than in the simple diffusion model described previously. Since more of the Ni would be consumed, it is likely that all of the Ni is incorporated into the Ni_3V_7 phase prior to reaching 1220°C, the temperature at which a Ni-V liquid is formed. Thus from 1220°C to 1280°C, little to no liquid would be available to fill in any strength-reducing flaws and voids at the interface, and the fraction of Ni in the intermetallic phases would decrease as Ni continued to redistribute into the V core. At 1280°C, Ni_3V_7 becomes thermodynamically unstable, and the majority of whatever intermetallic phases remained would melt, forming a liquid phase. However, since Ni diffusion in V is expected to be the limiting diffusion rate, the previous calculation that >90 at% of the Ni has already homogenized in the V core by 1280°C is still expected to be valid, despite the presence of the intermetallic phases. As a result, very little liquid-phase is expected to form along the interface. The combination of interfacial flaws, the formation of intermetallics, and the rapid redistribution of Ni into V appear to be the cause of lower overall bond strength of Al_2O_3 bonded using Ni/V/Ni interlayers.

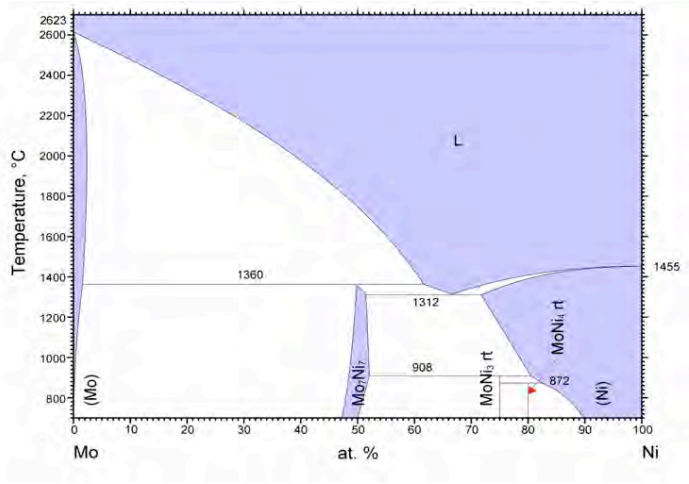

(a)

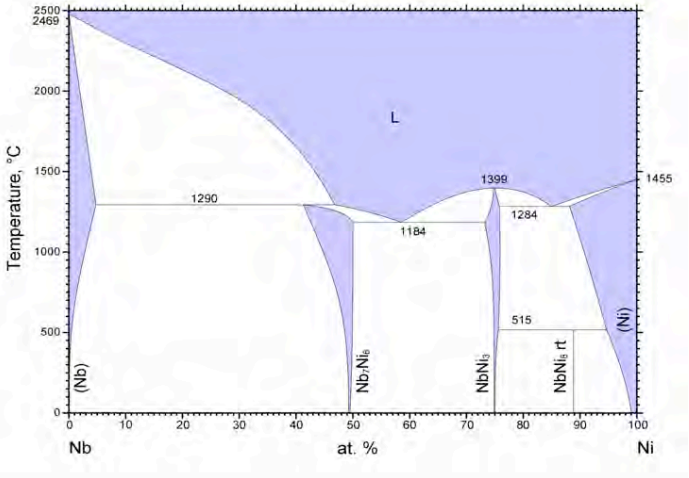

(b)

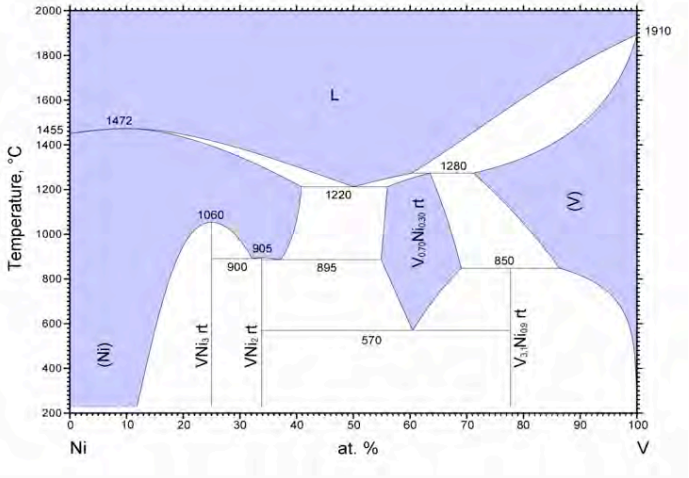

(c)

Figure 4.10: The (a) Ni-Mo [153], (b) Ni-Nb [125], and (c) Ni-V [154] phase diagrams. All three have a eutectic transition below 1400°C, no intermetallic phases that form at 1400°C, and have non-negligible Ni solubility in the refractory-metal phase.

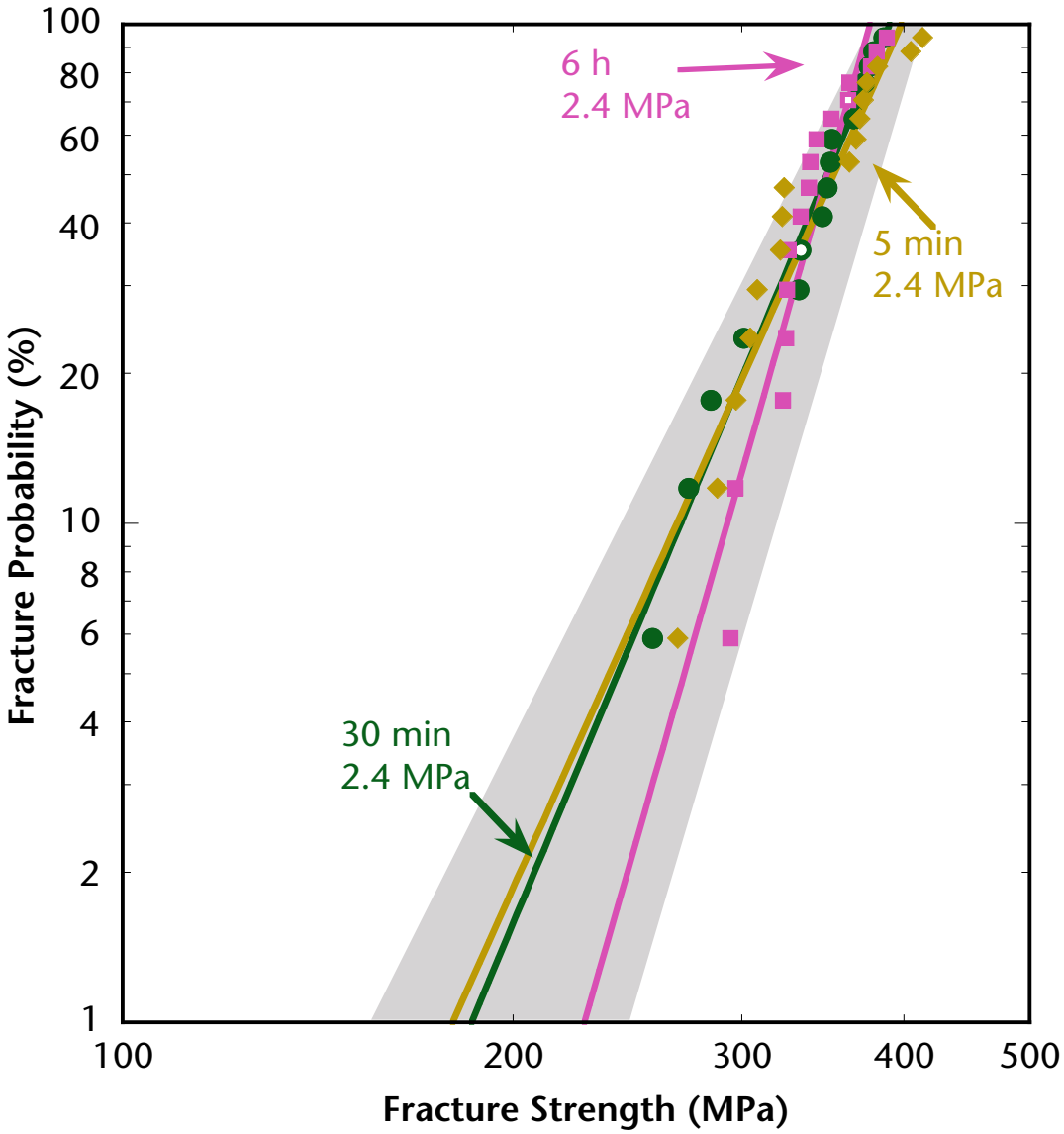

Figure 4.11: Fracture strength of Ni/Nb/Ni bonds of 999W Al_2O_3 fabricated at 1400°C under a 2.4-MPa applied pressure. 5 min and 6 h bonds are from Hong *et al.*[137].

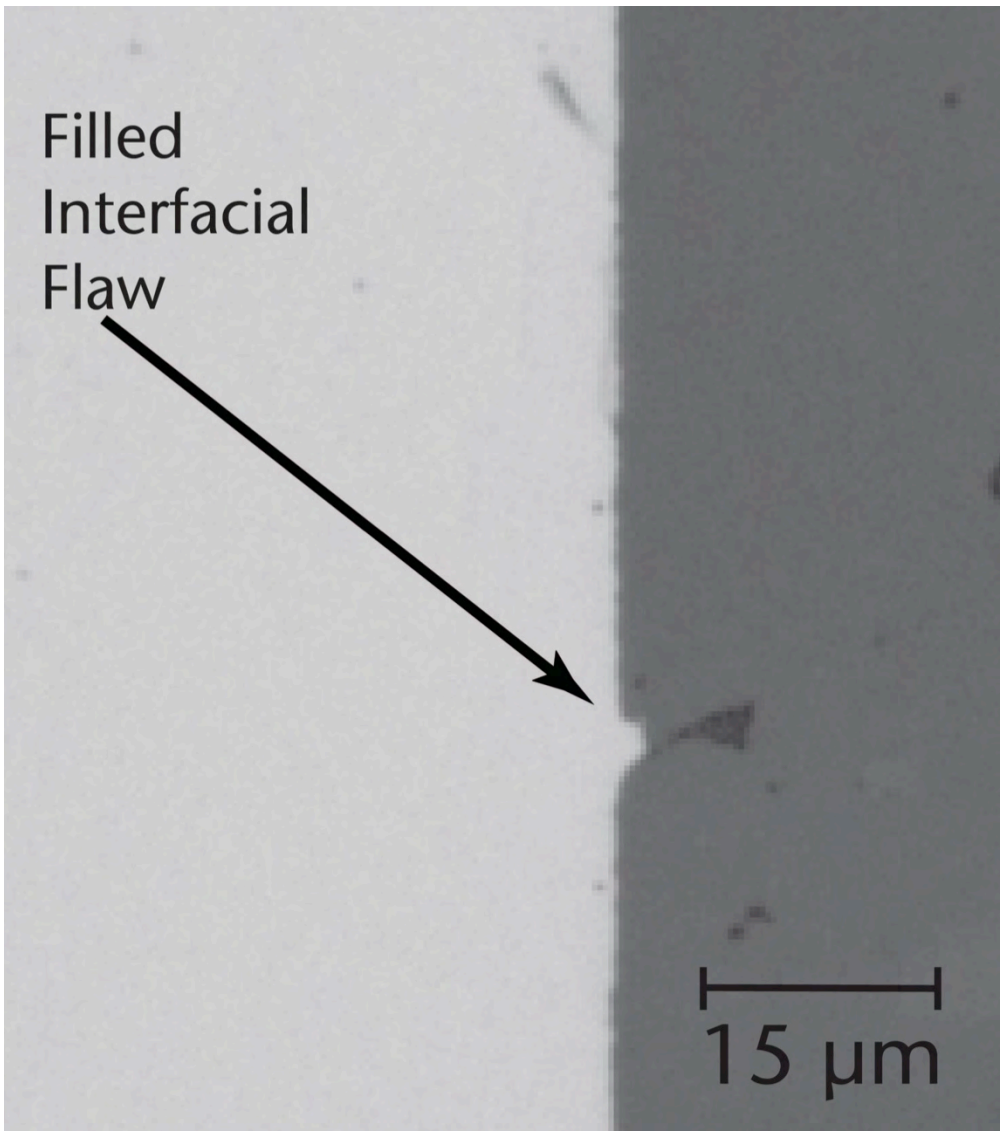

Figure 4.12: Nb/Al_2O_3 interface of Al_2O_3 bonded using a Ni/Nb/Ni interlayer. The Nb is the lighter phase on the left. Note that the Nb interlayer has filled in the flaw in the Al_2O_3 interface during the bonding process.

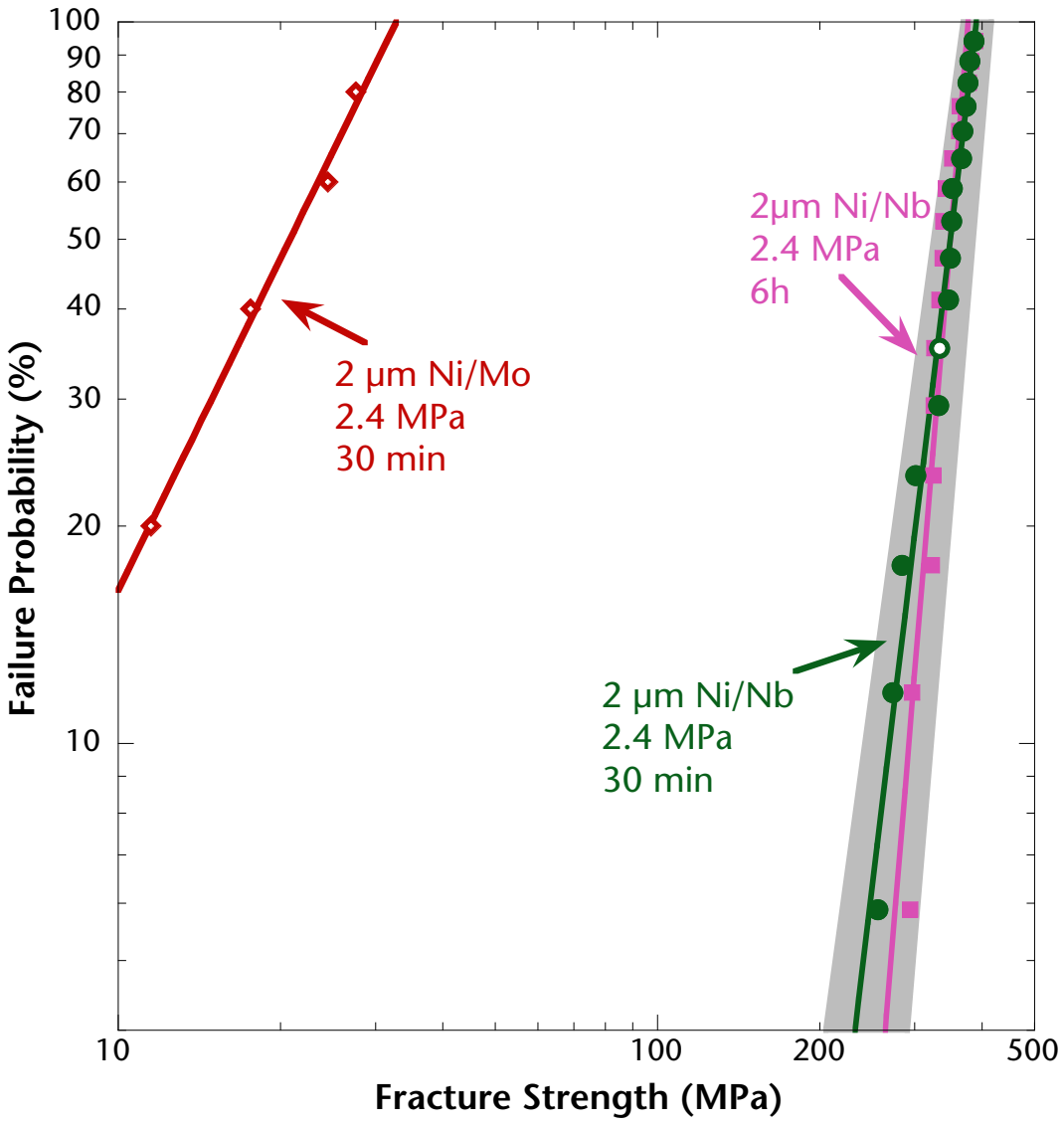

Figure 4.13: Fracture strengths of Al_2O_3 bonded using Ni/Mo/Ni and Ni/Nb/Ni interlayers. Note the change in scale on the x-axis compared to other fracture strength plots.

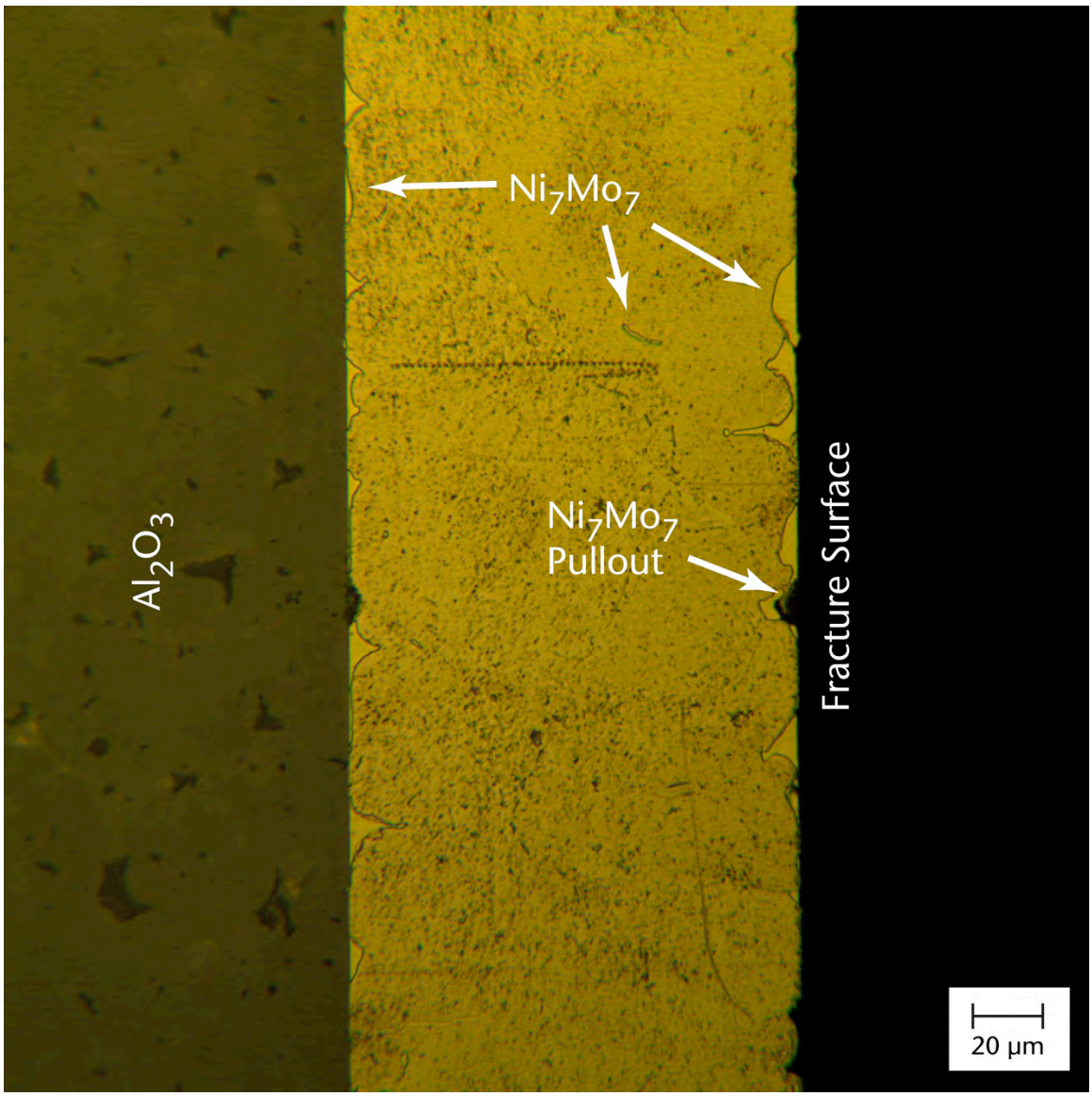

Figure 4.14: Ni/Mo/Ni bond after bend testing. Interfacial fracture occurred along the right interface. Ni_7Mo_7 secondary phase is present along both interfaces as well as within the Mo interlayer.

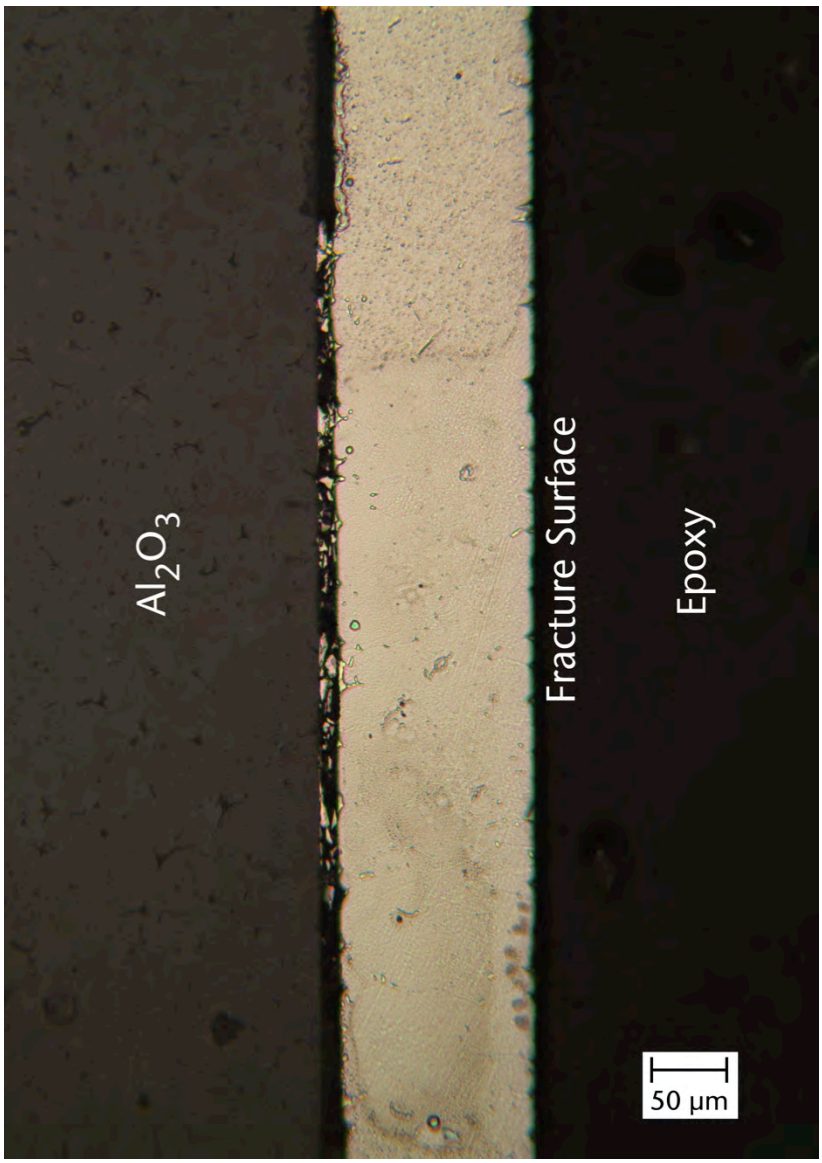

Figure 4.15: Fractured Ni/Mo/Ni bond that has been mounted in epoxy and polished. The combined action of the epoxy drying and the polishing caused the leftmost interface to delaminate. The remaining Ni_7Mo_7 intermetallic is visible in the delaminated region.

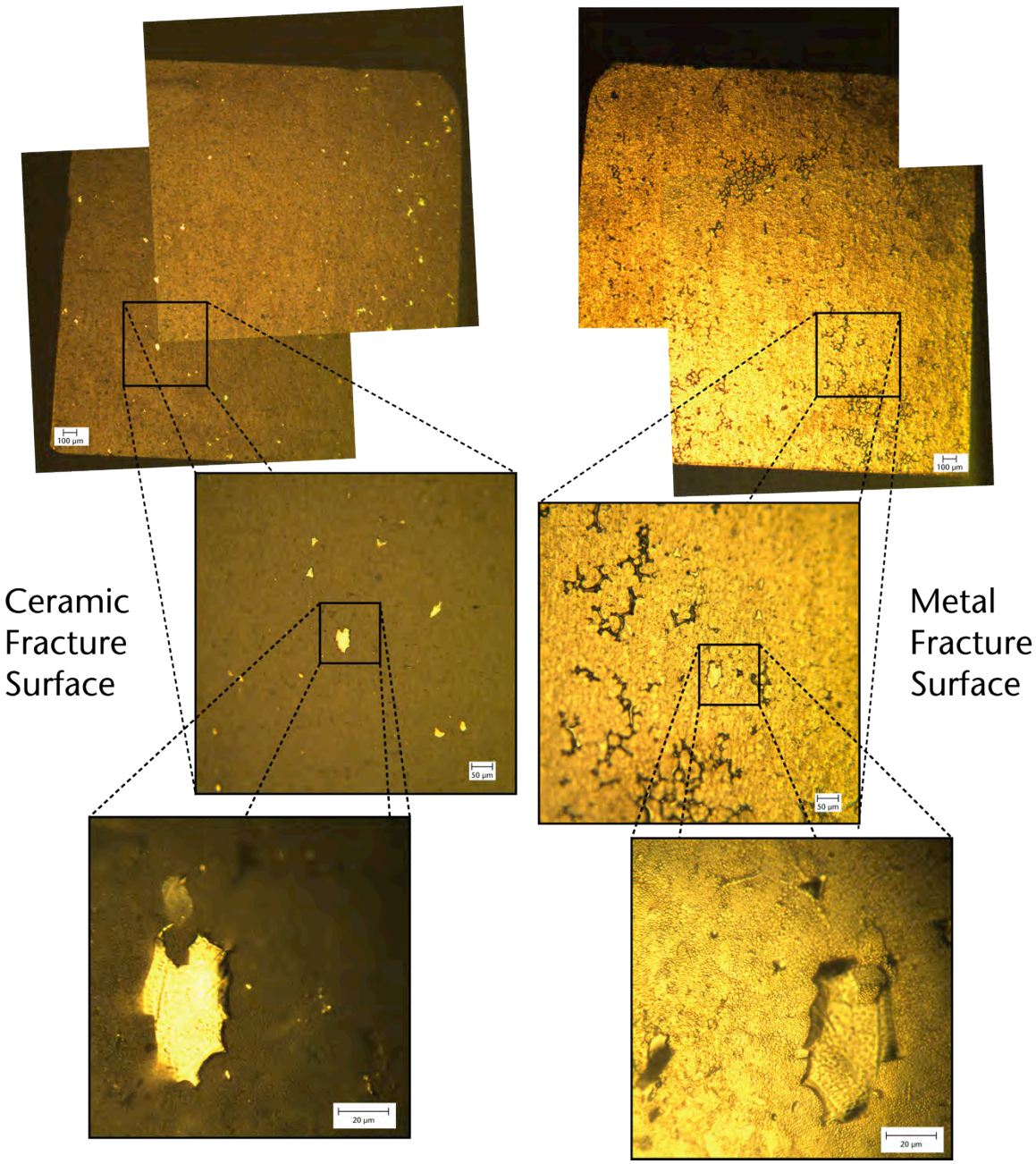

Figure 4.16: The (a) ceramic and (b) metal fracture surfaces of Al_2O_3 bonded using a Ni/Mo/Ni interlayer. At the bottom left, Ni_7Mo_7 remaining on the ceramic interface is shown, and on the right is the corresponding void left on the metal interface.

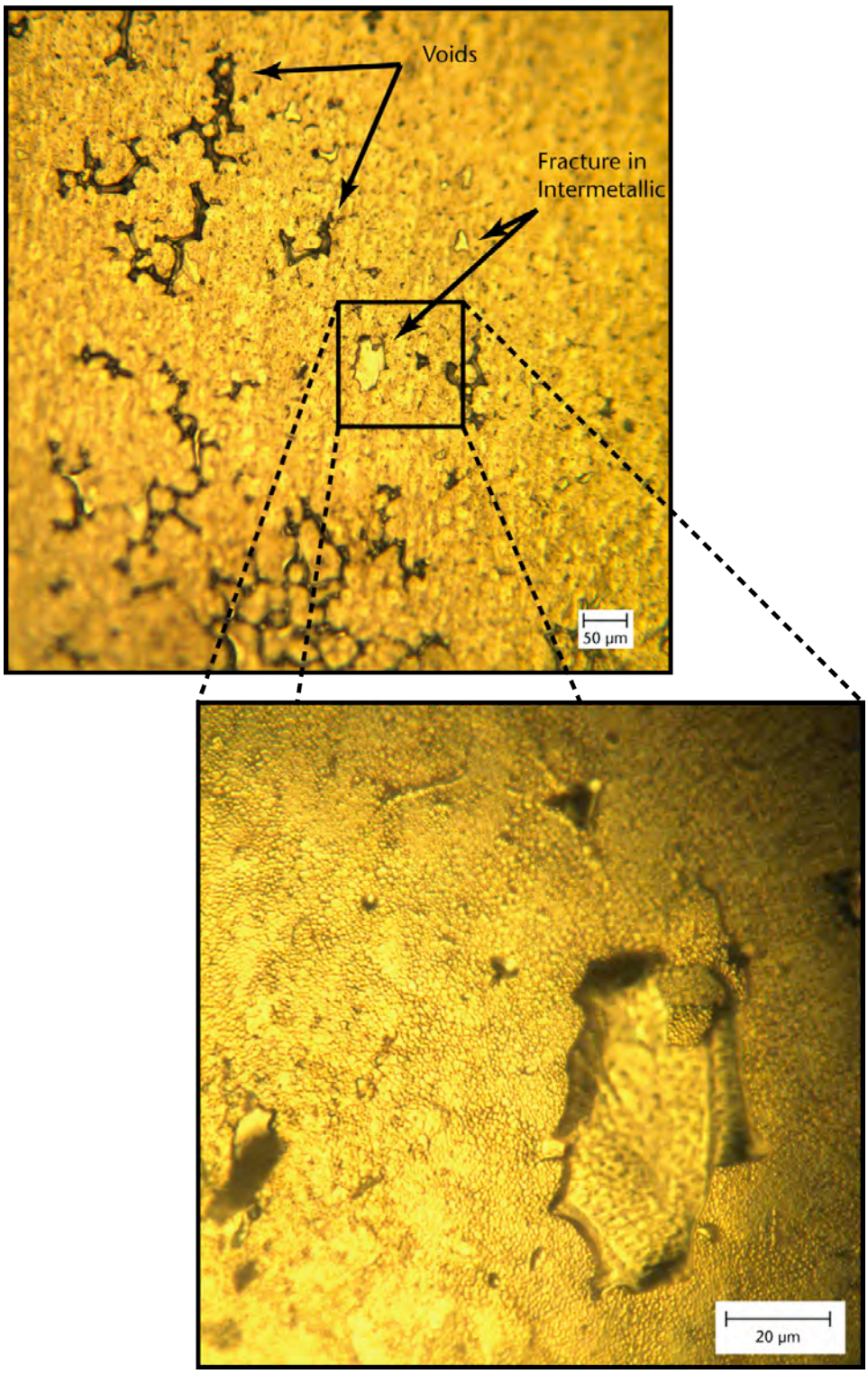

Figure 4.17: Metal fracture surfaces from Figure 4.16. In the top image, voids are visible at the interface. In the bottom image, a region of Ni_7Mo_7 pullout is shown. The metal interlayer indicates that a continuous layer of Ni_7Mo_7 forms at the interface, with varying thickness.

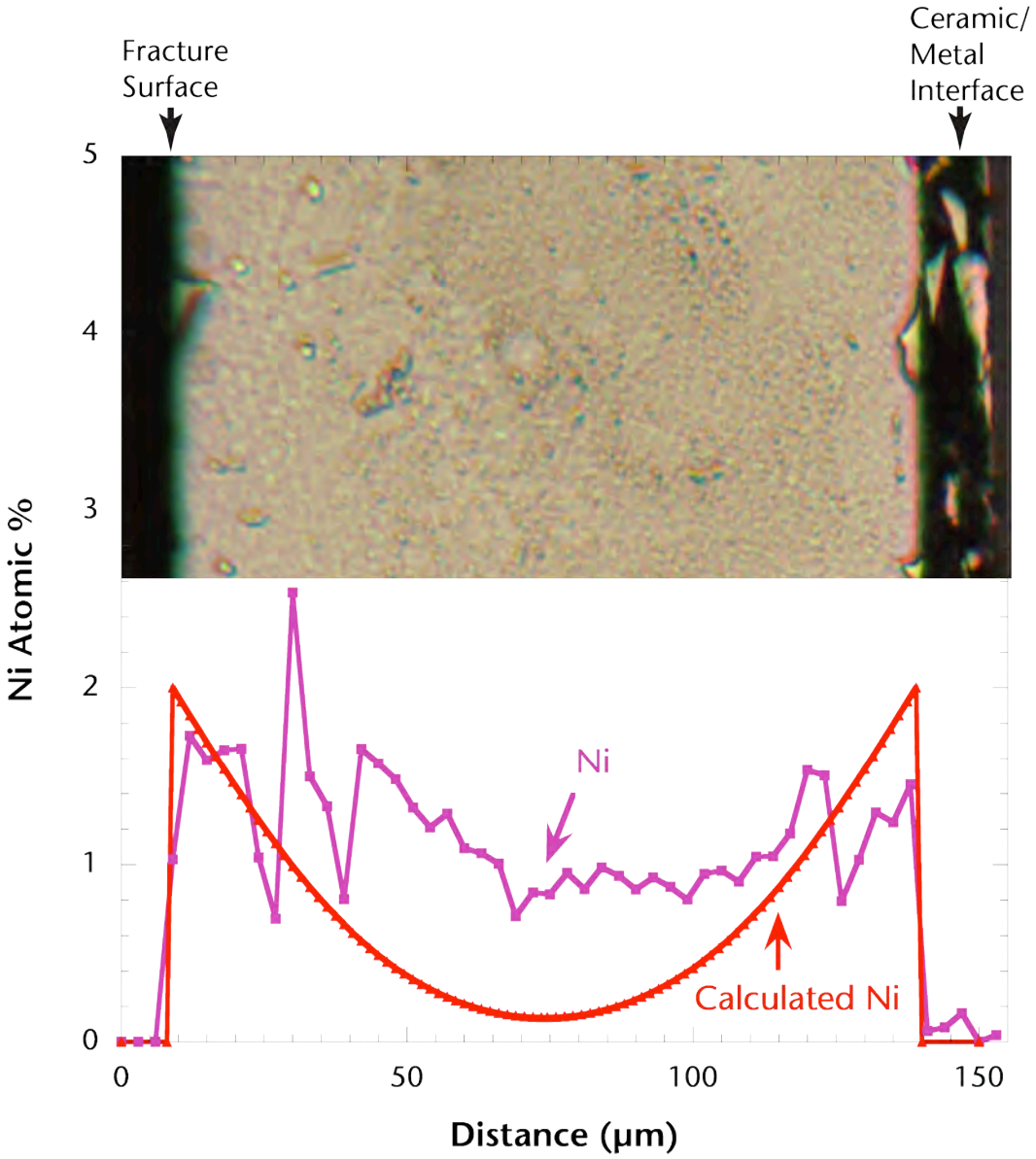

Figure 4.18: EPMA diffusion scan of Al_2O_3 bonded using a Ni/Mo/Ni interlayer for 30 min at 1400°C under a 2.4-MPa pressure, as shown in Figure 4.16, compared with a calculated diffusion profile based on lattice diffusion of Ni in Mo.

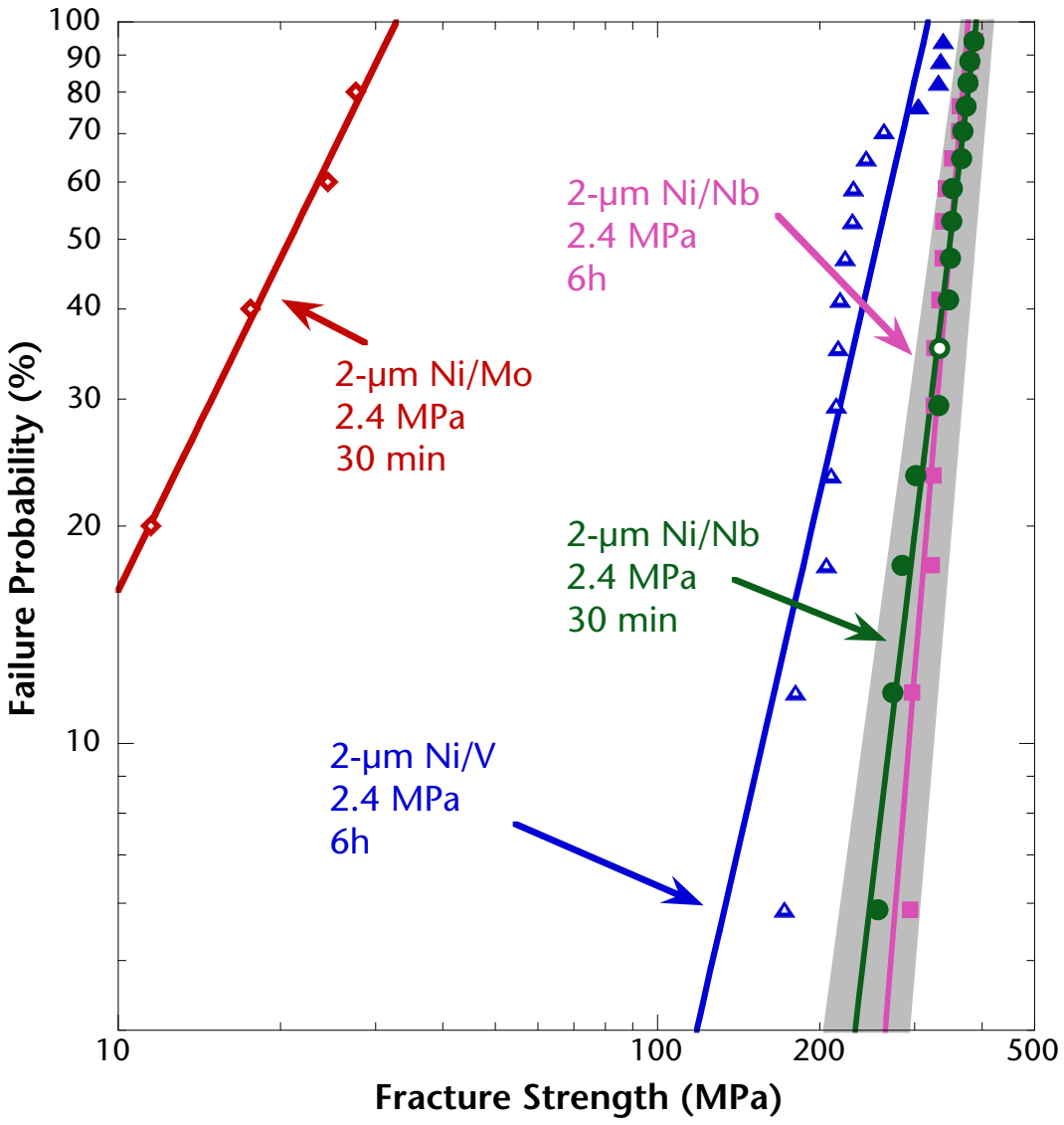

Figure 4.19: Bend strengths of Al_2O_3 bonded using Ni/Nb/Ni, Ni/V/Ni, and Ni/Mo/Ni interlayers. Note the change in scale on the x-axis compared to other fracture strength plots.

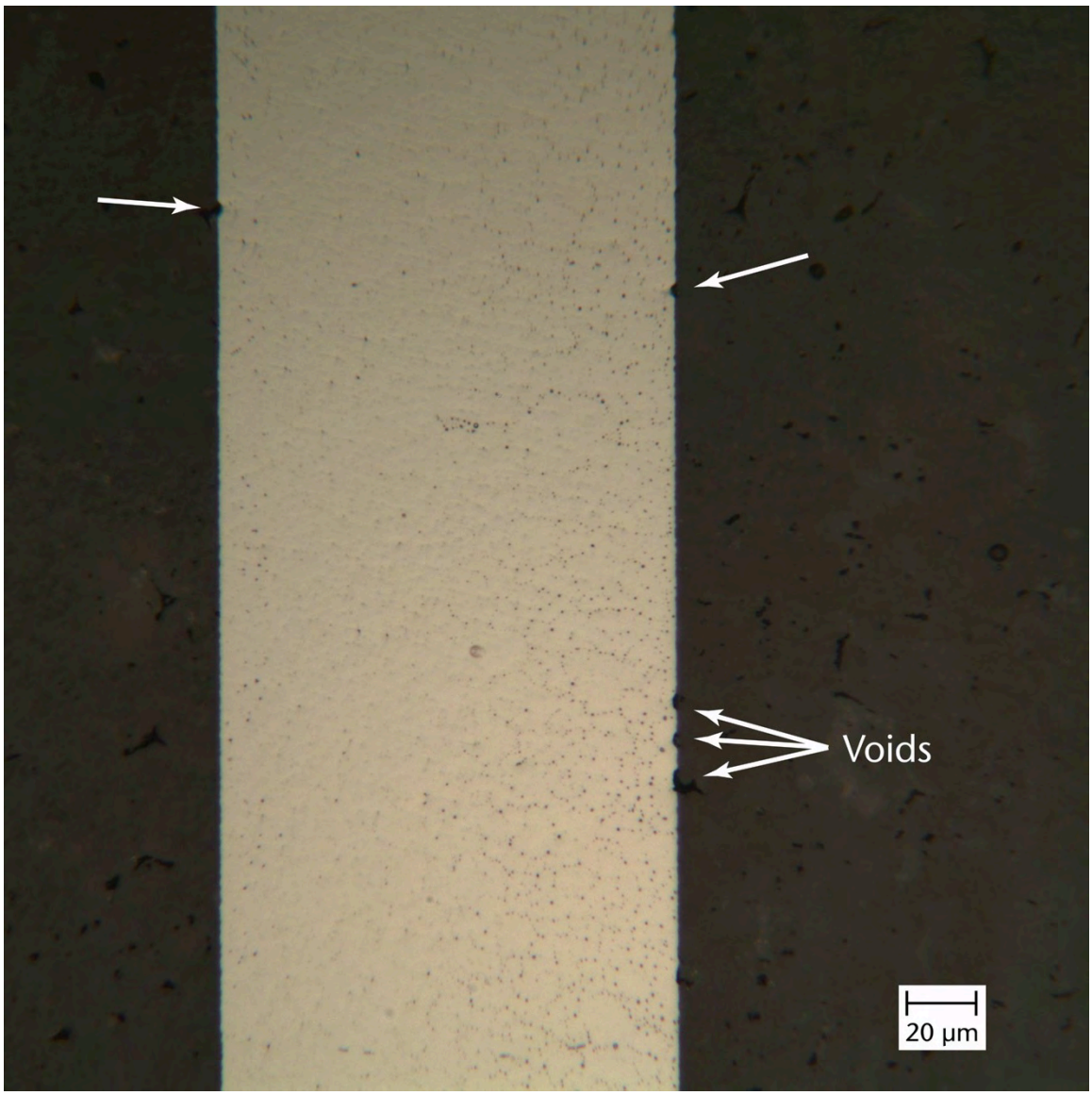

Figure 4.20: Interlayer in Al_2O_3 bonded using Ni/V/Ni. Voids exist at the interface.

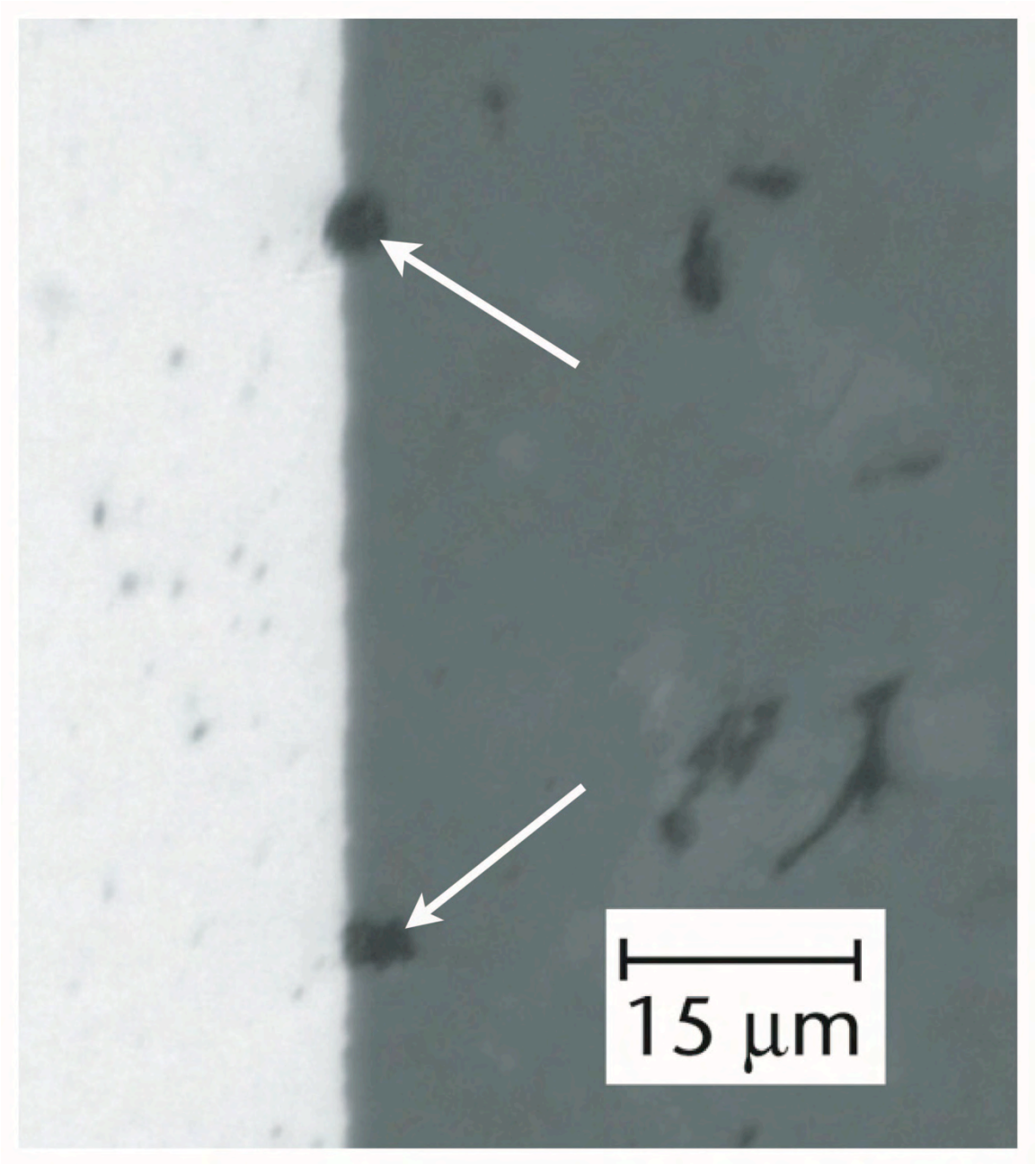

Figure 4.21: Interface of Al_2O_3 bonded using a 2-µm Ni/V/2-µm Ni interlayer. Note the presence of voids along the interface after bonding.

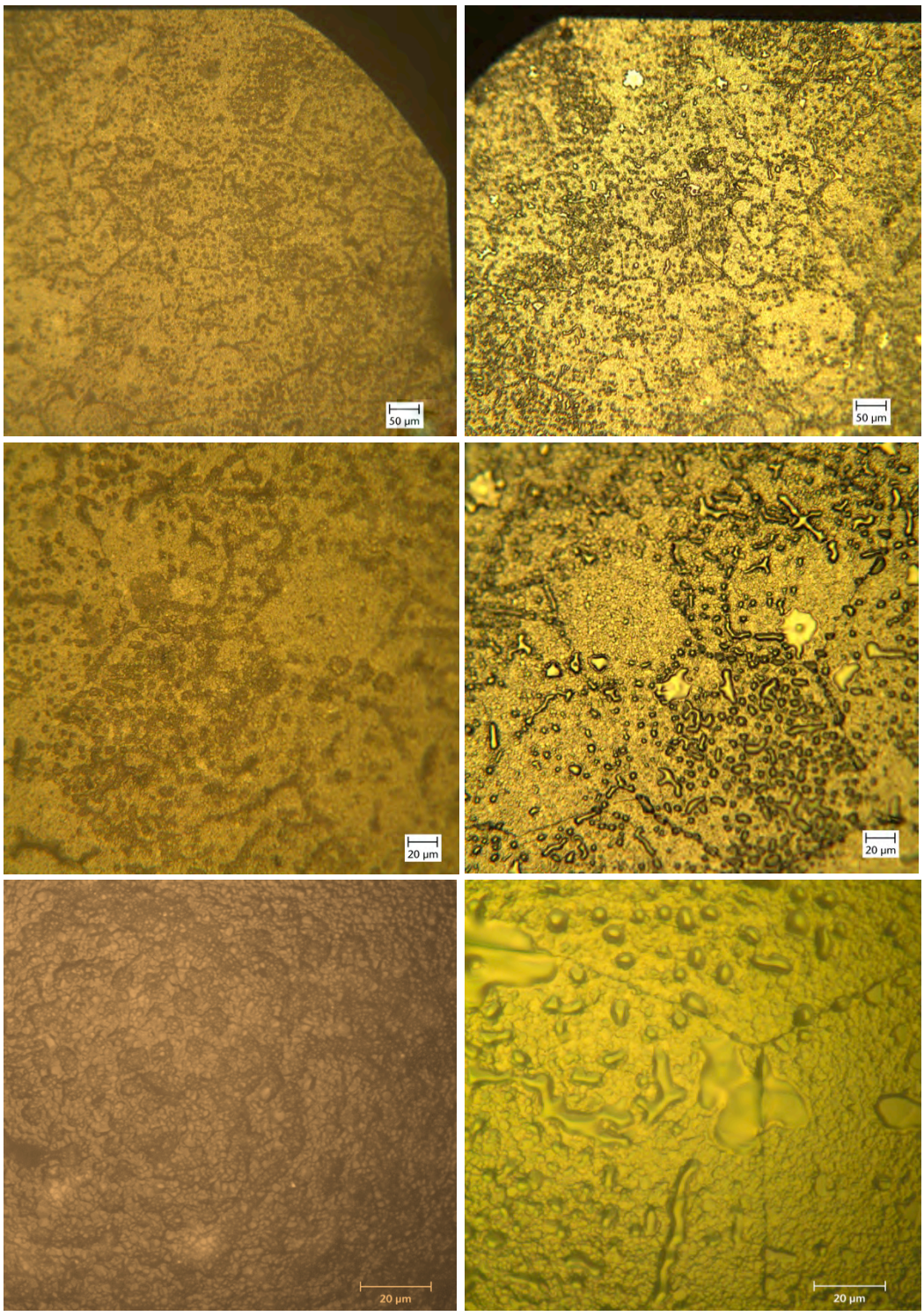

(a) (b)

Figure 4.22: The (a) ceramic and (b) metal fracture surfaces of Al_2O_3 bonded with a Ni/V/Ni interlayer. The magnification increases from top to bottom. A secondary phase is visible on the metal surface. The pocketed surface of the ceramic is from dissolution of Al_2O_3 into the metal interlayer.

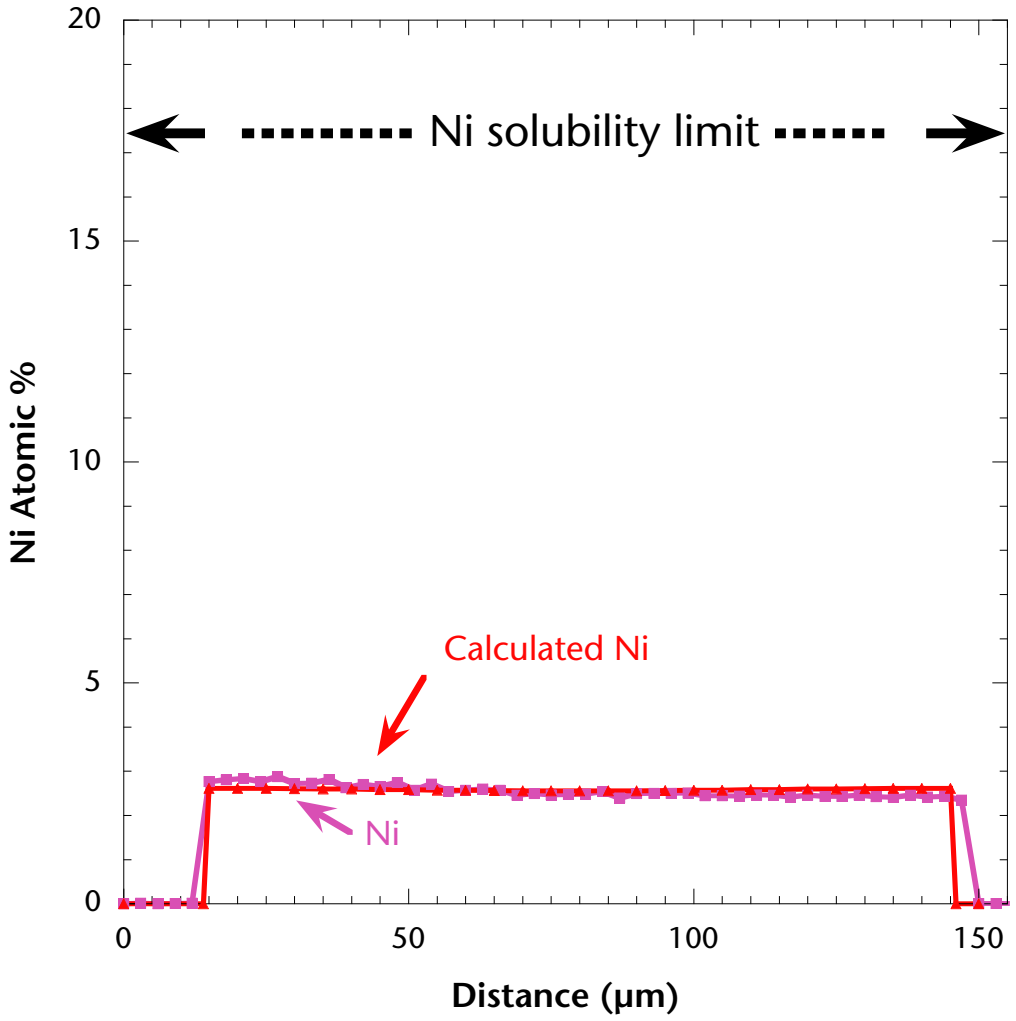

Figure 4.23: Diffusion of Ni in V core after bonding for 6 h at 1400°C under a 2.4-MPa pressure.

4.3.2 PTLP Bonding of Al_2O_3 using Nb-Surface-Modified Cores

4.3.2.1 Ni/Nb/Mo/Nb/Ni

As discussed in Section 4.1, compared to that of Ni-Nb alloys, the contact angle of 42-at% Ni-Mo alloy is relatively high, 120°, on Al_2O_3 substrates. As discussed in Section 2.1.1, a decrease in the contact angle of a liquid is associated with an increase in the W_{ad} of the interface. Since PTLP-bonded Al_2O_3 using Ni/Mo/Ni binary interlayers fractured at the metal/ceramic interface, resulting in very low fracture strengths, it was hypothesized that improving the contact angle of the liquid-phase during PTLP bonding could improve the interfacial strength, and thus the fracture strength of Mo-core bonds. In wetting experiments, a 62-at% Ni-19-at% Nb-Mo ternary alloy had a contact angle of ~90°, a significant reduction. Attempts were made to use a 2-μm Ni cladding and a 2-μm Nb-coated modified Mo core to improve the wetting properties of the liquid phase during the bonding process.

The addition of the 2-μm-thick Nb film, which is ~2.6-at% Nb-Mo when the interlayer has fully homogenized, does little to alter the mechanical properties of the Mo-foil. Pipitz *et al.*[155] found that when 3-at% Nb was in solution in Mo, the tensile strength of the alloy increased ~12%, and the DBTT increased as well. As a result, assuming that the Mo interlayer is elastic with little ductility, as was done for Ni/Mo/Ni bonds in Section 4.3.1.2, is reasonable. The CTE of the Mo foil would not change appreciably despite the addition of Nb to the solution, remaining at $\sim 6.4\times10^{-6}\,K^{-1}$. Thus, the effective elastic stress in the foil due to bonding, $E\Delta\alpha\Delta T$, would be equivalent to that of Ni/Nb/Ni bonds, ~905 MPa. Since the residual stresses were equivalent, it was expected that the bond strengths using Ni/Nb/Mo/Nb/Ni interlayers would be similar or higher than those using Ni/Mo/Ni interlayers. However, this was not the case. Instead, none of the fabricated bonds survived the machining process and all bonds failed within the interlayer, in a near-interfacial intermetallic layer.

Figure 4.24 shows a macroscopic view of the ceramic fracture surface of the failed Ni/Nb/Mo/Nb/Ni bonds. The interlayer foil did not extend to the edge of the substrate, leaving an unbonded region, which is circled in the figure. The failure of the assembly may partially be due to this unbonded region acting as a stress-concentrating crack. The unbonded region has a smooth surface, as shown in Figure 4.25, and is not in plane with the fracture surface, which was raised in respect to the region of unbonded Al_2O_3. In Figure 4.26, the metallic appearance of the ceramic fracture surface indicates that the fracture path was not along the metal/ceramic interface as was the case in the Ni/Nb/Ni and Ni/Mo/Ni interfacial failures, but instead within a metallic phase. Attempts were made to determine the thickness of the remaining metal phase on the ceramic interface by examining the ceramic bulk perpendicular to the fracture surface, but the raised metallic phase was not easily discernable by optical microscopy. This suggests that the metallic phase remaining on the ceramic fracture surface is very thin, <5 μm, as a very rough estimate. In both the Ni/Mo/Ni and Ni/Nb/Ni systems, the Al_2O_3 fracture surfaces were smooth, other than small regions of intermetallic pullout remaining on the surfaces. In contrast, for bonds using Ni/Nb/Mo/Nb/Ni interlayers the fracture surface on the ceramic side has long, shallow, crack-like voids on the surface, as shown in Figure 4.26. Deeper crack-like voids also appear on the metal fracture surface, as seen in Figure 4.27. An examination of the fracture surfaces indicated that the voids on both fracture surfaces were the two sides of the same void structure. Figure 4.28 shows a higher

magnification of the ceramic fracture surface, and the metallic phase on the surface. Since the bond failed during processing, it was not possible to take micrographs of the bonded interlayer perpendicular to the fracture surface. As a result, we were not able to examine the interlayer in cross-section for further evidence of a secondary phase at the interface, but the fracture surface micrographs strongly suggest that a second phase formed at the interface and fracture occurred within that phase.

To gain insight into how the interlayer microstructure developed, a composition profile was calculated for the case of lattice diffusion, as seen in Figure 4.29. In this graph, an assumption is made that the diffusion of Ni and Nb do not influence the rate of the other, which is not strictly correct. However, it does provide some indication of how the interlayer evolves in Ni/Nb/Mo/Nb/Ni bonds. As calculated, the 2-μm-thick Nb film is not fully incorporated into the Mo core after the entirety of the bonding cycle, while the Ni is able to nearly homogenize across the interlayer. Neglecting extrusion of any liquid phase, 2-μm Ni and 2-μm Nb are equivalent to 4.3-at% Ni and 2.6-at% Nb, respectively, when fully homogenized in the Mo core. At 1400°C Ni only has a solubility of ~2 at% in Nb-containing Mo, as seen in the ternary Ni-Nb-Mo phase diagram in Figure 4.30a. As a result, a fraction of the Ni would also remain at the interface throughout the bonding cycle.

Figure 4.30 was also used to determine an approximate evolution of the interfacial composition during bonding. We make the assumption that Mo diffusion through the Nb layer is sufficiently slow such that the initial liquid-phase composition is the Ni-Nb eutectic composition, marked point 1 in Figure 4.30a. At 1400°C, Mo is incorporated into the liquid phase until a Ni-Nb-Mo liquid phase stabilizes at the liquidus composition, marked point 2. If the bond was quenched to room temperature, Figure 4.30b shows that point 2 lies in a 3-phase region, in equilibrium with the (Ni_3Nb, Ni_3Mo) phase, the Nb-Mo phase, and the Ni_6Nb_7 phase. In practice, the Ni in the remaining liquid phase would begin to homogenize across the interlayer, decreasing the fraction of Ni in solution. As this occurred, the liquid composition is expected to follow the liquidus towards point 3, at which time Ni has saturated the core layer. If quenched from point 3, Figure 4.30b shows that the composition lies in the two-phase region between Ni_6Nb_7 and the Ni-Mo solid solution and since it is closer to the Ni_6Nb_7 phase on the phase diagram, a substantial fraction of the composition would form the intermetallic phase. In either case, the final interfacial composition lies in a region that is in equilibrium with intermetallic phases. This is consistent with the observation that an intermetallic phase formed during cooling.

The Ni-Nb and Ni-Mo intermetallic phases that form would be expected to be brittle at room temperatures[156]. Since half of the Ni cladding, ~2 at%, is incorporated into the core during bonding, the remaining liquid would remain at the interface. Some of that liquid is potentially extruded from the interface during the bonding process. Due to LFM, additional Ni would be redistributed to the grain boundaries, further reducing the interfacial liquid-film thickness. As a result, intermetallic would exist along the grain boundaries, and the intermetallic layer that forms at the interface during cooling is expected to be quite thin, at the most ~2 μm. A lack of interlayer ductility and high stresses due to thermal shrinkage are likely to have caused the crack-like voids seen in Figure 4.27. The presence of these cracks and the additional stresses from machining could be sufficient to cause crack bridging to occur, leading to interfacial failure during processing. This is consistent with the proposed idea that the

bonds failed within the intermetallic phase, and not along the metal/ceramic interface as they did in the Ni/Mo/Ni assemblies.

While the addition of a 2-μm-thick Nb coating on Mo cores was not found to improve the strength of Al_2O_3 assemblies bonded with Mo cores, the presence of the intermetallic phase is an indication that the interlayer design could be further altered in order to improve the bond strength. Since not all of the Ni and Nb were able to incorporate into the Mo interlayer, reducing the initial thicknesses of both could help reduce or eliminate the formation of intermetallics at the interface. A potential experiment would be to join Al_2O_3 using a 1-μm Ni/0.15-μm Nb/Mo/0.15-μm Nb/1-μm Ni interlayer. If instead of a 2-μm Nb coating, a coating of 0.15-μm Nb was deposited on the Mo core foil, then the Ni-Nb-Mo liquid that formed during bonding would be expected to be ~5-at% Nb. This is a sufficient amount of Nb to reduce the contact angle, while the decrease in quantity of Nb would allow the Nb to fully incorporate into the Mo core during processing. In fact, the 0.15-μm Nb coating would be expected to be incorporated into the Mo core within 10 min of reaching the soak temperature, and would spend the remaining portion of the 6 h soak time becoming more homogenized across the interlayer. The Ni cladding would also be reduced from 2-μm Ni to 1-μm Ni. Fully homogenized the interlayer is ~2.1-at% Ni, which is approximately the solubility limit for Ni in the Mo core. As a result, using a 1-μm Ni/0.15-μm Nb/Mo/0.15-μm Nb/1-μm Ni interlayer almost all of the Ni and Nb would be expected to be incorporated into the core layer during bonding, as shown in Figure 4.31. However, by reducing the thickness of the Ni cladding, the resultant thickness of the liquid phase would decrease by half as well. As a result, the reduced quantity of liquid has the potential to no longer be sufficient to fill the interfacial gaps and voids, causing strength-reducing voids to remain at the interface. To find the most desirable thickness of the Ni and Nb layers, iterative testing of several different designs may be necessary. The results of this experiment would be beneficial in two ways: help determine whether the intermetallic phase only forms due to excess Ni and Nb at the interface; and if no intermetallic forms, help quantify the contribution of Nb to interfacial strength in Al_2O_3 bonds.

4.3.2.2 Ni/Nb/V/Nb/Ni

Because Al_2O_3 bonded using Ni/V/Ni interlayers was also found to fail interfacially, PTLP bonds using Nb-surface-modified V cores were fabricated. Figure 4.32 shows the EPMA measurements across the interlayer. The Nb and Ni components were found to homogenize in the V core during bonding, similar to what was observed in the Ni/V/Ni bonds in Section 4.3.1.2. Nano-indentation was done across the interlayer to determine the modulus of the V interlayer, as shown in Figure 4.33. The modulus of the homogenized V interlayer was found to be uniform across the interlayer, with an average of 163±15 GPa. This is higher than reported values of the modulus of pure V, which is ~125 GPa [157]. There was no data available as to how solutes increased the modulus of V metals in the literature, but Harris[158] andVasil'eva *et al.*[159] found that a 2-at% solution of V in Nb metal will increase the modulus of Nb by ~2%. The influence of Ni solutes is unknown, but may account for the additional increase in the V modulus. As a result of the solid-solution hardening, the expected elastic residual stress, $E\Delta\alpha\Delta T$, in the V interlayer increases compared to Ni/V/Ni interlayers, from 560 MPa to 705 MPa. Since the V yield strength is ~300 MPa, and V is able

to form a complete solid solution with both Ni and Nb, plastic yielding is expected to dominate the interlayer during cooling in accordance with Figure 2.4. Thus the equivalent stress, σ_0, in the interlayer is assumed to be equal to the stress needed to cause plasticity in the interlayer, which is initially taken to be the V uniaxial yield stress. Both He[28] and Cao[27] predict that when plastic yielding dominates the interlayer, the equivalent stress in the ceramic near the interface, but away from the bond's edge, is $-(0.1\text{-}0.2) \times \sigma_0$. V has a uniaxial yield stress of ~300 MPa, and is able to strain harden substantially; its ultimate tensile strength is ~450 MPa [138]. As a result, the stress in the Al_2O_3 is expected to be in the range of 30–90 MPa, depending on the amount of strain-hardening that has occurred in the V due to prior deformation.

To determine the accuracy of this model, photoluminescence (PL) spectroscopy was used to directly measure the residual stresses in the Al_2O_3 near the interface. The results of the scan can be seen in Figure 4.34. The residual stress was found to be ~40–70 MPa nearest to the ceramic/metal interface, which falls in the center of the predicted range. Thus, the assumption that the V interlayer undergoes plastic relaxation due to the elastic residual stresses during the bonding process appears to be valid.

While the residual stresses in the Ni/Nb/V/Nb/Ni bonds were similar to those in Ni/V/Ni bonds, the fracture strengths were not. The fracture strengths of the resultant bonds are shown in Figure 4.35. Despite the presence of the Nb, using a 2-μm Ni/2-μm Nb/V/2-μm Nb/2-μm Ni interlayer resulted in fracture strengths of 137±17 MPa, well below the 245±54 MPa fracture strength of the bonds fabricated with a 2-μm Ni/V/2-μm Ni interlayer.

Since the fracture strength of Ni/Nb/V/Nb/Ni bonds were lower than those of Ni/V/Ni bonds despite having similar residual stresses, the interfacial microstructure is expected to contribute significantly to the differences in fracture strengths. For the Ni/Nb/V/Nb/Ni bonds, $CTE_{metal} > CTE_{ceramic}$. From the analysis of Cao *et al.*[27], a positive CTE mismatch indicates that interfacial failures are not energetically favorable unless the interfacial strength is significantly lower than that of the ceramic or metal bulk. In Figure 4.36, the opposing metal and ceramic fracture surfaces are shown. The lack of any bright, metallic phases on the ceramic fracture surface suggests that fracture occurred along the metal/ceramic interface. In Figure 4.37, a higher magnification reveals that the interface was not smooth, a discrete secondary phase is present on the metal surface, and is nearly continuous along the grain boundaries. Figure 4.38 shows the ceramic fracture surface. The surface is rough, and is the negative surface structure of that seen in Figure 4.37. Figure 4.39 is the same image as Figure 4.38, but with a channel of porosity outlined. This outline is the negative of a grain boundary seen on the metal fracture surface. The fracture surfaces indicate that a substantial amount of Al_2O_3 dissolution occurs at the interface during bonding. Ni-Nb and Co-Nb liquids are expected to have similar properties. Valenza *et al.*[160] have recently shown that additions of Nb to pure Co promote Al_2O_3 dissolution. The observations are thus consistent with similar behavior occurring in the Ni-Nb and Ni-Nb-V systems.

Figure 4.40 shows a cross section of the bonded assembly. While no interfacial phase is present, there are large regions of interfacial porosity. The largest of these are two 35-μm long voids separated by a 5-μm-thick ligament of metal. Using the first-order approximation that the voids constitute a crack with a radius of 20 μm, and the assumption, as a lower bound,

that the interface has a toughness similar to Al_2O_3, ~2 MPa√m, then interfacial failure would be expected at a stress of ~225 MPa – higher than the actual measured fracture strengths. However, this approximation assumes that void is isolated and the sole void along the interface. In reality, there are multiple voids present, and the cross-sections of the voids seen at the surface in Figure 4.40 are most likely not representative of the largest diameter of the voids, underestimating their true size. The presence of the voids reduces the true load-bearing area at the interface. On the right interface in Figure 4.40, only ~50% of the interface is bonded, which means that the true stress experienced at the interface during loading will be ≥2× the applied stress. Thus for a flaw with a radius of 20 μm, the applied stress needed for failure would be closer to 225 MPa/2≈113 MPa, which is close to measured fracture strength of the bonded assembly.

During the bonding process, the presence of Nb at the interface does not diminish the ability of Ni to diffuse rapidly into the interlayer. Since the 2-μm Nb layer separates the Ni cladding from the V, initially the Ni would react exclusively with Nb, forming Ni_3Nb and Ni_6Nb_7 intermetallic phases during heating. Extrapolating from the data of Sprengel *et al.*[161], the interdiffusion coefficients of Ni in Ni_3Nb and Ni_6Nb_7 intermetallics are the same order of magnitude of that of Ni diffusivity in Nb and V matrices at 1400°C. The intrinsic diffusivity of Ni in the intermetallic phases was not available in the literature for comparison. Assuming the Ni and Nb diffusivities are equivalent in the intermetallic phases, Ni diffuses more quickly in the intermetallic than in the pure metals at temperatures closer to 1000°C. As a result, similar to the situation in Ni/V/Ni bonds, over 90% of the Ni will have dissolved into the V foil and be in solid solution prior to reaching the liquidus temperature. There would not be sufficient Ni-Nb-V liquid phase remaining to flow into and fill all interfacial voids and gaps. The exact composition of the interfacial and grain boundary metallic phases is unclear; EDS was unavailable at the time this bond was fabricated. Unfortunately, there are currently no ternary Ni-Nb-V phase diagrams at the bonding temperature of 1400°C. Looking at the Ni-V-Nb liquidus and solidus projections in Figure 4.41, it appears that there are a number of solidification paths possible. To determine the solidification path, a more detailed investigation – including determining the exact compositions of the existing phases of the bonded assembly as well as more precise values for the initial quantities of the Ni, Nb, and V components – would be necessary.

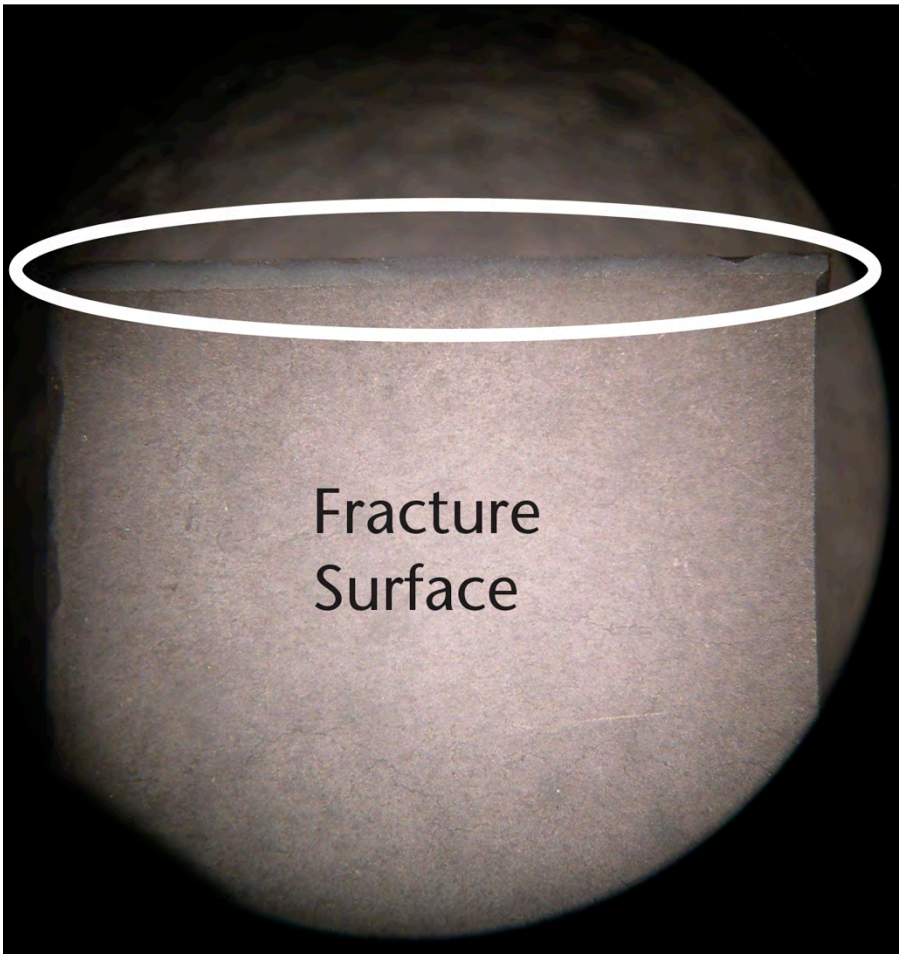

Figure 4.24: Macroscopic view of the ceramic side of the fracture surface for the interfacial failure of Al_2O_3 bonded using a Ni/Nb/Mo/Nb/Ni interlayer. The surface within the ellipse marks where the interlayer was no longer in contact with the ceramic substrate during bonding.

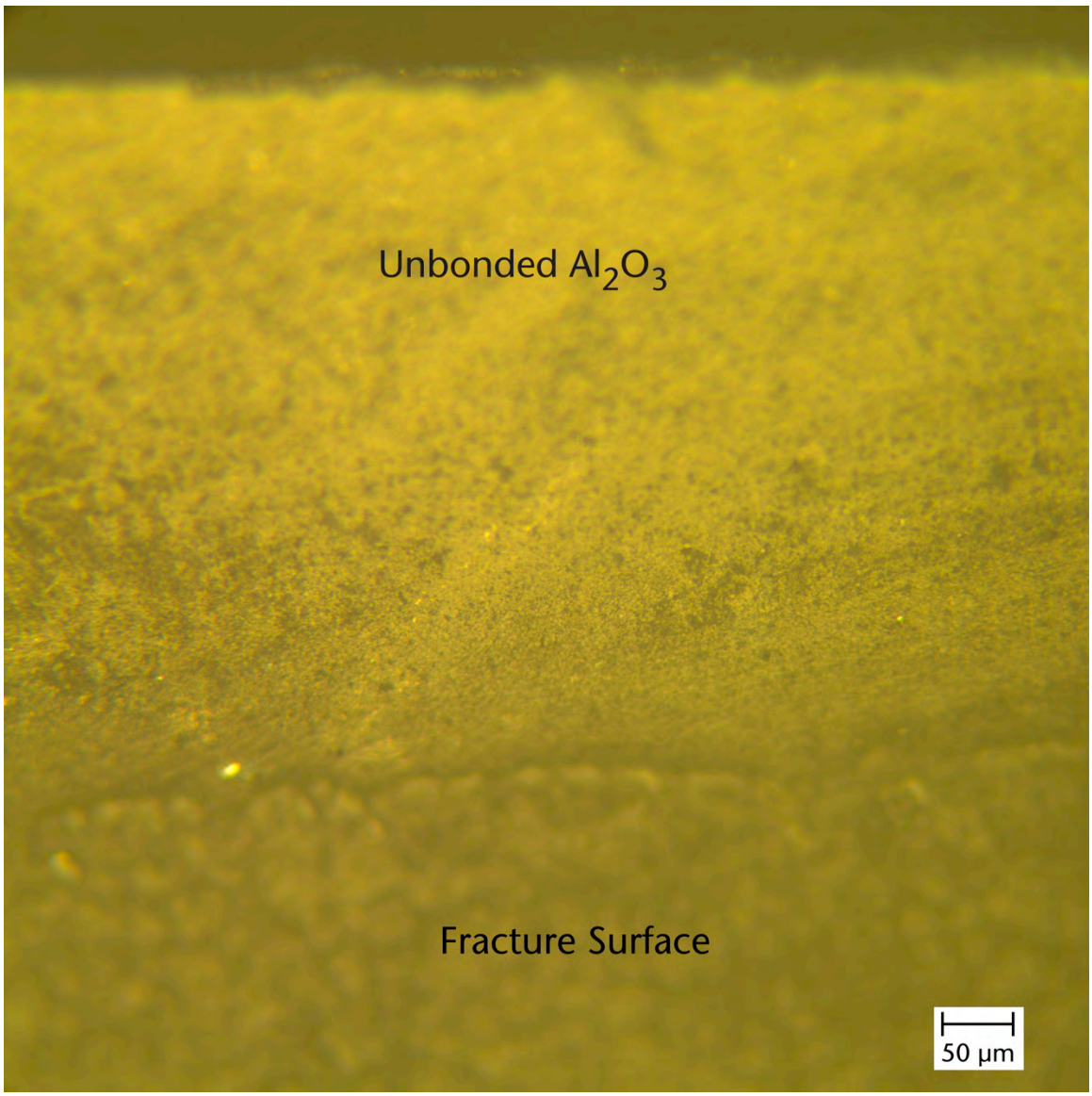

Figure 4.25: Closer view of the boundary between the Ni/Nb/Mo/Nb/Ni fracture surface, and the unbonded region of Al_2O_3 near the edge of the assembly. The fracture surface was raised above the unbonded region, as seen by the difference in focus.

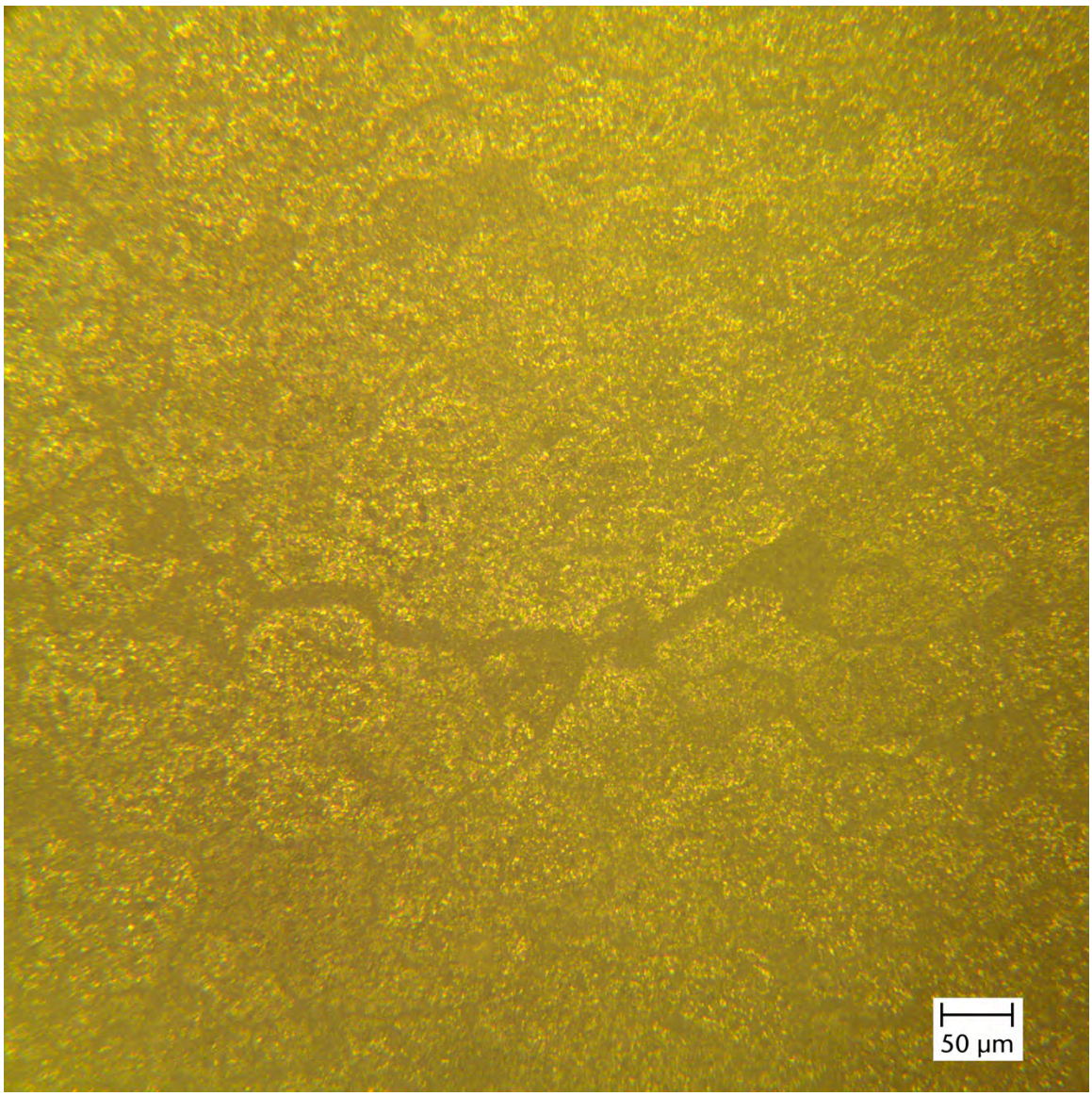

Figure 4.26: Fracture surface on ceramic side of bond. Note the channel-like void at the center of the micrograph.

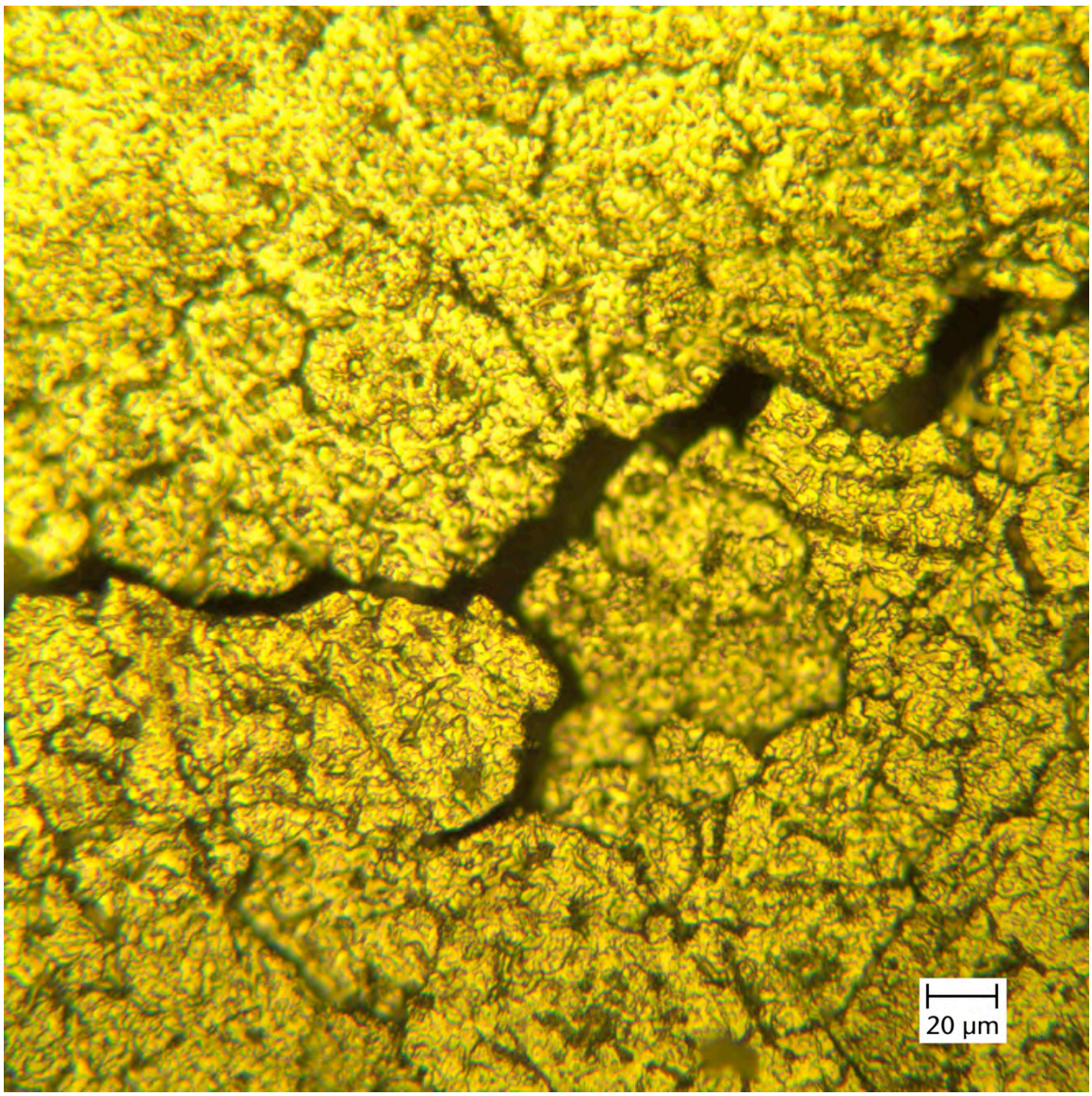

Figure 4.27: A crack-like void on the metal fracture surface of a Ni/Nb/Mo/Nb/Ni bond.

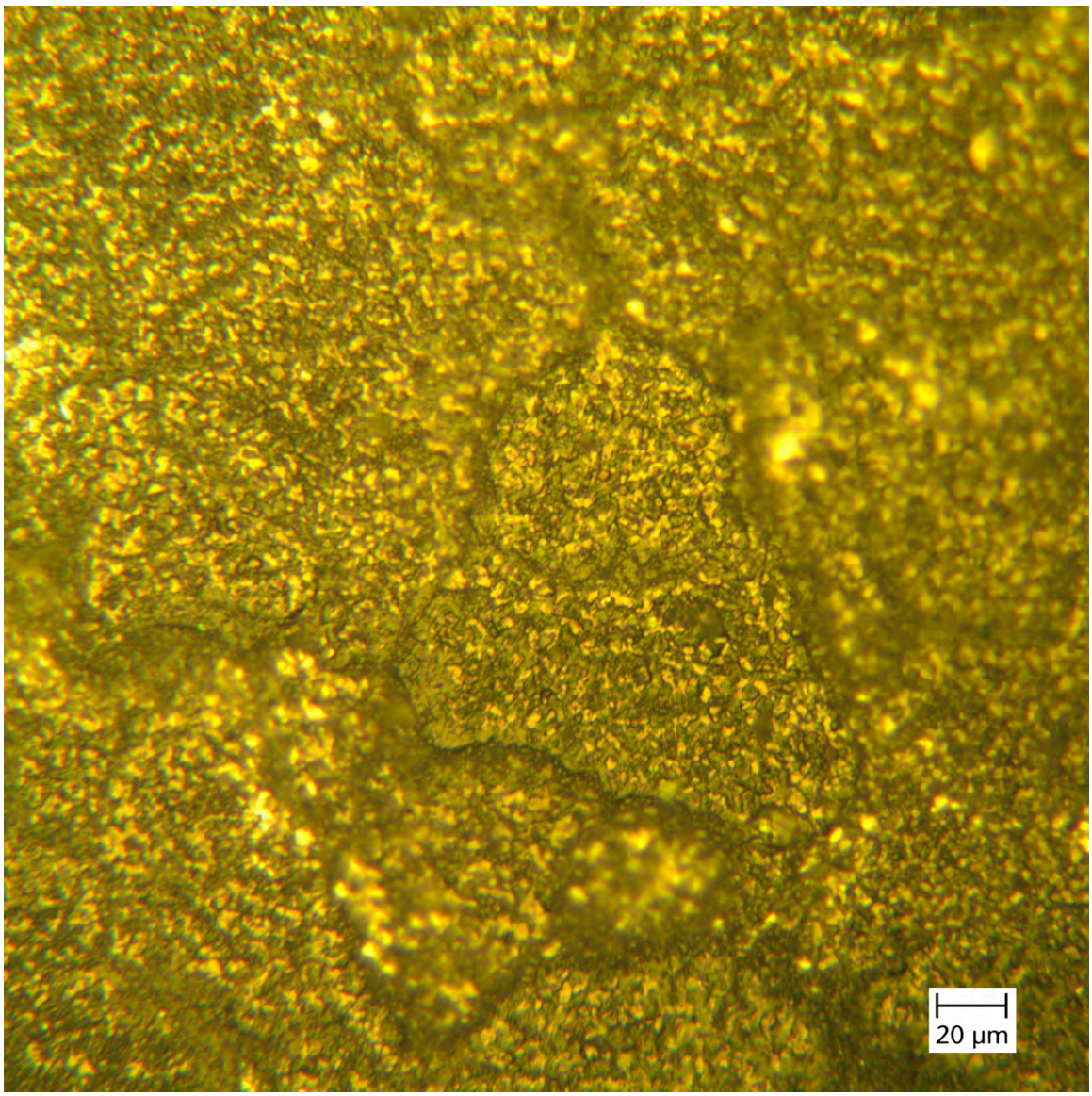

Figure 4.28: The metallic nature of the ceramic fracture surface is evident under higher magnification.

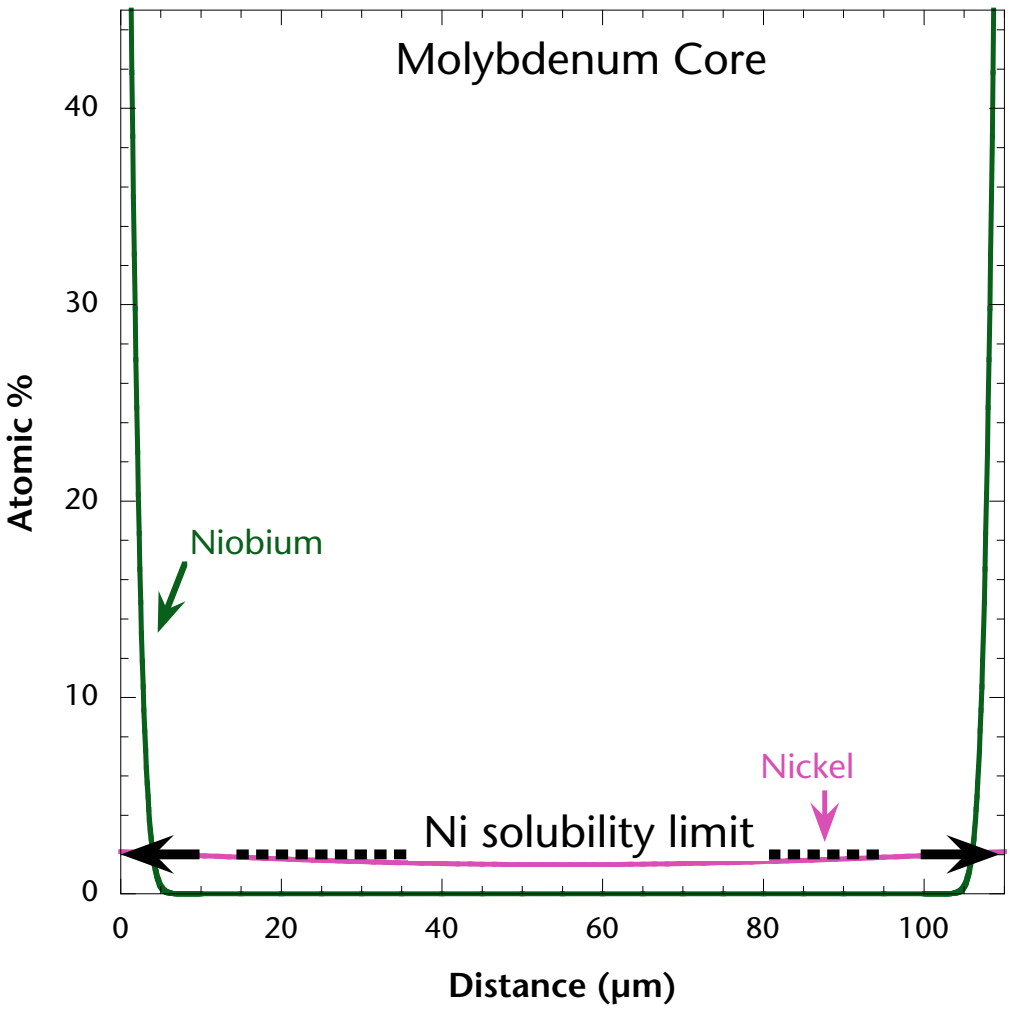

Figure 4.29: Calculated EPMA diffusion profile for a 2-μm Ni/2-μm Nb/Mo interlayer used to bond Al_2O_3 at 1400°C for 6 h under a 2.4-MPa pressure.

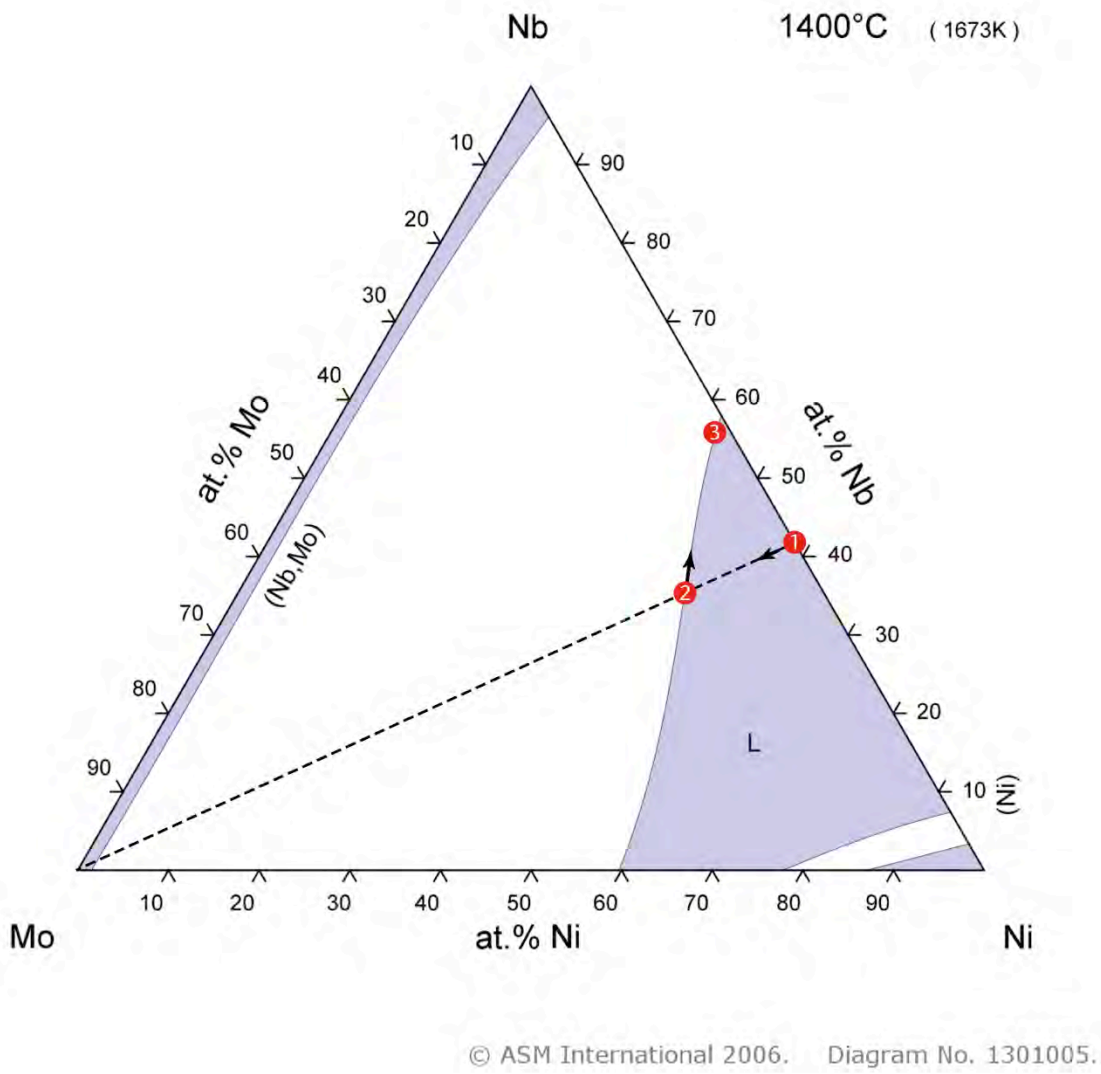

(a)

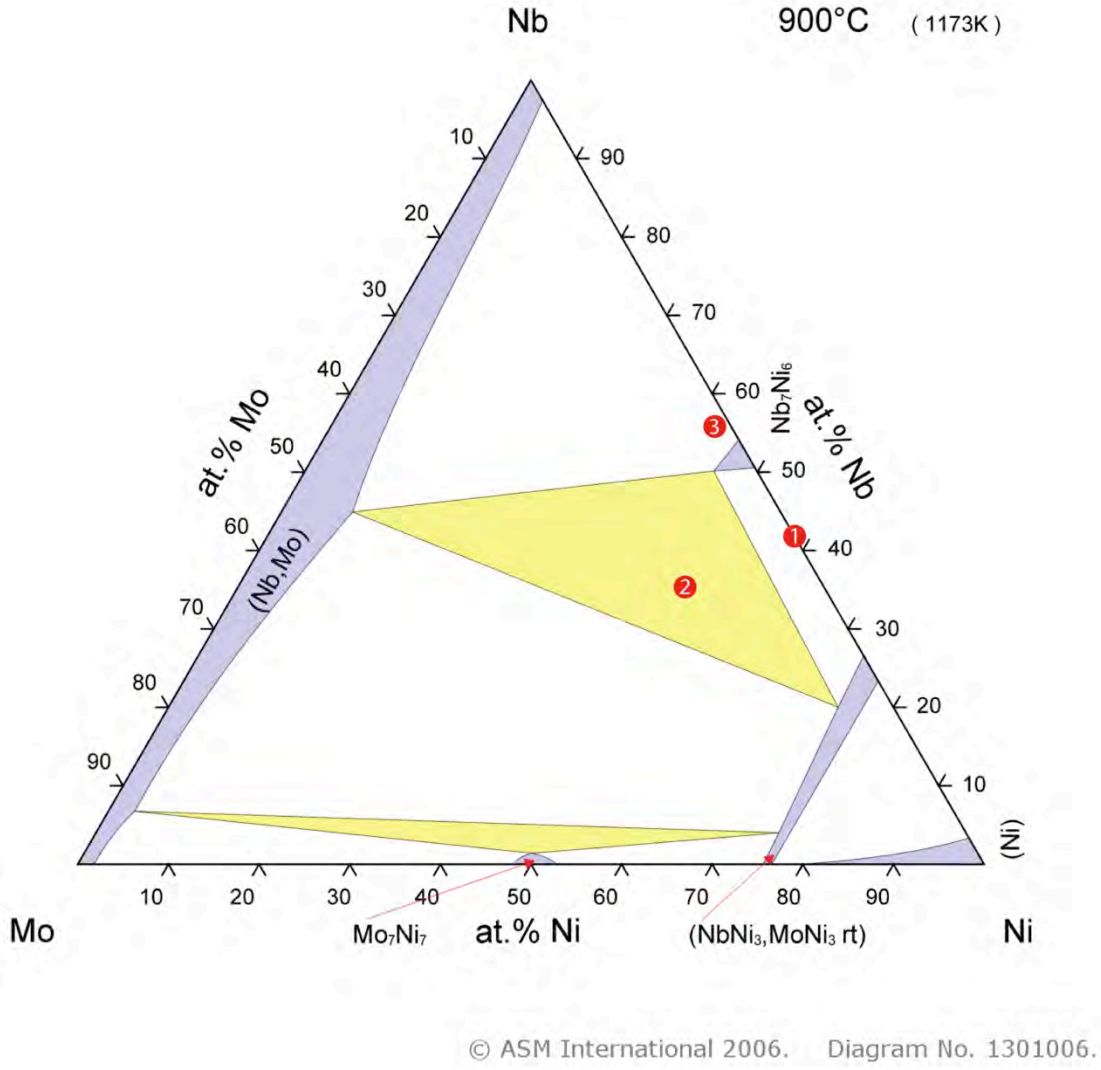

(b)

Figure 4.30: Ni-Mo-Nb ternary phase diagram at (a) 1400°C and (b) 900°C [162].

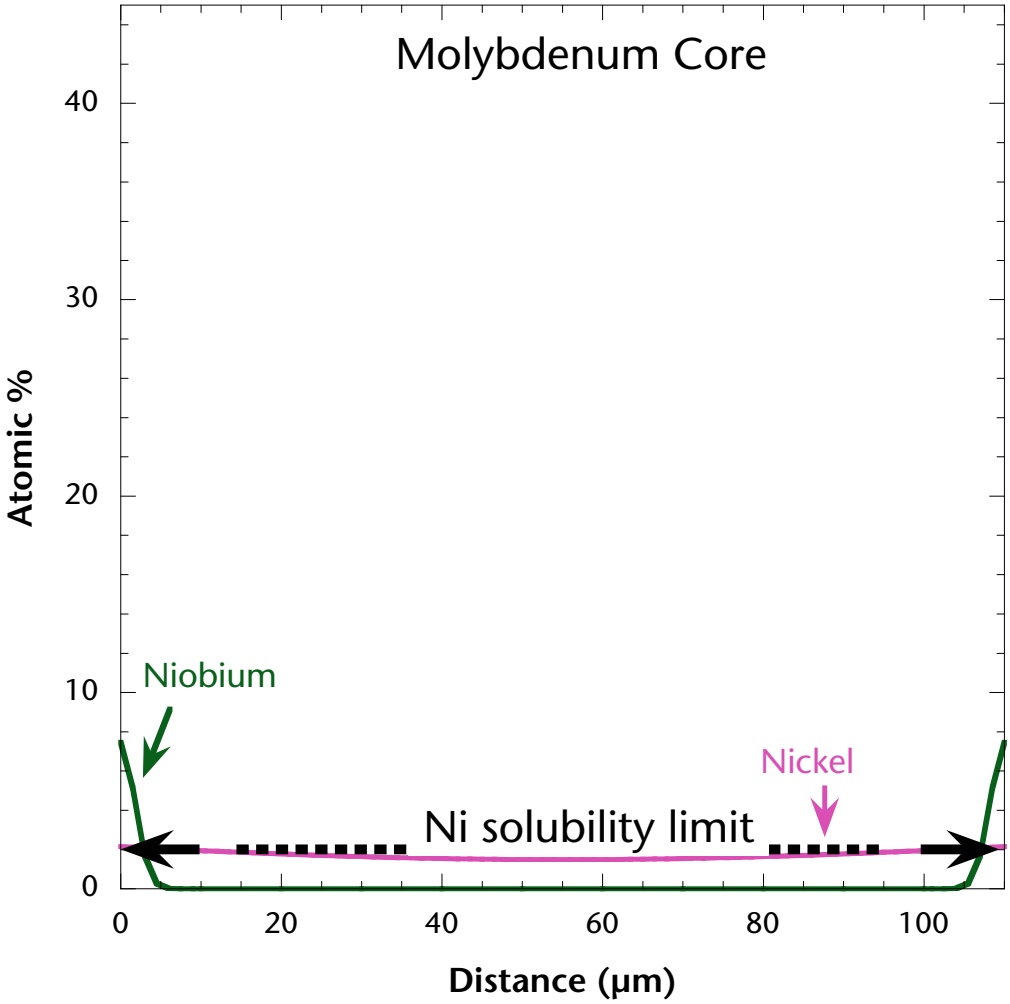

Figure 4.31: Calculated EPMA diffusion profile for a 1-μm Ni/0.15-μm Nb/Mo interlayer used to bond Al_2O_3 at 1400°C for 6 h under a 2.4-MPa pressure.

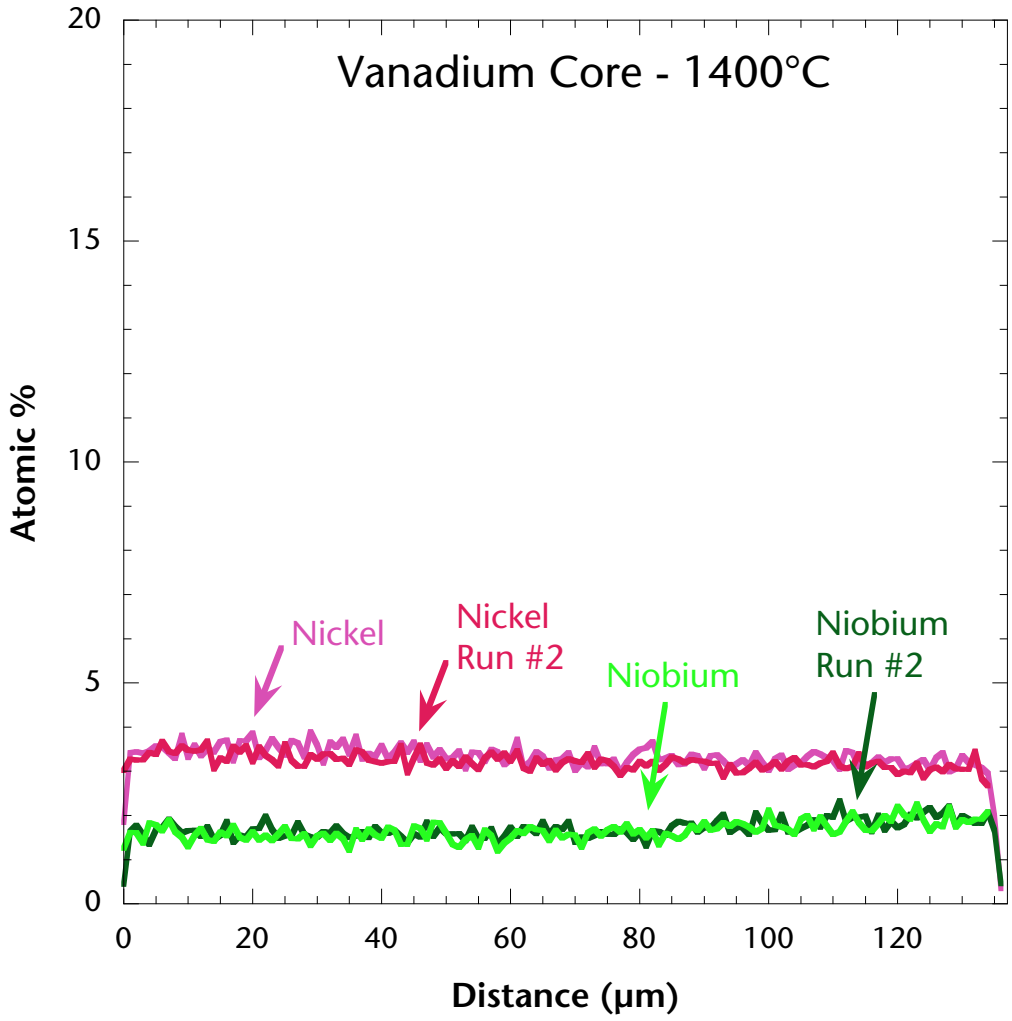

Figure 4.32: EPMA of 999W Al_2O_3 joined using 2-μm Ni and 2-μm Nb cladding with a V core layer.

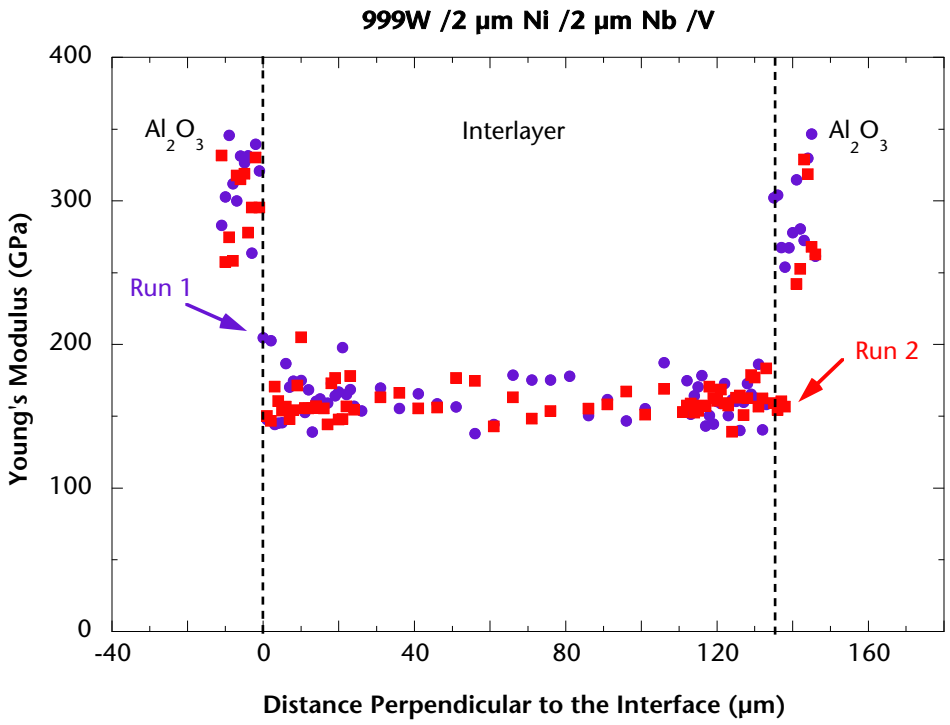

Figure 4.33: Modulus across the interlayer for Al_2O_3 bonded using a 2-µm Ni/2-µm Nb/V interlayer.

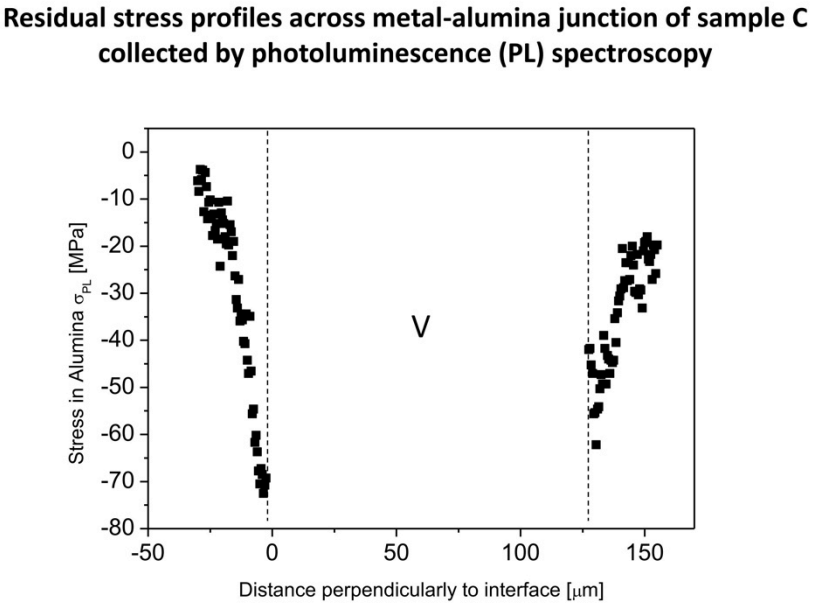

Figure 4.34: Residual stresses using 2-µm Ni/2-µm Nb/V as measured by photoluminescence spectroscopy[163].

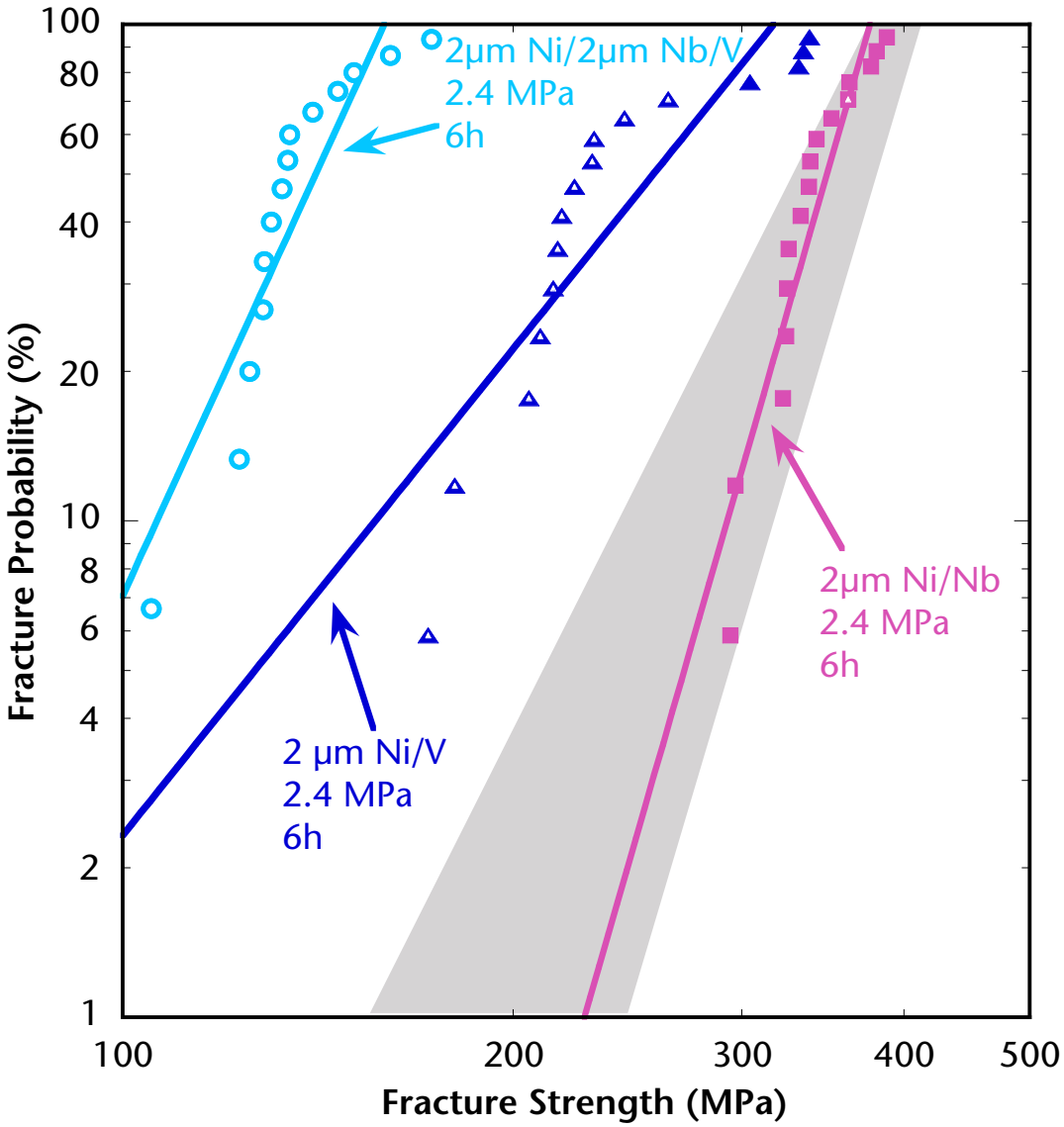

Figure 4.35: Difference in strength of 999W Al_2O_3 joined using Nb and V cores.

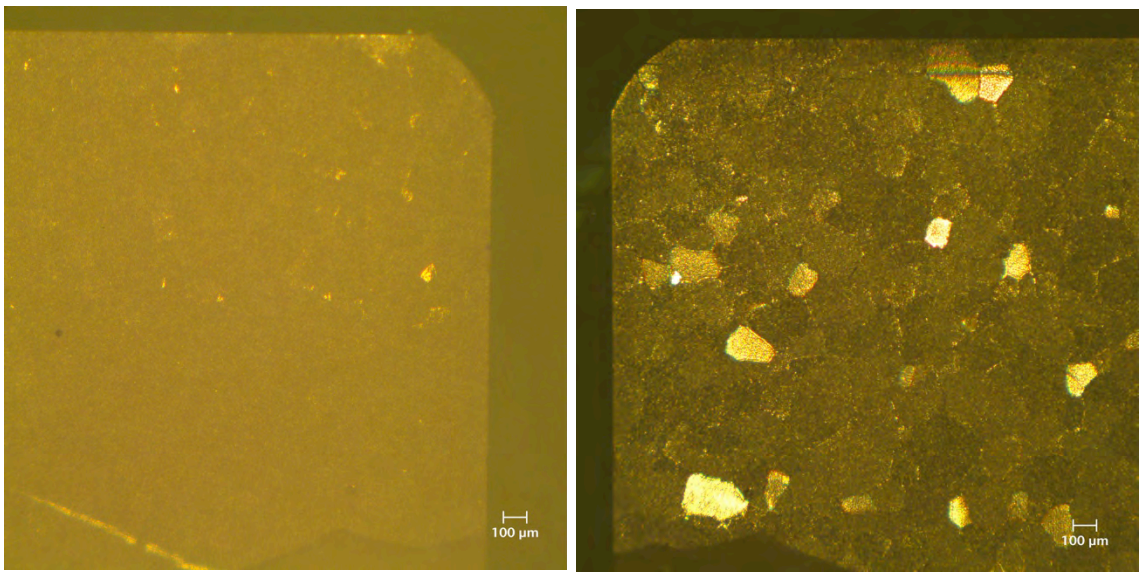

(a) (b)

Figure 4.36: Opposing faces of the (a) ceramic and (b) metal fracture surfaces for Al_2O_3 PTLP bonded using a Ni/Nb/V/Nb/Ni interlayer for 6 h at 1400°C under a 2.4-MPa pressure.

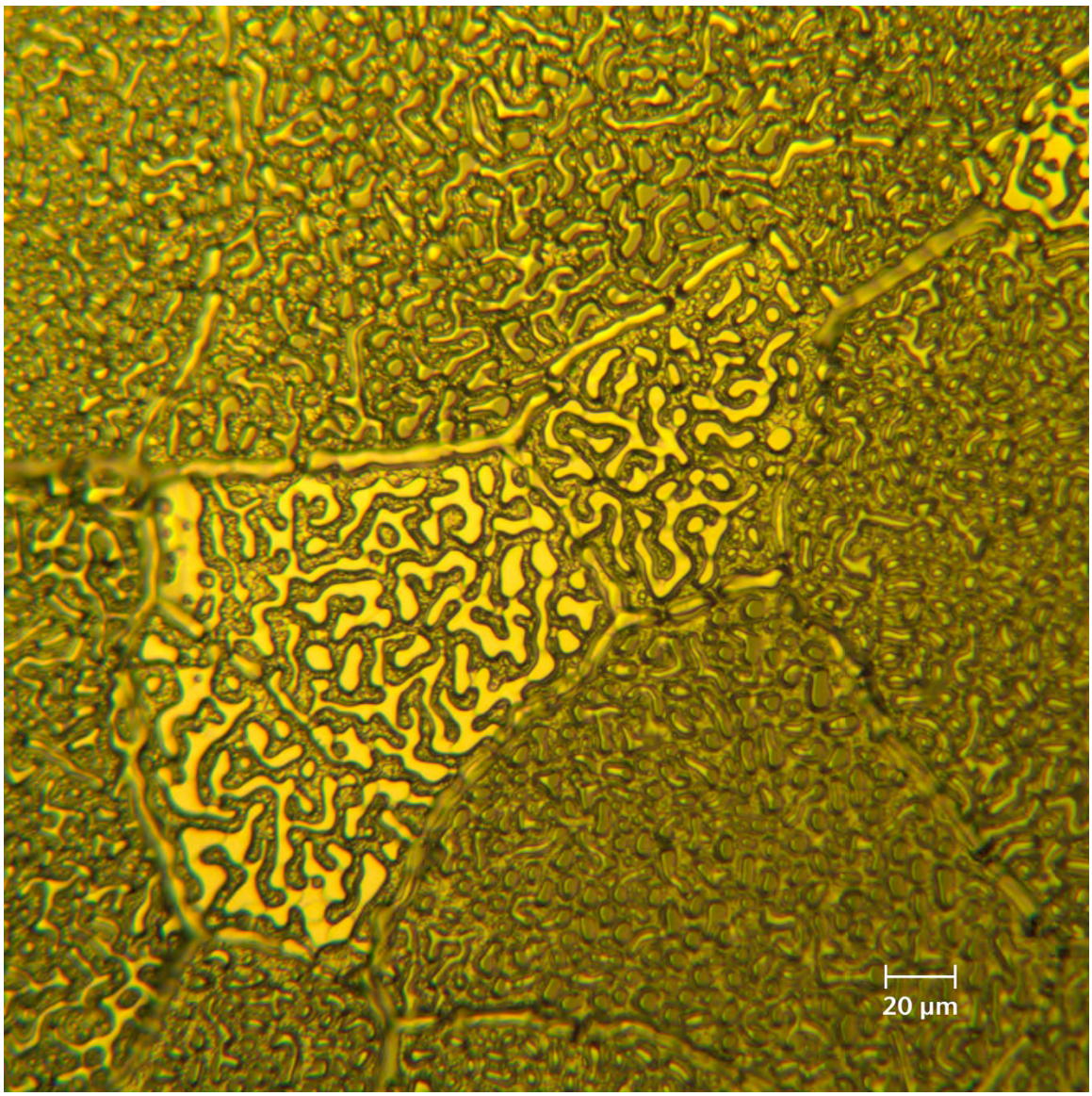

Figure 4.37: Higher magnification of the metal fracture surface of a Ni/Nb/V/Nb/Ni bond.

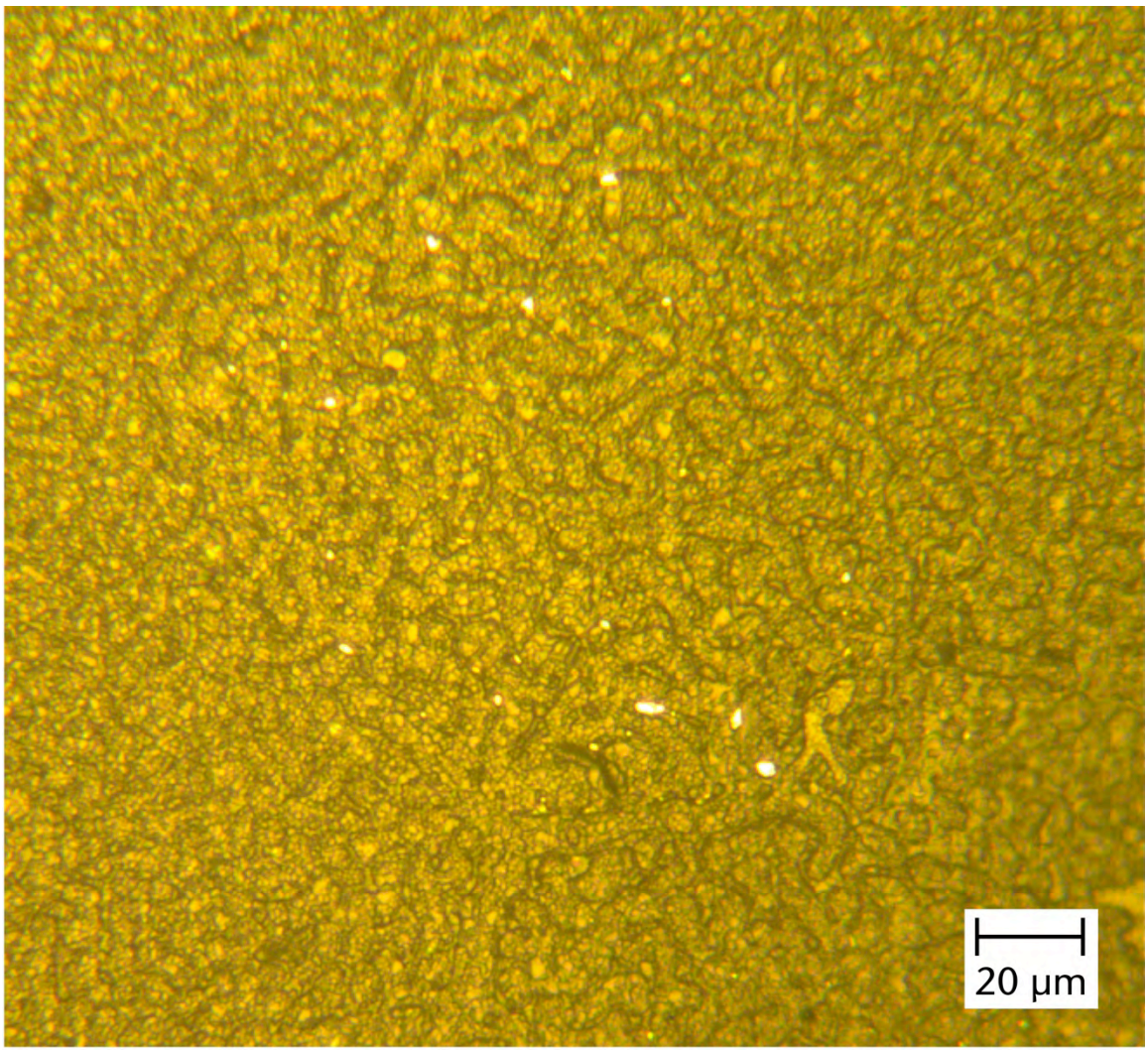

Figure 4.38: Higher magnification of the ceramic fracture surface of a Ni/Nb/V/Nb/Ni bond.

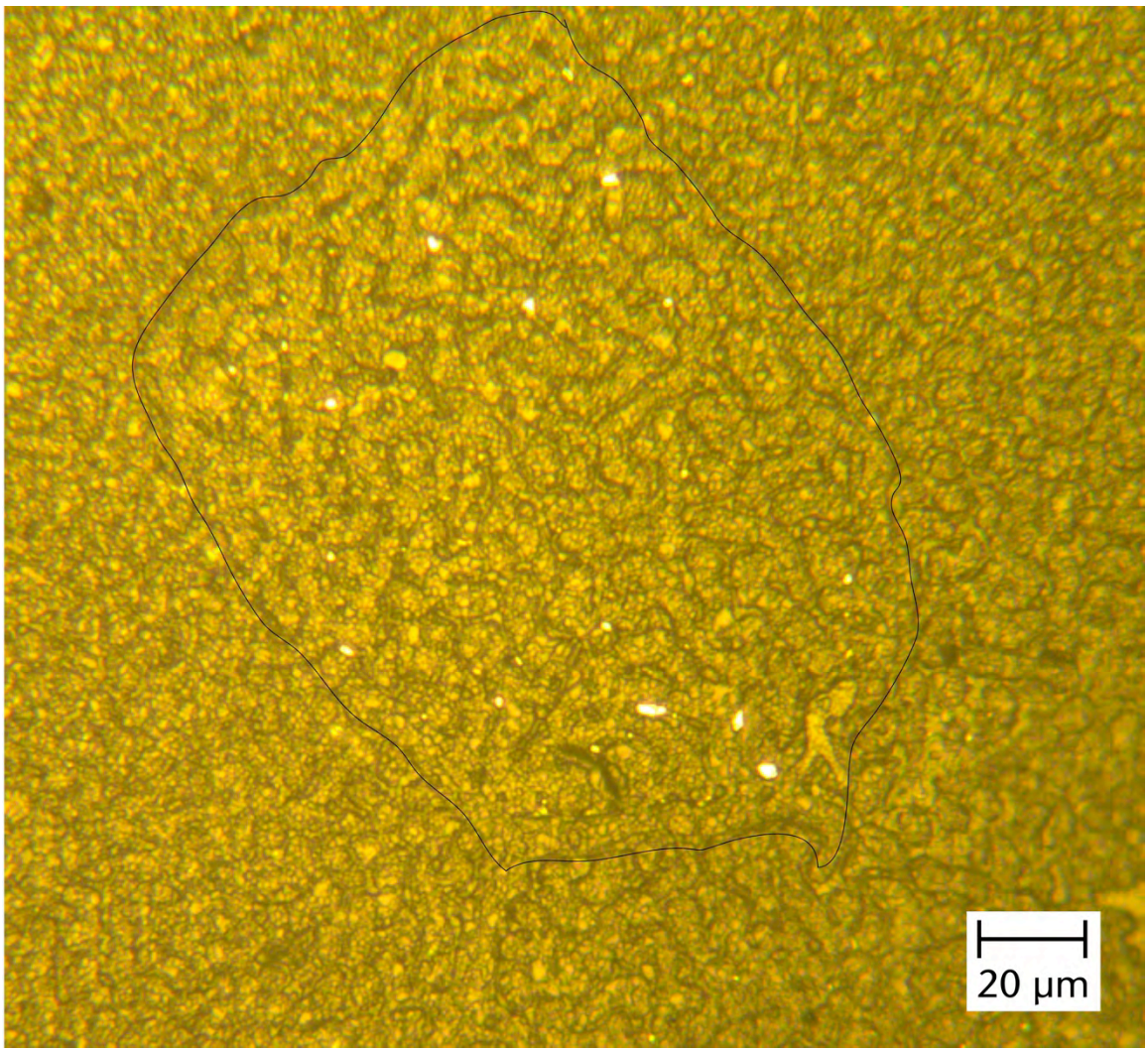

Figure 4.39: Identical micrograph as Figure 4.38, but with an approximate outline of a metallic grain boundary that has etched away a portion of the ceramic surface, leaving behind a channel of voids in its place.

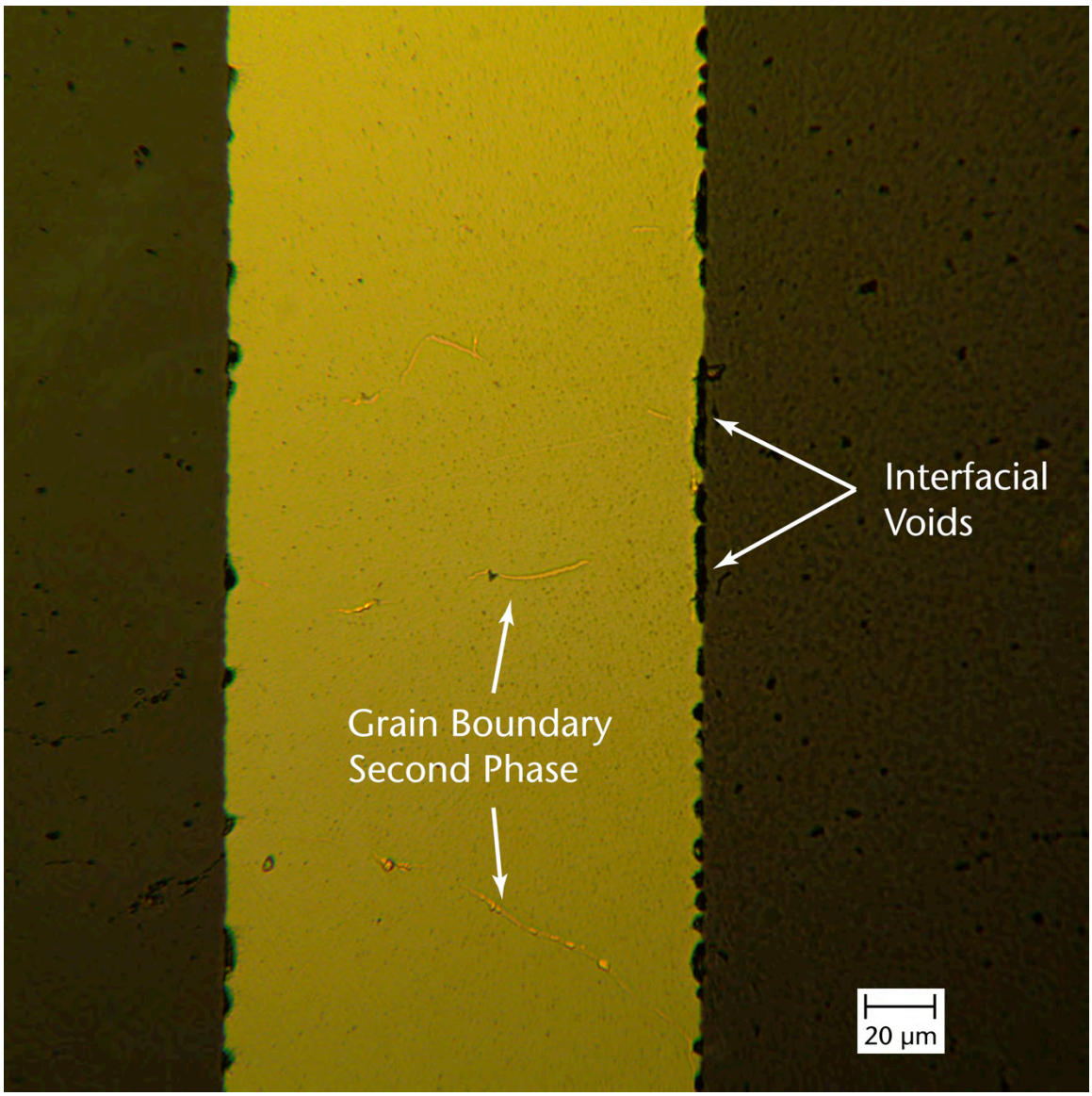

Figure 4.40: Cross-section of Ni/Nb/V/Nb/Ni bond. Significant porosity is present along the grain boundaries, as long as 35-μm. No secondary phases are visible along the interface, but secondary phases can be seen along the grain boundaries within the V core.

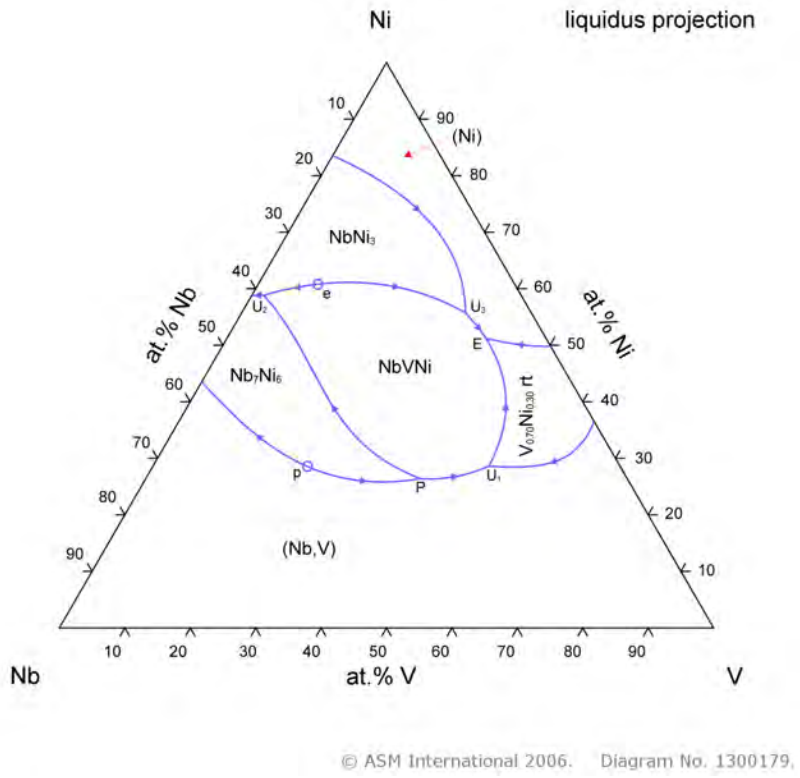

(a)

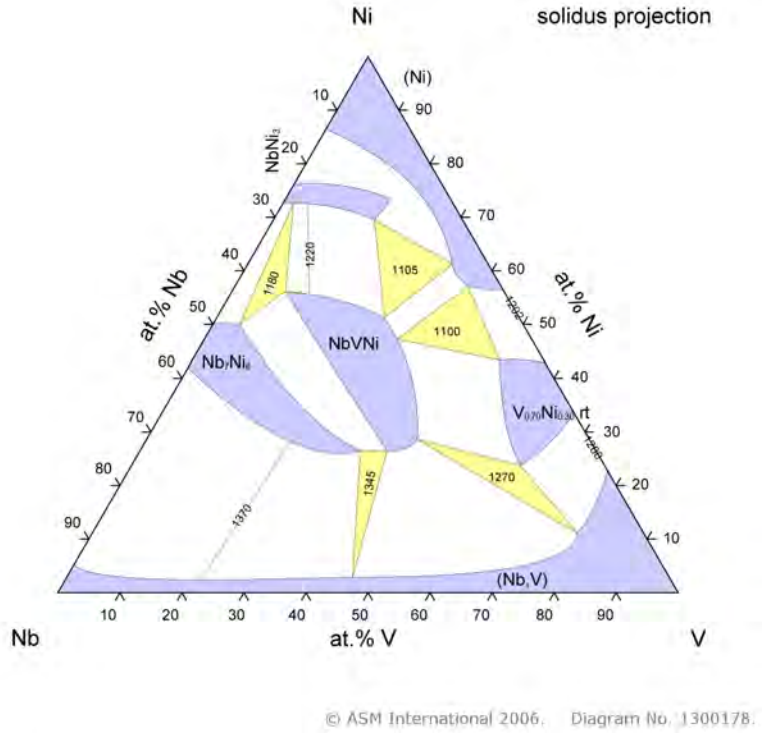

(b)

Figure 4.41: (a) Liquidus and (b) solidus projections of the ternary Nb-Ni-V phase diagram[164].

4.3.3 PTLP Bonding of Al_2O_3 using Mo-Surface-Modified Cores

4.3.3.1 Ni/Mo/Nb/Mo/Ni

A Mo surface-modified Nb core was employed in the PTLP bonding of Al_2O_3 in an attempt to prevent a Nb-based liquid phase from forming. By creating a PTLP bond that forms a Ni-Mo liquid phase at the interface, similar to a Ni/Mo/Ni interlayer, and has the CTE characteristics of a Nb foil, similar to the Ni/Nb/Ni interlayer, one would gain insight into the role of the Nb-based liquid phase during bonding. A 1-μm-thick Mo layer was initially used. Ni diffusion in Mo occurs predominantly through LFM along the grain boundaries, and the Ni lattice diffusivity in Nb is three orders of magnitude higher than the Mo lattice diffusivity in Nb [117,165]. Thus, the Ni was expected to be able to homogenize across the interlayer during bonding while the Mo remained at the interface.

Figure 4.42 shows an EPMA scan of the bonded 1-μm Ni/1-μm Mo/Nb/1-μm Mo/1-μm Ni assembly. In Mo-Nb binary systems, grain boundary diffusion does not contribute significantly to the overall flux[166]. However, while the Ni does homogenize across the interlayer as expected, it is evident that a substantial amount of Mo diffusion occurs as well. Figure 4.43 shows a cross section of the bonded interlayer. There is a notable amount of secondary-phase formation along the grain boundaries. The rapid penetration of Mo into the Nb core and the presence of grain-boundary secondary phases is an indication that the presence of Ni aids the rapid diffusion of Mo along the grain boundaries. In Ni-Nb binary systems, Ni diffuses in a solid-state manner, and diffuses anomalously fast along the Nb grain boundaries[45]. In Ni-Mo systems, LFM occurs for higher-energy grain boundaries, also causing rapid redistribution of Ni and grain growth. It is unclear whether solid-state grain-boundary diffusion or LFM causes the redistribution of Ni along the grain boundaries in this case, and could be a topic for future investigations.

Since the Mo redistributes significantly, the maximum concentration of Mo is ~10 at%, near the interface. The CTE of Nb-Mo alloys has a linear relationship with composition[167], and thus the elastic residual stress due to cooling can be estimated. Nano-indentation across the interlayer, shown in Figure 4.44, revealed that interlayer modulus is predominantly constant, ~130 GPa. The scatter in run two is attributed to the grain boundary phases across the interlayer. As an upper bound a homogeneous composition of 10-at% Mo is assumed, and the residual stress in the interlayer, $E\Delta\alpha\Delta T$, is 56 MPa, well below the uniaxial yield stress of Nb. Thus, it is reasonable to assume that the interlayer is behaving elastically. According to Cao *et al.*[27], the expected principal interfacial stress in the Al_2O_3 would be $0.2\times E\Delta\alpha\Delta T$, which is ~10 MPa. However, PL spectroscopy measurements indicated that the near-interfacial stresses in the Al_2O_3 approached 60 MPa, as shown in Figure 4.45. The discrepancy between the predicted and measured near-interfacial stress is most likely due to the inhomogeneous nature of the interlayer. For a more accurate model of the interfacial stress, a more detailed finite-element analysis would needed that accounts for the variable composition of the interlayer, which is beyond the scope of the current work.

Despite the presence of Mo and the intermetallic phases along the grain boundaries, the fracture strengths of the 1-μm Ni/1-μm Mo/Nb/1-μm Mo/1-μm Ni assembly were nearly as high as those of Ni/Nb/Ni assemblies, as seen in Figure 4.46. All but one of the 1-μm Ni/1-μm Mo/Nb/1-μm Mo/1-μm Ni bonds failed in the bulk ceramic. For the 1-μm Ni/1-μm Mo/Nb/1-μm Mo/1-μm Ni assemblies, the average fracture strength was

292±54 MPa, compared to 341±28 MPa for the 6 h Ni/Nb/Ni bonds[119,137]. While similar, the average fracture strength of the 1-μm Ni/1-μm Mo/Nb/1-μm Mo/1-μm Ni bonds was more than a standard deviation below the average fracture strength of Ni/Nb/Ni. Since the addition of Mo decreases the CTE of the Mo-Nb alloy, and since $CTE_{Metal}<CTE_{Ceramic}$, a tensile layer exists along the edge of the ceramic, decreasing the resistance of the ceramic to edge flaws[27]. It was thought that this might have played a role as well. To determine if a thicker Mo coating would further decrease the strength, a second set of bonds was fabricated using 1-μm Ni/3-μm Mo/Nb/3-μm Mo/1-μm Ni interlayers. The fracture results are shown in Figure 4.47. Despite the increase in Mo, the fracture strength of the assemblies increased, to 320±40 MPa, within the strength range of monolithic Al_2O_3 beams. This suggests that the strength decrease of the 1-μm Ni/1-μm Mo/Nb/1-μm Mo/1-μm Ni bonds may be predominantly due to scatter in the strength of the Al_2O_3 itself. This is not unprecedented, as differences in average fracture strength of up to ~140 MPa (481±19 MPa [137] vs. 339±40 MPa, Figure 4.11) have been observed in identically processed sets of Al_2O_3 bonded for 30 min with Ni/Nb/Ni interlayers, where nearly all of the samples failed in the ceramic phase.

4.3.3.2 Ni/Mo/V/Mo/Ni

Compared to Nb, Mo and V have properties that lie on opposite ends of the spectrum. Mo has a lower CTE, lower Ni solubility, and slower Ni lattice diffusion than Nb. V, in contrast, has a higher CTE, higher Ni solubility, and faster Ni lattice diffusion than Nb. In both cases, these differences in properties from Nb had drawbacks that led to binary Ni/Mo/Ni and Ni/V/Mo systems failing interfacially when used to PTLP bond Al_2O_3. For Mo, the low CTE and non-ductile nature led to elastic stresses forming that caused the interfacial failures, while for Ni/V/Ni systems, the rapid Ni diffusion substantially reduced the amount of liquid phase formed at the interface, and the quantity that did form was insufficient to fill the interfacial voids that were present. In order to mitigate the individual weaknesses of the V and Mo interlayers, a Mo-surface modified V core was used to bond Al_2O_3. By using a 1-μm Ni/3-μm Mo/V/3-μm Mo/1-μm Ni interlayer, it was expected that the Mo would help to slow the incorporation of Ni into the V core, thereby increasing the quantity of liquid that forms at the interface and decreasing the area fraction of interfacial flaws that remain after bonding.

The Ni solubility in pure Mo is ~2 at% and Ni has a lattice diffusivity of $\sim 10^{-12}$ cm^2/s in Mo at 1400°C. This solubility-diffusivity product is much lower than that of Ni in V, where the Ni solubility ranges from 15–29 at% as the temperature increases from 800°C to 1400°C, and the lattice diffusivity increases from $\sim 10^{-14}$ cm^2/s to $\sim 10^{-9}$ cm^2/s in the same temperature range. As a result, during heating from room temperature to 1400°C, the Mo layer will act as a boundary to Ni diffusion, reducing the quantity of Ni incorporated into the V core relative to the Ni/V/Ni interlayers. Mo and V form complete solid solutions and thus Mo is expected to incorporate into the V core. Pelleg *et al.*[168] found that the diffusivity of Mo in V is relatively low, $\sim 5\times 10^{-11}$ cm^2/s at 1400°C. The diffusivity of V in Mo was not found to have been measured, but for Nb-V systems the interdiffusion coefficient increased two orders of magnitude as the concentration of V increased from 0–100% V [165], suggesting that V diffusion in Mo is higher than Mo diffusion in V. As a result, it is estimated that by the time the joining temperature of 1400° has been reached, the Mo has incorporated into the V core.

Prior to this, a Mo-rich layer is expected to be present which separates the Ni-rich layer from the V core, lowering the rate of Ni redistribution into the core.

Neglected in this analysis is the presence of the NiMo intermetallic phase that is expected to form during heating, as seen in the phase diagram in Figure 4.10a. Based on the studies of Ni diffusion in Ni_6Nb_7, which found that the Ni interdiffusion coefficient in Ni_6Nb_7 and Ni_3Nb was the same order of magnitude as Ni lattice diffusion in Nb [161], the diffusion rate of Ni in NiMo is assumed to be similar to that of Ni lattice diffusion in Mo. As such, accounting for diffusion through the NiMo intermetallic would not significantly change the quantity of the liquid phase expected to form at the interface. Thus, diffusion through the NiMo phase was not included.

Due to the high diffusion rates of Ni and Mo in V, both the Ni and Mo were calculated to homogenize in the V interlayer during bonding. As a result, the homogenized V interlayer contains 4.1-at% Mo and 2-at% Ni. Pridantseva *et al.*[167] found a non-linear relationship between Mo-V composition and CTE, where between 0–10-at% Mo the CTE was equivalent to that of pure V. As a result, the residual stress state in the 1-μm Ni/3-μm Mo/V/3-μm Mo/1-μm Ni bonds is considered equivalent to that of the Ni/V/Ni bonds described in Section 4.3.1.3, and the interlayer deforms plastically during cooling.

The fracture strengths of the 1-μm Ni/3-μm Mo/V/3-μm Mo/1-μm Ni bonds are shown in Figure 4.48. They had an average fracture strength of 302±29 MPa and all of the beams failed in the ceramic phase. While still less than the Ni/Nb/Ni bond strength of 341±28 MPa, it is a significant improvement compared to the Ni/V/Ni bonds, which failed exclusively at the interface and had a fracture strength of 245±54 MPa. Since all of the failures occurred in the Al_2O_3 bulk, it suggests that the interface is no longer the strength-limiting component when PTLP bonding Al_2O_3 using a 1-μm Ni/3-μm Mo/V/3-μm Mo/1-μm Ni interlayer.

Figure 4.49 shows a cross-section of the 1-μm Ni/3-μm Mo/V/3-μm Mo/1-μm Ni interlayer after bonding. No secondary phases are present along the interface or within the interlayer. Unlike the interfaces for Ni/V/Ni, such as in Figure 4.20, the interfacial imperfections are filled. This has two important implications: the addition of the Mo layer increased the amount of liquid at the interface sufficiently so that liquid was able to flow into and fill gaps, and the liquid was able to fill most interfacial voids despite having a relatively high contact angle on Al_2O_3 compared to the Ni-Nb liquid phase. Not all interfacial voids were filled, as seen in Figure 4.50, likely due to an insufficient amount of liquid phase. As discussed in Section 2.1.1, a liquid with contact angle >90° is expected to be able to penetrate certain geometries of flaws. In addition, the bonding pressure increases the driving force for the liquid to penetrate flaws it otherwise would not[169]. As a result, to produce high-bond strength it appears that when an external pressure is applied during bonding, the contact angle of the liquid phase is less important than the quantity of the liquid phase and the ability for all the interlayer components to form a complete solid solution.

Despite all of the 1-μm Ni/3-μm Mo/V/3-μm Mo/1-μm Ni bonds failing in the ceramic, the fracture strengths were a standard deviation below those of the Ni/Nb/Ni bonds. This is expected to be due to both natural scatter in the ceramic fracture strength, and the difference in residual stress fields in the two bonds. While the elastic residual stress due to

cooling, $E\Delta\alpha\Delta T$, was only 13 MPa in the Ni/Nb/Ni interlayer, for the 1-μm Ni/3-μm Mo/V/3-μm Mo/1-μm Ni bonds, $E\Delta\alpha\Delta T$ is 613 MPa, double the yield stress of V and indicating that significant plastic deformation occurs in the V foil. Figure 4.51 shows a schematic of the bonded interlayer. As discussed in Section 2.1.2 and 2.1.3, He[28] and Cao[27] have noted that when $CTE_{metal} > CTE_{ceramic}$, a region of tensile stress develops in the ceramic $y \sim 0.03 \times h$, the interlayer thickness, from the edge of the sample. Since the interlayer thickness is 125 μm, then the region of tensile stress is only $y \sim 4$ μm from the edge of the sample; closer to the edge the stress is compressive. This means that any surface flaws >4 μm in size extend into the tensile region, potentially causing ceramic fractures to occur.

The maximum magnitude of the tensile stress at $y = 4$ μm is $\sim 0.7 \times \sigma_0$, which occurs at $z \sim h/2$, or $z \sim 62$ μm from the interface, parallel to the sample edge. Further from the interface, the magnitude of the tensile stress decreases, but remains tensile in nature. At a distance $2 \times h$, the tensile stress is still $\sim 0.2 \times \sigma_0$. Thus, the tensile stress, σ_{zz}, lies between $z = 0.5–2 \times h$ is 3-9 MPa for Ni/Nb/Ni bonds, and 60–200 MPa the Ni/Mo/V/Mo/Ni bonds. Assuming a penny-shaped flaw that exists at the position of maximum tensile strength and a fracture toughness of $K_I = 2$ MPa$\sqrt{m}$ for Al_2O_3, for a measured fracture strength of 340 MPa the maximum flaw size for the Ni/Nb/Ni bond is 13 μm. However, if the measured strength is 340 MPa for a Ni/Mo/V/Mo/Ni bond, then the actual stress is 340+200 MPa due to the ceramic residual stress. This reduces the maximum acceptable flaw size to 5 μm.

The locations of the ceramic fractures suggest that the residual tensile stress played a role in the failure of the Ni/Mo/V/Mo/Ni bonds. 6 of the 16 ceramic failures occurred within 300 μm of the interface, and 4 of those samples were 4 of the 5 lowest-strength samples. For the Ni/Nb/Ni bonds, none of the ceramic failures occurred less than 3 mm from the interface. Thus, the only way to improve the strengths of the Ni/Mo/V/Mo/Ni bonds would be to find a way to lower the yield stress of the V alloy, or to tailor the composition of the V-Mo core so that the CTE closely mimicked that of a Nb foil. In both cases, the magnitude of the ceramic residual tensile region would decrease, and thus increase the critical flaw size for ceramic failure.

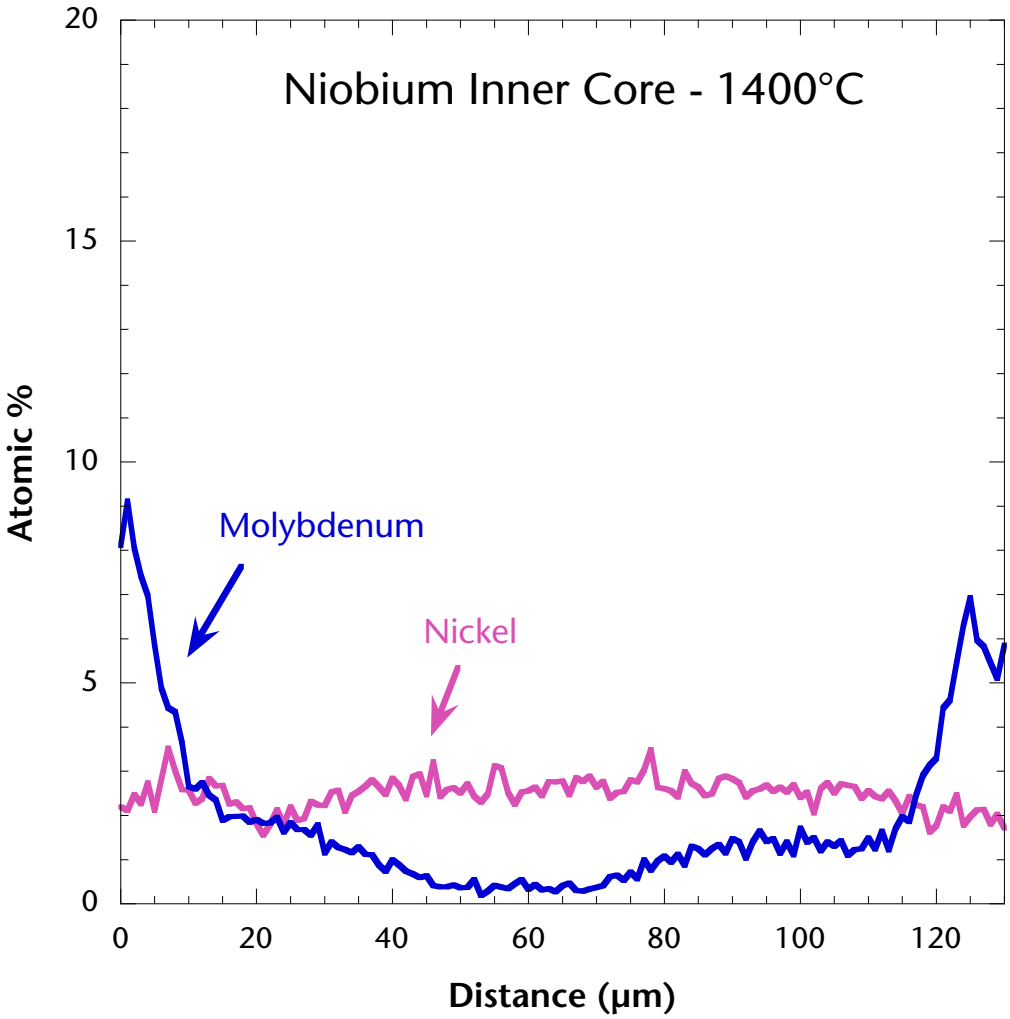

Figure 4.42: Diffusion of 1-μm Mo and 1-μm Ni claddings into Nb core after bonding for 6 h at 1400°C at 2.4 MPa

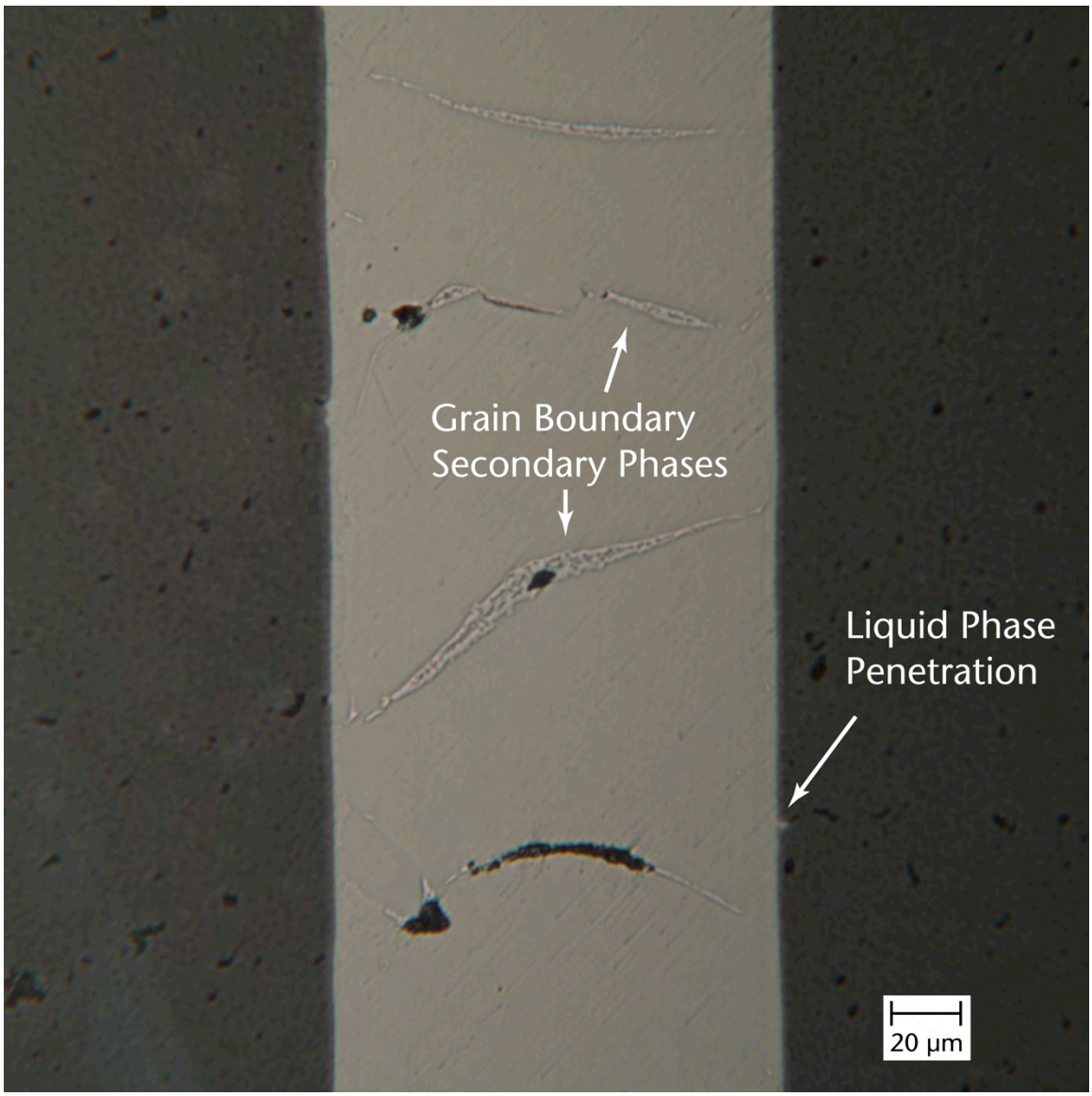

Figure 4.43: Cross section of 1-µm Ni/1-µm Mo/Nb/1-µm Mo/1-µm Ni assembly. An intermetallic secondary phase has formed along the grain boundaries. Grain boundary voids are due to secondary phase pullout during polishing. A region where the liquid phase was able to penetrate and partially fill an interfacial void is present as well.

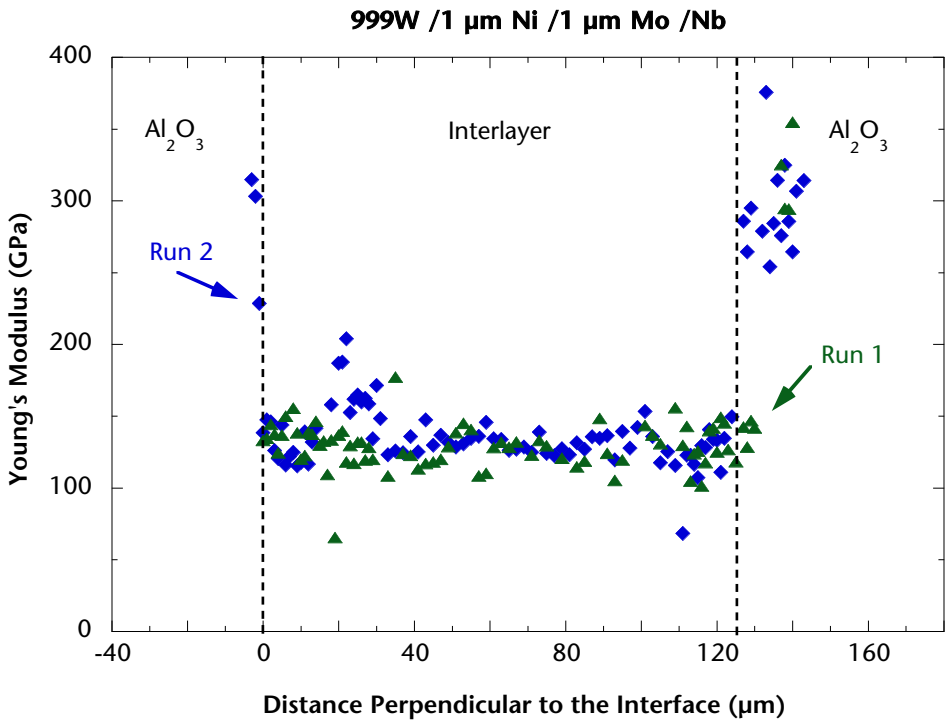

Figure 4.44: Modulus of the 1-µm Ni/1-µm Mo/Nb/1-µm Mo/1-µm Ni interlayer determined by nano-indentation[163].

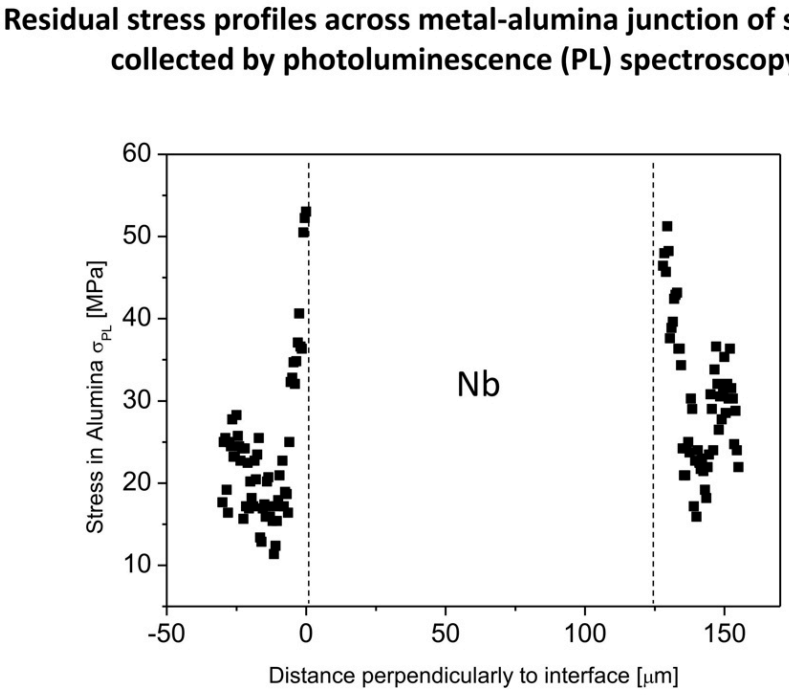

Figure 4.45: Residual stress in Al_2O_3 using 1-µm Ni/1-µm Mo/Nb/1-µm Mo/1-µm Ni interlayer as measured by photoluminescence spectroscopy[163].

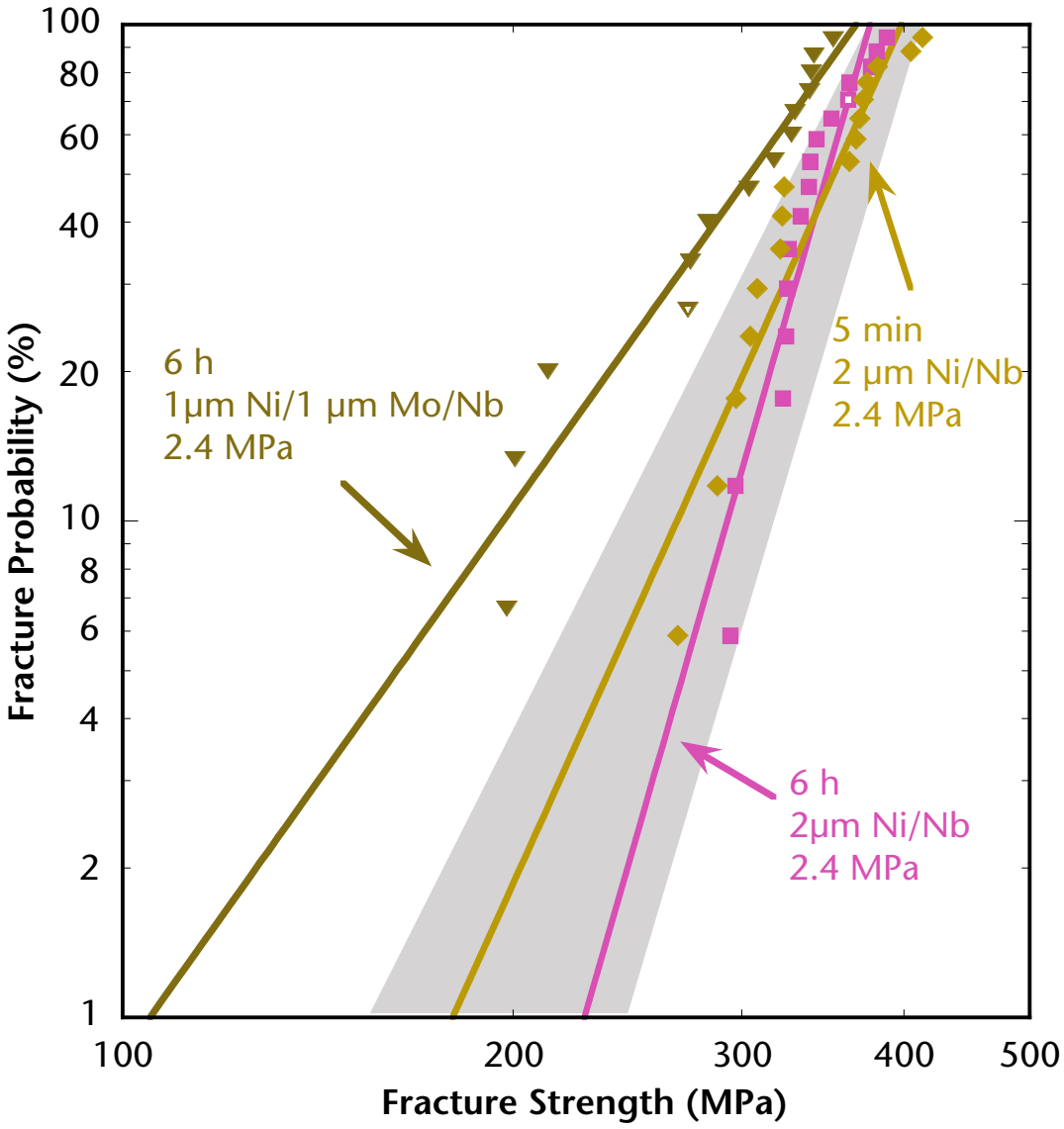

Figure 4.46: Fracture strength of 999W Al_2O_3 bonded using a Nb core and either a 2-μm Ni cladding or a combination 1-μm Ni and 1-μm Mo cladding.

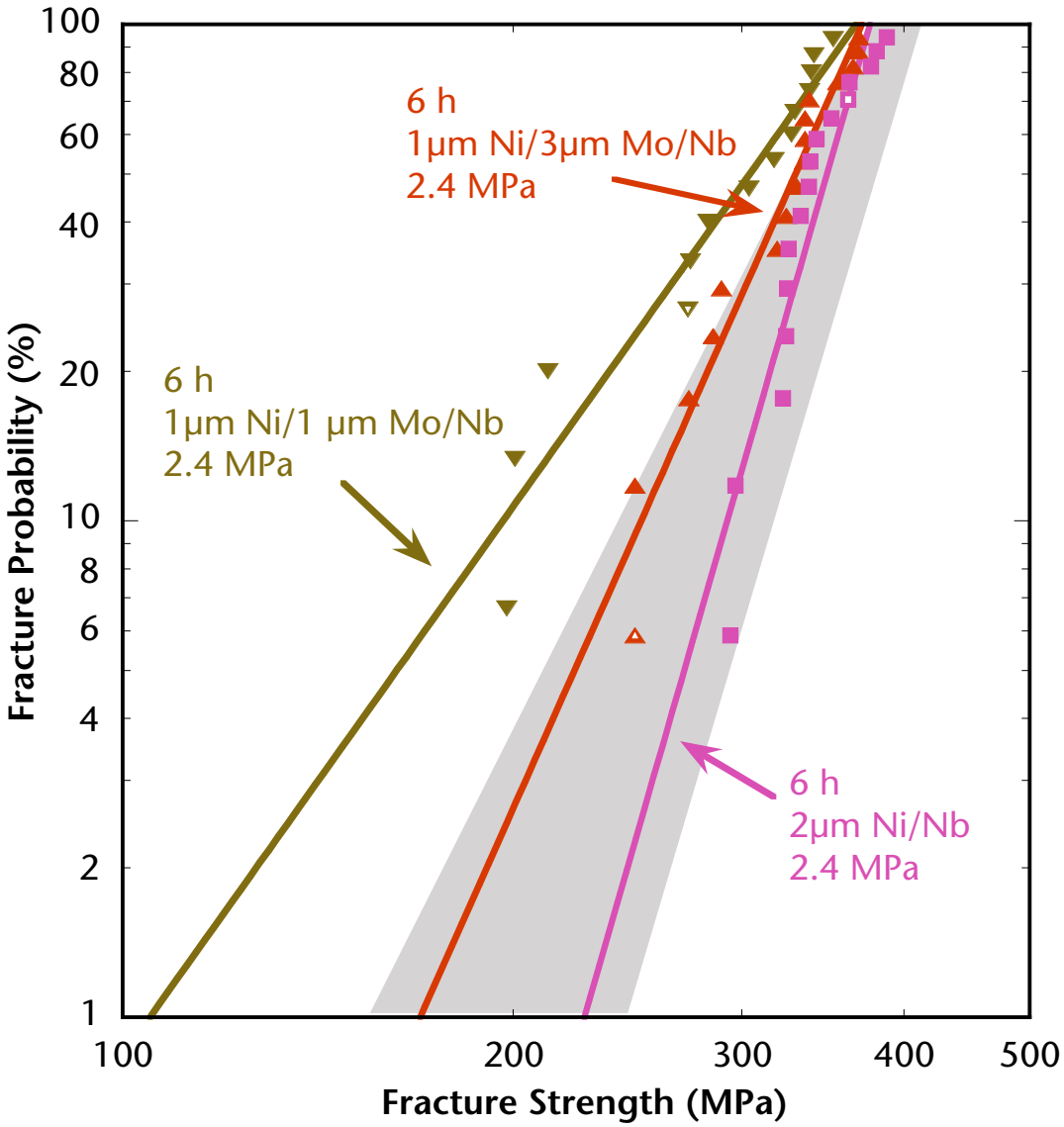

Figure 4.47: Influence of difference in Mo cladding thickness on fracture strength.

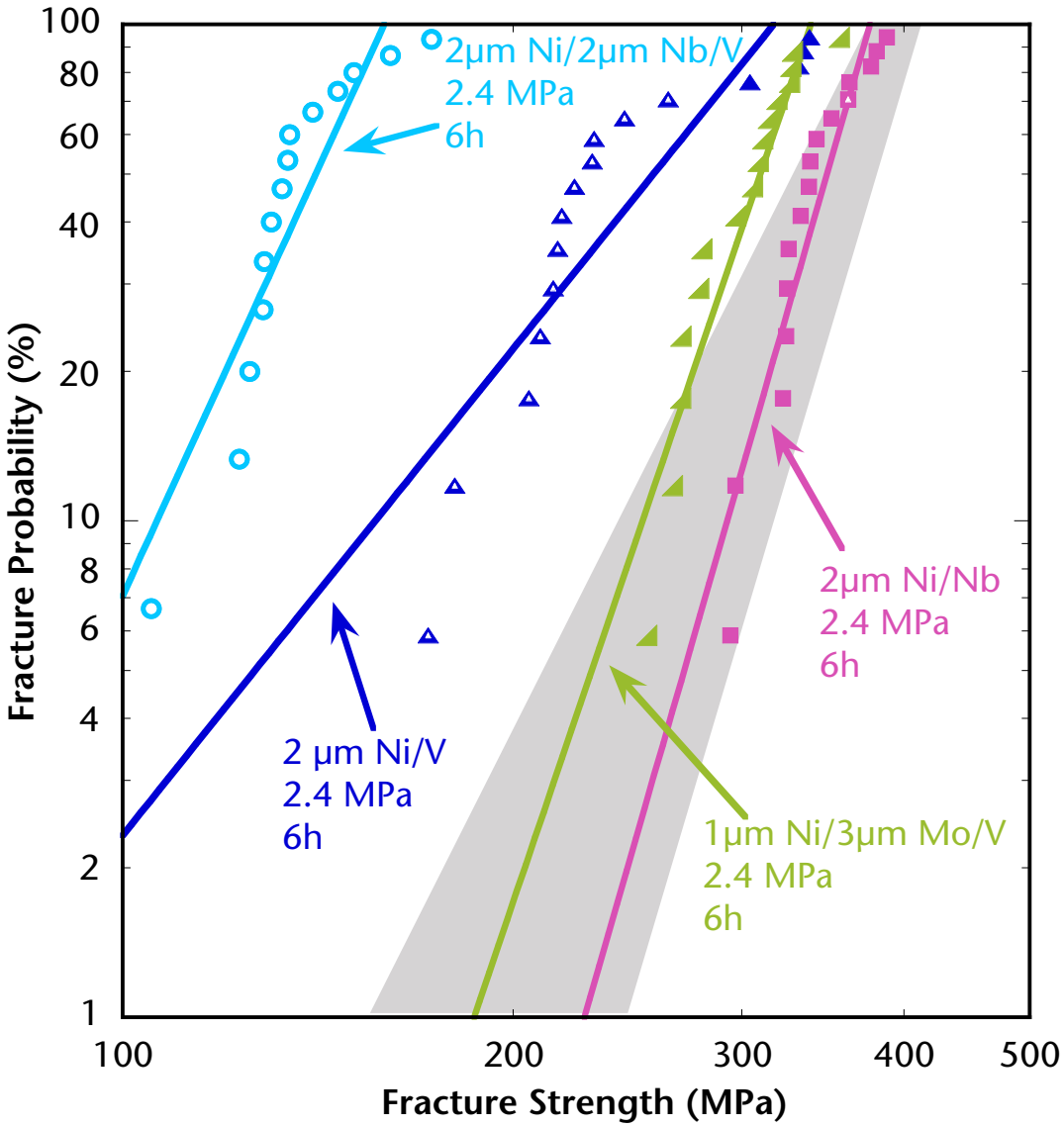

Figure 4.48: Fracture strengths for 999W Al_2O_3 bonded with 1-μm Ni/3-μm Mo/V/3-μm Mo/1-μm Ni interlayers. All bonds failed in the ceramic and were within the standard deviation range of the Ni/Nb/Ni bonds.

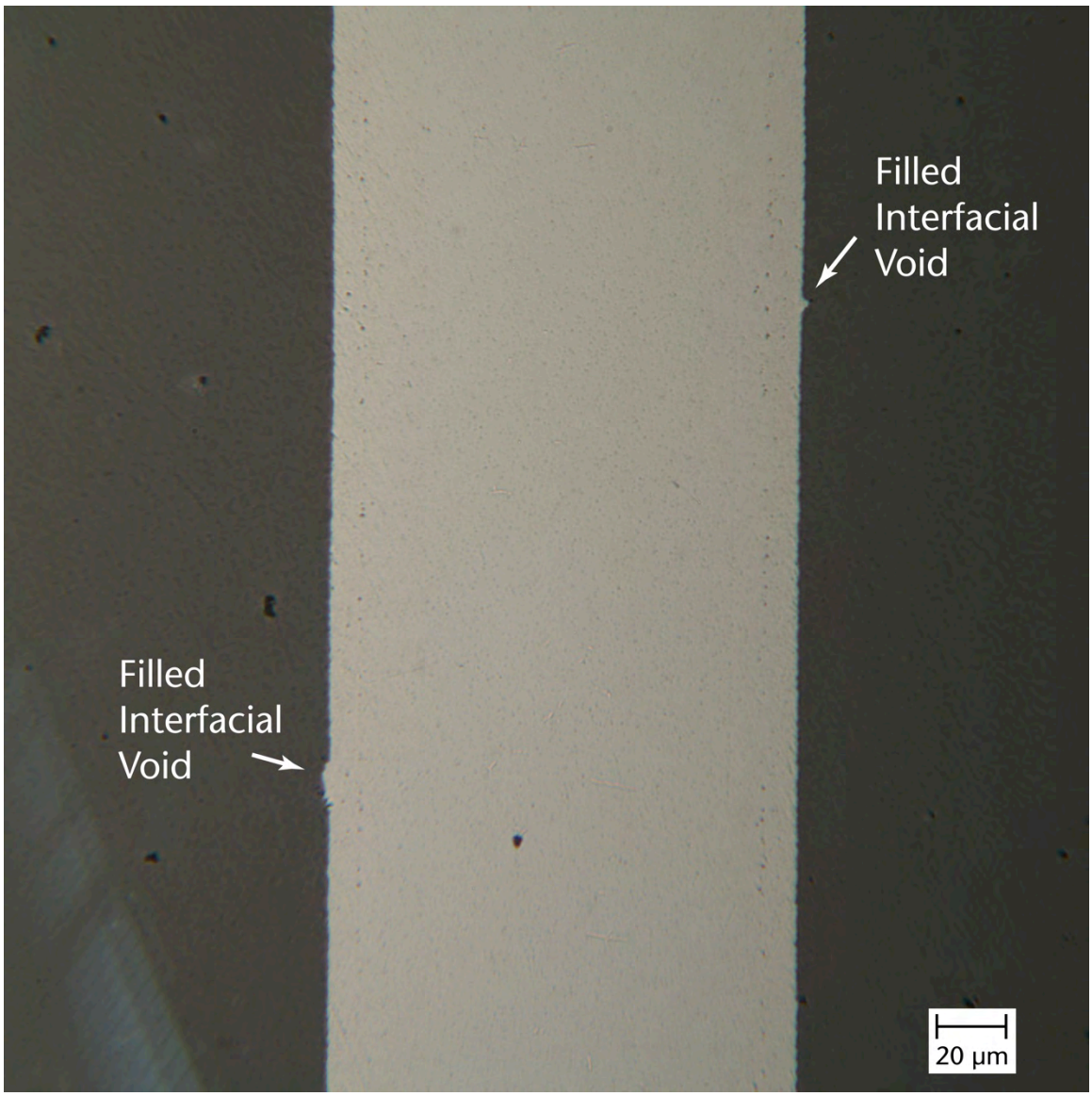

Figure 4.49: Al_2O_3 bonded using a 1-µm Ni/3-µm Mo/V/3-µm Mo/1-µm Ni interlayer. Note that the interlayer has filled imperfections in the Al_2O_3 at the interface.

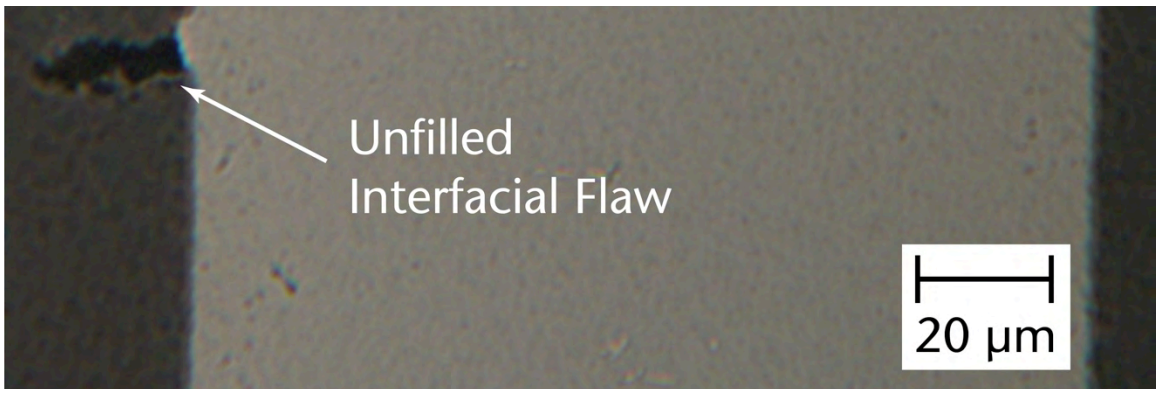

Figure 4.50: Unfilled interfacial flaw in a 1-μm Ni/3-μm Mo/V/3-μm Mo/1-μm Ni bond.

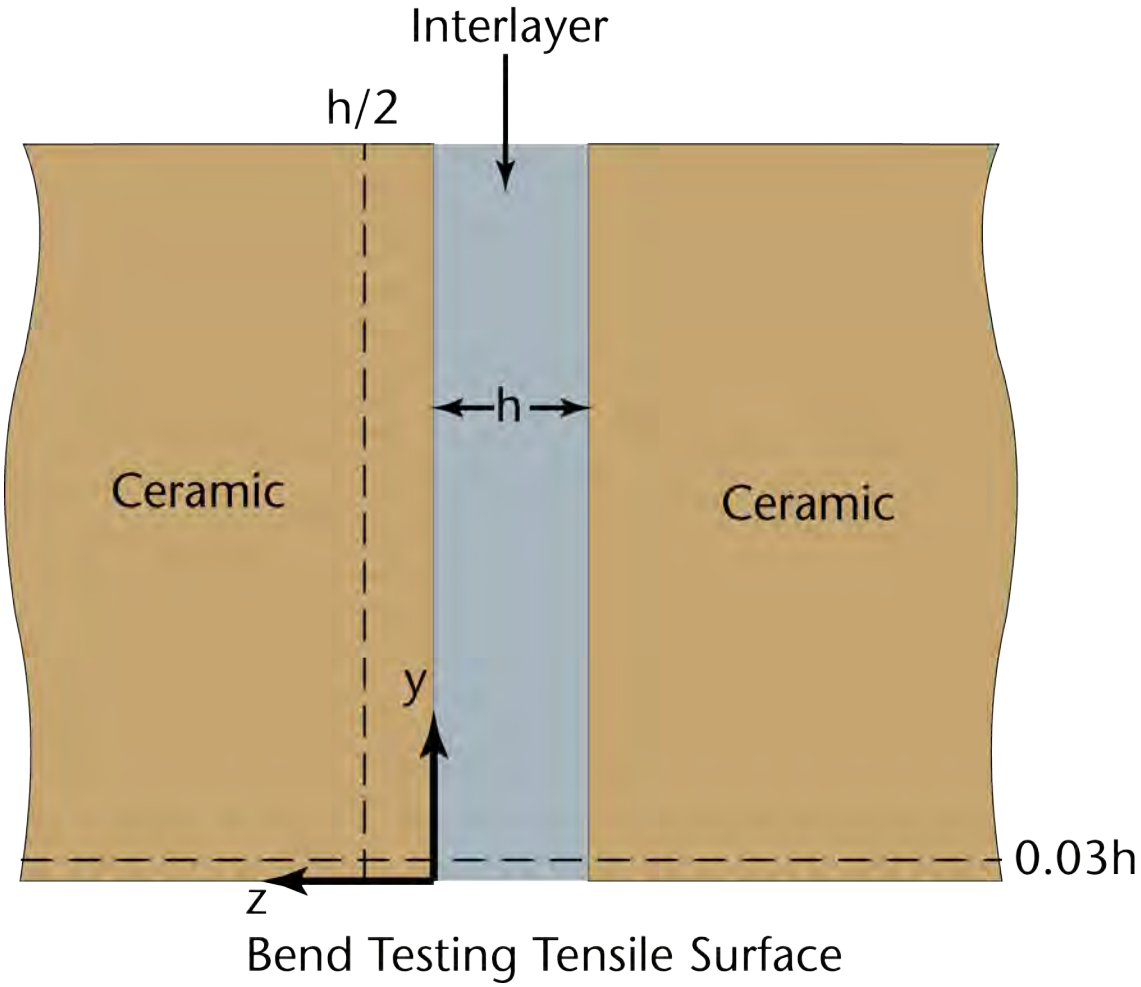

Figure 4.51: The maximum residual tensile stress location in a ceramic sandwich bonded structure is located at the intersection of the two dashed lines.

5. Summary and Conclusions

5.1 Summary of Work

PTLP bonding has been shown to be an effective alternative to traditional ceramic joining techniques such as brazing and diffusion bonding. The success of PTLP bonding relies on the proper selection of the interlayer components: the transient liquid must be able to flow into and fill strength-limiting interfacial flaws, the adhesion between the interlayer and the bulk ceramic must be sufficiently high to prevent interfacial failure, the formation of strength-reducing brittle phases at the interface should be minimized, and the residual stresses due to coefficient of thermal expansion (CTE) mismatch should be minimized. In addition, for PTLP bonding to occur rapidly, the solubility-diffusivity product of the MPD needs to be sufficiently large. To meet each of these requirements, the interlayer components need to be carefully selected.

In the past, it has been shown that using binary Ni/Nb/Ni interlayers, PTLP bonding can produce Al_2O_3 bonds that fail entirely within the ceramic component. The properties of Ni/Nb/Ni interlayers are exceptional. Molten Ni-Nb has a contact angle of ~90° on Al_2O_3, allowing it to wet the interface of PTLP-bonded assemblies and minimizing interfacial flaws and voids. The CTE of Nb is nearly identical to that of Al_2O_3, minimizing residual-stress formation. Finally, Ni is an anomalously fast diffuser in Nb [45], reducing the necessary bonding times. To determine if the Ni/Nb/Ni interlayer would be as successful at bonding ceramics other than pure Al_2O_3, it was used to join ZTA under 2.4-MPa and 6.7-kPa bonding pressures. It was found that with a 6.7-kPa bonding pressure, while a majority of the beams fail at the interface, the ZTA bond strengths were comparable to the highest strengths found bonding 999S Al_2O_3. Presence of the Ni_6Nb_7 intermetallic phase at the interface appeared to be the source of the interfacial failures. In contrast, most of the ZTA bonded at 2.4 MPa failed in the bulk ceramic, also at comparable strengths to the 999S Al_2O_3 bonds. Under a 2.4-MPa pressure, the interfacial failures that occurred did so at much lower fracture strengths than the ceramic failures. Minimal intermetallic phase was found on the fracture surface, suggesting another mechanism was responsible for the interfacial failures. It is thought that microcracking of the ZTA near the interface or near-interfacial degradation of the ZrO_2 phase may have contributed to the low fracture strengths, but more work is needed.

In many cases, interlayers that employ more than two components will be necessary to obtain the desired wetting, CTE, and solubility-diffusivity product for PTLP bonding. As control experiments, Al_2O_3 was bonded using binary Ni/Mo/Ni and Ni/V/Ni interlayers. For the Mo/Al_2O_3 system, the Ni-Mo liquid had a contact angle of 120° on Al_2O_3, and the $CTE_{Metal}<CTE_{Ceramic}$. For the V/$Al_2O_3$ system, the Ni-V liquid had a contact angle of 110° on Al_2O_3, and $CTE_{Metal}>CTE_{Ceramic}$. In both systems, every beam failed at the interface. However, the average fracture strength for the Ni/Mo/Ni beams was an order of magnitude lower than that of the Ni/V/Ni system. This was attributed to a number of factors. At room temperature, the Mo core was most likely below its DBTT, and thus not able to deform to reduce the residual stresses due to cooling. An intermetallic phase also formed along the interface due to the low Ni solubility in Mo, which acted as a fracture path for interfacial failure. Finally, when $CTE_{Metal}<CTE_{Ceramic}$, the interface is an energetically favorable fracture path, increasing the likelihood of interfacial fracture. In contrast, V is ductile at room temperature and has a relatively low yield stress, and Ni has a high solubility-diffusivity

coefficient in V. As a result, the residual stress in the Ni/V/Ni bonds was relatively low, and the interlayer fully homogenized during bonding. However, homogenization occurred so rapidly that little to no liquid-phase formation occurred, and thus flaws and voids remained at the interfacial surface. The low fracture strengths of the V bond were attributed to the presence of these flaws at the interface.

To determine whether the fracture strengths of Mo- and V-based cores could be improved by lowering the transient-liquid phases' contact angle, Nb-surface-modified core layers were fabricated. In both Ni/Nb/Mo/Nb/Ni and Ni/Nb/V/Nb/Ni systems, the fracture strength of the surface-modified-core assembly was lower than that of their Ni/Mo/Ni or Ni/V/Ni counterpart. In both systems, intermetallic phases were found at the interface, and caused interfacial fractures to occur. An examination of the likely solidification scenarios on the Ni-Nb-Mo ternary phase diagram suggested that the formation of a secondary phase was to be expected. A Ni-Nb-V phase diagram was not available, so it is unknown why the intermetallic phase formed despite the interlayer having homogenized.

Since the Ni-Mo liquid phase had the highest contact angle on Al_2O_3 of the systems examined, Mo-surface-modified cores were fabricated as well. For both the Ni/Mo/Nb/Mo/Ni and Ni/Mo/V/Mo/Ni systems, nearly all of fractures occurred in the ceramic component at fracture strengths approaching those of the Ni/Nb/Ni bonded assemblies. In both systems, the difference in average fracture strengths was attributed to the natural scatter in the Al_2O_3 itself in combination with higher residual stresses compared to the Ni/Nb/Ni bonds. In the Ni/Mo/Nb/Mo/Ni system, the presence of Mo appeared to cause the formation of grain-boundary phases in the Nb core, but no fractures were seen to initiate along the grain boundaries themselves. In the only sample that failed interfacially, no continuous intermetallic phases were found at the interface.

For the Ni/Mo/V/Mo/Ni system, the Mo in the core appeared to act as a barrier to Ni diffusion, increasing the quantity of transient liquid that formed at the interface during bonding. As a result, no flaws or voids were apparent at the interface after bonding, unlike in the Ni/V/Ni bonds. The fact that the Ni/Mo/V/Mo/Ni bonds had similar fracture strengths to that of the Ni/Nb/Ni assemblies is significant since the contact angle of the Ni-Mo-V transient-liquid phase is expected to be higher than that of Ni-Nb transient-liquid, and the CTE of V is significantly higher than that of Al_2O_3. This suggests that when designing PTLP interlayers, the quantity of the transient liquid may be more important than its contact angle and the yield stress of the core may be more important than its CTE.

5.2 Design of future PTLP systems

There are a number of factors that need to be taken into account during the materials selection process for PTLP bonding in order to rapidly obtain strong bonded assemblies. In an ideal system: the MPD will combine with the core to form a transient liquid at a relatively low temperature, the liquid phase will wet the ceramic interface, the MPD will have a high solubility and diffusivity in the core, the homogenized MPD will form a complete solid solution with the core material at the bonding temperature, the cladding/core combination will not react with itself or the base material to form an secondary phase at the interface, and the interlayer will have minimal CTE mismatch stresses form during cooling to room temperature. In the case where all of these criteria are met, strong bonds can be formed while

minimizing processing times and bonding temperatures. The minimal joining temperature is one where the liquid phase can form while the core and MPD also form a complete solid solution. The minimal joining time is the amount of time necessary to incorporate all of the MPD into solid solution with the core material, and is dependent on the MPD's solubility-diffusivity product in the core.

In real systems it is not always possible to satisfy all of these requirements simultaneously. Fortunately, as this study has shown, not all of these requirements must be met in order to have successful PTLP bonding. For example, high bond strengths can still be achieved despite the formation of secondary phases, as in the case of ZTA and 999S Al_2O_3 bonded under a 6.7-kPa pressure[1]. Transient liquids that do not wet the ceramic, such as the Mo-V-Ni liquid that formed in the 1-μm Ni/3-μm Mo/V/3-μm Mo/1-μm Ni bonds, can still flow and fill interfacial flaws when an applied pressure is used during the bonding process. And while residual stresses due to CTE mismatch can lower the ceramic fracture strength of a bonded assembly, as is suspected to have occurred in the 1-μm Ni/3-μm Mo/V/3-μm Mo/1-μm Ni bonds, a core material with a low yield stress and good ductility can be selected to minimize the residual stresses that do form. Finally, surface-modified cores can be used to regulate the diffusion of the MPD into the core, reducing the required cladding thickness to ensure transient-liquid formation. In future designs, this technique can be used to reduce the likelihood that strength-reducing intermetallics form along the interface.

From this work, it has been shown that refractory-metal-based interlayers can be used for the successful PTLP bonding of both ZTA and Al_2O_3 ceramics with high fracture strengths. Using the guidelines for interlayer design presented, it is expected that the fabrication of strong PTLP-bonded assemblies of other ceramic materials will be feasible in the future.

References

1. Hong, S. "Transient Liquid Phase Bonding of Al_2O_3 using Nb-based Multilayer Interlayers." *Ph.D. Thesis* (U.C. Berkeley, 2009).
2. Bartlow, C. "Numerical Simulations of Surface Roughness Effects on Liquid/Solid Interactions in One- and Two-Surface Systems." *Ph.D. Thesis* (U.C. Berkeley, 2011).
3. Hong, S., Bartlow, C., Reynolds, T., McKeown, J. & Glaeser, A. "Ultrarapid Transient-Liquid-Phase Bonding of Al_2O_3 Ceramics." *Advanced Materials* **20**, 4799–4803 (2008).
4. Greenwood J. & Williamson, J. "Contact of Nominally Flat Surfaces." *Proceedings of the Royal Society of London Series A-Mathematical and Physical Sciences* **295**, 300–319 (1966).
5. Archard, J. "Elastic Deformation and the Laws of Friction." *Proceedings of the Royal Society of London Series A-Mathematical and Physical Sciences* **243**, 190–205 (1957).
6. Childs, T. "Persistence of Roughness between Surfaces in Static Contact." *Proceedings of the Royal Society of London Series A-Mathematical, Physical and Engineering Sciences* **353**, 35–53 (1977).
7. Nicholas, M., Forgan, R. & Poole, D. "The Adhesion of Metal/Alumina Interfaces." *Journal of Materials Science* **3**, 9–14 (1968).
8. Nicholas, M. "The Strength of Metal/Alumina Interfaces." *Journal of Materials Science* **3**, 571–576 (1968).
9. Eustathopoulos, N., Nicholas, M., Drevet, B. & Cahn, R. *Wettability at High Temperatures*. (Elsevier, 1999).
10. Saiz, E., Tomsia, A. & Cannon, R. "Triple Line Ridging and Attachment in High-Temperature Wetting." *Scripta Materialia* **44**, 159–164 (2001).
11. Wenzel, R. "Resistance of Solid Surfaces to Wetting by Water." *Industrial and Engineering Chemistry* **28**, 988–994 (1936).
12. Wenzel, R. "Surface Roughness and Contact Angle." *The Journal of Physical Chemistry* **53**, 1466–1467 (1949).
13. Wolansky, G. & Marmur, A. "Apparent Contact Angles on Rough Surfaces: the Wenzel Equation Revisited." *Colloids and Surfaces A-Physicochemical and Engineering Aspects* **156**, 381–388 (1999).
14. Nakae, H., Inui, R., Hirata, Y. & Saito, H. "Effects of Surface Roughness on Wettability." *Acta Materialia* **46**, 2313–2318 (1998).
15. Nakae, H., Yoshida, M. & Yokota, M. "Effects of Roughness Pitch of Surfaces on Their Wettability." *Journal of Materials Science* **40**, 2287–2293 (2005).
16. Nogi, K., Oishi, K. & Ogino, K. "Wettability of Solid Oxides by Liquid Pure Metals." *Materials Transactions JIM* **30**, 137–145 (1989).
17. Levi, G., Scheu, C. & Kaplan, W. "Segregation of Aluminium at Nickel-Sapphire Interfaces." *Interface Science* **9**, 213–220 (2001).

18. Humenik, M. & Kingery, W. "Metal-Ceramic Interactions: III, Surface Tension and Wettability of Metal-Ceramic Systems." *Journal of the American Ceramic Society* **37**, 18–23 (1954).
19. Armstrong, W., Chaklader, A. & Clarke, J. "Interface Reactions Between Metals and Ceramics: I, Sapphire-Nickel Alloys." *Journal of the American Ceramic Society* **45**, 115–118 (1962).
20. Ritter, J. & Burton, M. "Adherence and Wettability of Nickel, Nickel- Titanium Alloys, and Nickel-Chromium Alloys to Sapphire." *Transactions of the Metallurgical Society of AIME* **239**, 21–26 (1967).
21. Crispin, R. & Nicholas, M. "The Wetting and Bonding Behaviour of Some Nickel Alloy-Alumina Systems." *Journal of Materials Science* **11**, 17–21 (1976).
22. Ogino, K. & Taimatsu, H. "Effect of Oxygen on the Surface-Tension of Liquid Nickel and the Wettability of Alumina by Liquid Nickel." *Journal of the Japan Institute of Metals* **43**, 871–876 (1979).
23. Kritsalis, P., Merlin, V., Coudurier, L. & Eustathopoulos, N. "Effect of Cr on Interfacial Interaction and Wetting Mechanisms in Ni Alloy/Alumina Systems." *Acta Metallurgica et Materialia* **40**, 1167–1175 (1992).
24. Chatain, D., Rivollet, I. & Eustathopoulos, N. "Adhésion Thermodynamique Dans Les Systèmes Non Réactifs Métal Liquide-Alumine." *Journal de Chimie Physique* **83**, 561–567 (1986).
25. Wan, C., Kritsalis, P., Drevet, B. & Eustathopoulos, N. "Optimization of Wettability and Adhesion in Reactive Nickel-Based Alloys/Alumina Systems by a Thermodynamic Approach." *Materials Science and Engineering A: Structural Materials* **207**, 181–187 (1996).
26. Nicholas, M., Valentine, T. & Waite, M. "The Wetting of Alumina by Copper Alloyed with Titanium and Other Elements." *Journal of Materials Science* **15**, 2197–2206 (1980).
27. Cao, H., Thouless, M. & Evans, A. "Residual-Stresses and Cracking in Brittle Solids Bonded with a Thin Ductile Layer." *Acta Metallurgica* **36**, 2037–2046 (1988).
28. He, M. & Evans, A. "The Strength and Fracture of Metal Ceramic Bonds." *Acta Metallurgica et Materialia* **39**, 1587–1593 (1991).
29. Dalgleish, B., Saiz, E., Tomsia, A., Cannon, R. & Ritchie, R. "Interface Formation and Strength in Ceramic-Metal Systems." *Scripta Metallurgica Et Materialia* **31**, 1109–1114 (1994).
30. Kovalev, S., Miranzo, P. & Osendi, M. "Finite Element Simulation of Thermal Residual Stresses in Joining Ceramics with Thin Metal Interlayers." *Journal of the American Ceramic Society* **81**, 2342–2348 (1998).
31. Gibbesch, B. & Elssner, G. "Ultra High-Vacuum Diffusion Bonded Nb-Al_2O_3 and Cu-Al_2O_3 Joints - the Role of Welding Temperature and Sputter Cleaning." *Acta Metallurgica et Materialia* **40**, S59–S66 (1992).
32. Bailey, F. & Black, K. "Effect of Ambient Atmosphere on Gold-to-Alumina Solid-State Reaction Bond." *Journal of Materials Science* **13**, 1606–1608 (1978).

33. Bailey, F. & Black, K. "Gold-to-Alumina Solid-State Reaction Bonding." *Journal of Materials Science* **13**, 1045–1052 (1978).
34. Allen, R. & Borbidge, W. "Solid-State Metal Ceramic Bonding of Platinum to Alumina." *Journal of Materials Science* **18**, 2835–2843 (1983).
35. Serier, B., Berroug, A., Juve, D., Treheux, D. & Moya, E. "Silver-Alumina Solid State Bonding: Study of Diffusion and Toughness Close to the Interface." *Journal of the European Ceramic Society* **12**, 385–390 (1993).
36. Serier, B., Bouiadjra, B. & Treheux, D. "Mechanism of Adhesion at Solid State Bonding Ceramic-Metal: Case of Silver-Alumina Couple." *Euro Ceramics VIII, Pts 1-3* **264-268**, 667–670 (2004).
37. Nicholas, M. & Crispin, R. "Diffusion Bonding Ceramics with Ductile Interlayers." in *Science of Ceramics* **14**, 539–544 (Academic Press for the British Ceramic Society, 1988).
38. Çam, G. & Koçak, M. "Progress in Joining of Advanced Materials." *International Materials Reviews* **43**, 1–44 (1998).
39. Derby, B. in *Joining of Ceramics* (Nicholas, M.) 94–110 (Chapman and Hall, 1990).
40. Klomp, J. & Vandeven, A. "Parameters in Solid-State Bonding of Metals to Oxide Materials and the Adherence of Bonds." *Journal of Materials Science* **15**, 2483–2488 (1980).
41. Almond, E., Cottenden, A. & Gee, M. "Metallurgy of Interfaces in Hardmetal Metal Diffusion Bonds." *Metal Science* **17**, 153–158 (1983).
42. Derby, B. & Wallach, E. "Theoretical-Model for Diffusion Bonding." *Metal Science* **16**, 49–56 (1982).
43. Derby, B. & Wallach, E. "Diffusion Bonding - Development of Theoretical-Model." *Metal Science* **18**, 427–431 (1984).
44. Garmong, G., Paton, N. & Argon, A. "Attainment of Full Interfacial Contact during Diffusion Bonding." *Metallurgical Transactions A-Physical Metallurgy and Materials Science* **6**, 1269–1279 (1975).
45. Razumovskii, I., Mishin, Y. & Herzig, C. "Investigation of Ni-63 Diffusion along Stationary and Moving Grain Boundaries in Nb." *Materials Science and Engineering A-Structural Materials Properties Microstructure and Processing* **212**, 45–50 (1996).
46. Hill, A. & Wallach, E. "Modeling Solid-State Diffusion Bonding." *Acta Metallurgica* **37**, 2425–2437 (1989).
47. Murray, P., Lively, D. & Williams, J. in *Ceramic Fabrication Processes* (Kingery, W. D.) 147–171 (John Wiley and Sons LTD., 1958).
48. Coble, R. & Ellis, J. "Hot-Pressing Alumina—Mechanisms of Material Transport." *Journal of the American Ceramic Society* **46**, 438–441 (1963).
49. Coble, R. "Diffusion Models for Hot Pressing with Surface Energy and Pressure Effects as Driving Forces." *Journal of Applied Physics* **41**, 4798–4807 (1970).
50. Mangsen, G., Lambertson, W. & Best, B. "Hot Pressing of Aluminum Oxide." *Journal of the American Ceramic Society* **43**, 55–59 (1960).

51. Rossi, R. & Fulrath, R. "Final Stage Densification in Vacuum Hot-Pressing of Alumina." *Journal of the American Ceramic Society* **48**, 558–564 (1965).
52. Wilkinson, D. & Ashby, M. "Pressure Sintering by Power Law Creep." *Acta Metallurgica* **23**, 1277–1285 (1975).
53. Reimanis, I. "Pore Removal during Diffusion Bonding of Nb-Al_2O_3 Interfaces." *Acta Metallurgica et Materialia* **40**, S67–S74 (1992).
54. Beraud, C., Courbiere, M., Esnouf, C., Juve, D. & Treheux, D. "Study of Copper-Alumina Bonding." *Journal of Materials Science* **24**, 4545–4554 (1989).
55. Espe, W., Hix, P. & Kejhar, J. "A High-Vacuumtight, Reliable, Brazed Joint Between Ceramic and Metal. Pt. 1." *Vacuum Tech* **16**, 1–8 (1966).
56. Das, S., Tiwari, A. & Kulkarni, A. "Thermo-Compression Bonding of Alumina Ceramics to Metal." *Journal of Materials Science* **39**, 3345–3355 (2004).
57. Persson, B. "Adhesion between Elastic Bodies with Randomly Rough Surfaces." *Physical Review Letters* **89**, 245502 (2002).
58. Nicholas, M. & Crispin, R. "Diffusion Bonding Stainless Steel to Alumina Using Aluminium Interlayers." *Journal of Materials Science* **17**, 3347–3360 (1982).
59. Espe, W., Hix, P. & Kejhar, J. "A High-Vacuumtight, Reliable, Brazed Joint Between Ceramic and Metal. Pt. 2." *Vacuum* **16**, 61–65 (1966).
60. Urena, A., de Salazar, J. & Quinones, J. "Diffusion Bonding of Alumina to Steel Using Soft Copper Interlayer." *Journal of Materials Science* **27**, 599–606 (1992).
61. Wang, H., Gerberich, W. & Angelo, J. "Interfacial Reactions and Adhesion Strength of Metal/Ceramic Composites." *Journal of Materials Research* **10**, 2367–2373 (1995).
62. Travessa, D. & Ferrante, M. "The Al_2O_3-Titanium Adhesion in the View of the Diffusion Bonding Process." *Journal of Materials Science* **37**, 4385–4390 (2002).
63. Zalar, A., Baretzky, B., Hofmann, S., Rühle, M. & Panjan, P. "Interfacial Reactions in Al_2O_3/Ti, Al_2O_3/Ti_3Al and Al_2O_3/TiAl Bilayers." *Thin Solid Films* **352**, 151–155 (1999).
64. Kliauga, A. & Ferrante, M. "Interface Compounds Formed During the Diffusion Bonding of Al_2O_3 to Ti." *Journal of Materials Science* **35**, 4243–4249 (2000).
65. Gubbels, G., Heikinheimo, L. & Klomp, J. "A Comparison between Titanium Alumina Diffusion Bonding and Titanium Active Brazing." *Zeitschrift Für Metallkunde* **85**, 828–832 (1994).
66. Suezawa, Y. & Izui, H. "Effects of Surface Roughness of Base Metals on the Residual Stress of Filler Metals at Brazed Joints." *Materials Science Forum* **404-407**, 611–616 (2002).
67. Hammond, J., David, S. & Santella, M. "Brazing Ceramic Oxides to Metals at Low Temperatures." *Welding Journal* **67**, S227–S232 (1988).
68. Mizuhara, H. & Mally, K. "Ceramic-to-Metal Joining with Active Brazing Filler Metal." *Welding Journal* **64**, 27–32 (1985).
69. Elssner, G. & Petzow, G. "Metal Ceramic Joining." *ISIJ International* **30**, 1011–1032 (1990).

70. Hosking, F., Cadden, C. & Yang, N. "Microstructural and Mechanical Characterization of Actively Brazed Alumina Tensile Specimens." *Welding Journal* **79**, 222S–230S (2000).
71. Loehman, R. & Tomsia, A. "Wetting and Joining of Mullite Ceramics by Active-Metal Braze Alloys." *Journal of the American Ceramic Society* **77**, 271–274 (1994).
72. Hong, S. "Effects of Processing Conditions on the Interlayer Microstructure and Fracture Strengths in Reduced-Temperature Transient-Liquid-Phase Bonding of Alumina." *M.S. Thesis*, (U.C. Berkeley, 2006).
73. Nicholas, M. & Mortimer, D. "Ceramic/Metal Joining for Structural Applications." *Materials Science and Technology* **1**, 657–665 (1985).
74. Nicholas, M. *Joining Processes: Introduction to Brazing and Diffusion Bonding*. (Kluwer Academic Publishers, 1998).
75. Ed: Bellosi, A., Kosmaç, T. & Tomsia, A. *Interfacial Science in Ceramic Joining*. **58**, (Kluwer Academic Publishers, 1998).
76. Duvall, D. & Owczarski, W. "TLP Bonding - A New Method for Joining Heat Resistant Alloys." *Welding Journal* **53**, 203–214 (1974).
77. Ikawa, H., Nakao, Y. & Isai, T. "Theoretical Considerations on the Metallurgical Process in TLP Bonding of Nickel-Base Superalloys." *Transactions of the Japanese Welding Society* **10**, 25–29 (1979).
78. MacDonald, W. & Eagar, T. "Transient Liquid Phase Bonding." *Annual Review of Materials Science* **22**, 23–46 (1992).
79. Tuah-Poku, I., Dollar, M. & Massalski, T. "A Study of the Transient Liquid-Phase Bonding Process Applied to a Ag-Cu-Ag Sandwich Joint." *Metallurgical Transactions A-Physical Metallurgy and Materials Science* **19**, 675–686 (1988).
80. Gale, W. & Butts, D. "Transient Liquid Phase Bonding." *Science and Technology of Welding and Joining* **9**, 283–300 (2004).
81. Zhou, Y., Gale, W. & North, T. "Modelling of Transient Liquid Phase Bonding." *International Materials Reviews* **40**, 181–196 (1995).
82. Duvall, D., Owczarski, W. & Paulonis, D. "TLP Bonding - New Method for Joining Heat-Resistant Alloys." *Welding Journal* **53**, 203–214 (1974).
83. Gale, W. & Orel, S. "A Microstructural Investigation of NiAl/Ni-Si-B/NiAl Transient Liquid Phase Bonds." *Journal of Materials Science* **31**, 345–349 (1996).
84. Gale, W. & Wallach, E. "Microstructural Development in Transient Liquid-Phase Bonding." *Metallurgical Transactions A-Physical Metallurgy and Materials Science* **22**, 2451–2457 (1991).
85. Gale, W. & Guan, Y. "Transient Liquid-Phase Bonding in the NiAl/Cu/Ni System-A Microstructural Investigation." *Metallurgical and Materials Transactions A* **27**, 3621–3629 (1996).
86. Gale, W. & Guan, Y. "Microstructure and Mechanical Properties of Transient Liquid Phase Bonds Between NiAl and a Nickel-Base Superalloy." *Journal of Materials Science* **34**, 1061–1071 (1999).
87. Lynch, J., Feinstein, L. & Huggins, R. "Brazing by Diffusion-Controlled Formation of Liquid Intermediate Phase." *Welding Journal* **38**, 85–89 (1959).

88. Niemann, J. & Garrett, R. "Eutectic Bonding of Boron-Aluminum Structural Components. 1. Evaluation of Critical Processing Parameters." *Welding Journal* **53**, S175–S184 (1974).
89. MacDonald, W. & Eagar, T. "Isothermal Solidification Kinetics of Diffusion Brazing." *Metallurgical and Materials Transactions A-Physical Metallurgy and Materials Science* **29**, 315–325 (1998).
90. Nakao, Y., Nishimoto, K., Shinozaki, K. & Kang, C. "Theoretical Research on Transient Liquid Insert Metal Diffusion Bonding of Nickel Base Alloys." *Transactions of the Japan Welding Society* **20**, 60–65 (1989).
91. Kokawa, H., Lee, C. & North, T. "Effect of Grain Boundaries on Isothermal Solidification During Transient Liquid Phase Brazing." *Metallurgical and Materials Transactions A* **22**, 1627–1631 (1991).
92. Saida, K., Zhou, Y. & North, T. "The Influence of Base Metal Grain Size on Isothermal Solidification During Transient Liquid-Phase Brazing of Nickel." *Journal of Materials Science* **28**, 6427–6432 (1993).
93. Mishin, Y., Herzig, C., Bernardini, J. & Gust, W. "Grain Boundary Diffusion: Fundamentals to Recent Developments." *International Materials Reviews* **42**, 155–178 (1997).
94. Zhou, Y. & North, T. "Numerical Model for the Effect of Grain Boundaries on the Total Amount Diffused." *Acta Metallurgica et Materialia* **42**, 1025–1029 (1994).
95. Smidoda, K., Gottschalk, W. & Gleiter, H. "Diffusion in Migrating Interfaces." *Acta Metallurgica* **26**, 1833–1836 (1978).
96. Olander, D. & El-Saied, U. "The Effect of Grain Boundary Motion on the Kinetics of Solute Penetration Into a Polycrystalline Medium." *Acta Metallurgica et Materialia* **40**, 1329–1336 (1992).
97. Glaeser, A. & Evans, J. "Effect of Grain Boundary Migration on Apparent Boundary Diffusion Coefficients." *Acta Metallurgica* **34**, 1545–1552 (1986).
98. Kaur, I., Mishin, Y. & Gust, W. in *Fundamentals of Grain and Interphase Boundary Diffusion* 304–377 (John Wiley and Sons LTD., 1995).
99. Zhou, Y. & North, T. "Process Modeling and Optimized Parameter Selection During Transient Liquid Phase Bonding." *Zeitschrift Für Metallkunde* **85**, 775–780 (1994).
100. Shalz, M., Dalgleish, B., Tomsia, A. & Glaeser, A. "Ceramic Joining I - Partial Transient Liquid-Phase Bonding of Alumina via Cu/Pt Interlayers." *Journal of Materials Science* **28**, 1673–1684 (1993).
101. Shalz, M., Dalgleish, B., Tomsia, A. & Glaeser, A. "Ceramic Joining II - Partial Transient Liquid-Phase Bonding of Alumina via Cu/Ni-Cu Multilayer Interlayers." *Journal of Materials Science* **29**, 3200–3208 (1994).
102. Sugar, J., McKeown, J., Marks, R. & Glaeser, A. "Liquid-Film-Assisted Formation of Alumina/Niobium Interfaces." *Journal of the American Ceramic Society* **85**, 2523–2530 (2002).
103. Iino, Y. & Taguchi, N. "Interdiffusing Metals Layer Technique of Ceramic Metal-Bonding." *Journal of Materials Science Letters* **7**, 981–982 (1988).

104. Iino, Y. "Partial Transient Liquid-Phase Metals Layer Technique of Ceramic Metal-Bonding." *Journal of Materials Science Letters* **10**, 104–106 (1990).
105. Ceccone, G., Nicholas, M., Peteves, S., Tomsia, A., Dalgleish, B. & Glaeser, A. "An Evaluation of the Partial Transient Liquid Phase Bonding of Si_3N_4 Using Au Coated Ni-22Cr Foils." *Acta Materialia* **44**, 657–667 (1996).
106. Dalgleish, B., Tomsia, A., Nakashima, K., Locatelli, M. & Glaeser, A. "Low-Temperature Routes to Joining Ceramics for High-Temperature Applications." *Scripta Metallurgica et Materialia* **31**, 1043–1048 (1994).
107. Locatelli, M., Tomsia, A., Nakashima, K., Dalgleish, B. & Glaeser, A. "New Strategies for Joining Ceramics for High-Temperature Applications." *Key Engineering Materials* **111-112**, 157–190 (1995).
108. Locatelli, M., Dalgleish, B., Nakashima, K., Tomsia, A. & Glaeser, A. "New Approaches to Joining Ceramics for High-Temperature Applications." *Ceramics International* **23**, 313–322 (1997).
109. Burger, K. & Rühle, M. "Material Transport Mechanisms during the Diffusion Bonding of Niobium to Al_2O_3." *Ultramicroscopy* **29**, 88–97 (1989).
110. Evans, A., Lu, M., Schmauder, S. & Rühle, M. "Some Aspects of the Mechanical Strength of Ceramic Metal Bonded Systems." *Acta Metallurgica* **34**, 1643–1655 (1986).
111. Morozumi, S., Kikuchi, M. & Nishino, T. "Bonding Mechanism between Alumina and Niobium." *Journal of Materials Science* **16**, 2137–2144 (1981).
112. Bruley, J., Brydson, R., Müllejans, H., Mayer, J., Gutekunst, G., Mader, W., Knauss, D. & Rühle, M. "Investigations of the Chemistry and Bonding at Niobium-Sapphire Interfaces." *Journal of Materials Research* **9**, 2574–2583 (1994).
113. McKeown, J., Sugar, J., Gronsky, R. & Glaeser, A. "Processing of Alumina-Niobium Interfaces via Liquid-Film-Assisted Joining." *Welding Journal* **84**, 41S–51S (2005).
114. Gibbesch, B., Elssner, G., Mader, W., Fischmeister, H. & Kraft, W. "Ultrahigh Vacuum Diffusion Bonding of Nb and Cu Single Crystals to Sapphire." in *Joining Ceramics, Glass, and Metal International Conference* 65–72 (Feb. 1989).
115. McKeown, J. "Processing and Characterization of Alumina-Niobium Interfaces Produced via Liquid-Film-Assisted Joining." *M.S. Thesis* (U.C. Berkeley, 2003).
116. Shalz, M., Dalgleish, B., Tomsia, A., Cannon, R. & Glaeser, A. "Ceramic Joining III - Bonding of Alumina via Cu/Nb/Cu Interlayers." *Journal of Materials Science* **29**, 3678–3690 (1994).
117. Ablitzer, D. "Diffusion of Niobium, Iron, Cobalt, Nickel and Copper in Niobium." *Philosophical Magazine* **35**, 1239–1256 (1977).
118. Agarwala, R. & Hirano, K. "Diffusion of Nickel in Niobium." *Transactions of the Japan Institute of Metals* **13**, 425–427 (1972).
119. Reynolds, T. "Influence of Processing Conditions and Interlayer Composition on the Interfacial Microstructure and Fracture Strength of Alumina/Niobium Assemblies Produced *via* Partial-Transient-Liquid-Phase Bonding." *M.S. Thesis* (U.C. Berkeley, 2009).

120. Reynolds, T., Bartlow, C., Hong, S. & Glaeser, A. "Rapid Transient-Liquid-Phase Bonding of Al_2O_3 Ceramics." in *2009 TMS Annual Meeting and Exhibition* **3**, 645–652 (2009).
121. Wuchina, E., Opeka, M., Causey, S., Buesking, K., Spain, J., Cull, A., Routbort, J. & Guitierrez-Mora, F. "Designing for Ultrahigh-Temperature Applications: the Mechanical and Thermal Properties of HfB_2, HfC_x, HfN_x, and Alpha-HfN." *Journal of Materials Science* **39**, 5939–5949 (2004).
122. Aldebert, P. & Traverse, J. "Alpha-Al_2O_3: A High-Temperature Thermal Expansion Standard." *High Temperatures - High Pressures* **16**, 127–135 (1984).
123. Wang, K. & Reeber, R. "The Role of Defects on Thermophysical Properties: Thermal Expansion of V, Nb, Ta, Mo and W." *Materials Science & Engineering R-Reports* **23**, 101–137 (1998).
124. Riley, F. *Structural Ceramics: Fundamentals and Case Studies*. (Cambridge University Press, 2009).
125. Okamoto, H. "Nb-Ni (Niobium-Nickel)." *Journal of Phase Equilibria and Diffusion* **27**, 314–314 (2006).
126. Teitz, T. & Wilson, J. *Behavior and Properties of Refractory Metals*. (Stanford University Press, 1965).
127. *Landolt-Börnstein: Group III Condensed Matter*. **26**, 41–54 (1990).
128. Akselsen, O. "Advances in Brazing of Ceramics." *Journal of Materials Science* **27**, 1989–2000 (1992).
129. Evans, A. & Heuer, A. "Transformation Toughening in Ceramics - Martensitic Transformations in Crack-Tip Stress-Fields." *Journal of the American Ceramic Society* **63**, 241–248 (1980).
130. Wang, J. & Stevens, R. "Zirconia-Toughened Alumina (ZTA) Ceramics." *Journal of Materials Science* **24**, 3421–3440 (1989).
131. Green, D. "A Technique for Introducing Surface Compression into Zirconia Ceramics." *Journal of the American Ceramic Society* **66**, c178–c179 (1983).
132. Green, D. "Critical Microstructures for Microcracking in Al_2O_3-ZrO_2 Composites." *Journal of the American Ceramic Society* **65**, 610–614 (1982).
133. Heuer, A., Claussen, N., Kriven, W. & Ruhle, M. "Stability of Tetragonal ZrO_2 Particles in Ceramic Matrices." *Journal of the American Ceramic Society* **65**, 642–650 (1982).
134. Becher, P. "Transient Thermal-Stress Behavior in ZrO_2-Toughened Al_2O_3." *Journal of the American Ceramic Society* **64**, 37–39 (1981).
135. Heuer, A., Lange, F., Swain, M. & Evans, A. "Transformation Toughening: an Overview." *Journal of the American Ceramic Society* **69**, i–iv (1986).
136. Witek, S. & Butler, E. "Zirconia Particle Coarsening and the Effects of Zirconia Additions on the Mechanical Properties of Certain Commercial Aluminas." *Journal of the American Ceramic Society* **69**, 523–529 (1986).
137. Hong, S., Reynolds, T., Bartlow, C. & Glaeser, A. "Rapid Transient-Liquid-Phase Bonding of Al_2O_3 with Microdesigned Ni/Nb/Ni Interlayers 2010." *International Journal for Materials Research* **101**, 133–142 (2010).

138. Lee, S., Edalati, K. & Horita, Z. "Microstructures and Mechanical Properties of Pure V and Mo Processed by High-Pressure Torsion." *Materials Transactions, JIM* **51**, 1072–1079 (2010).
139. Wronski, A., Chilton, A. & Capron, E. "The Ductile-Brittle Transition in Polycrystalline Molybdenum." *Acta Metallurgica* **17**, 751–755 (1969).
140. Schneibel, J., Brady, M. & Kruzic, J. "On the Improvement of the Ductility of Molybdenum by Spinel ($MgAl_2O_4$) Particles." *Zeitschrift Für Metallkunde* **96**, 632–637 (2005).
141. Miller, M. & Bryhan, A. "Effect of Zr, B and C Additions on the Ductility of Molybdenum." *Materials Science and Engineering A: Structural Materials* **327**, 80–83 (2002).
142. Okamoto, H. "Ni-O (Nickel-Oxygen)." *Journal of Phase Equilibria* **18**, 404 (1997).
143. Jacob, K., Kale, G. & Iyengar, G. "Phase Equilibria and Thermodynamic Properties in the System Ni-Mo-O." *Journal of Materials Science* **22**, 4274–4280 (1987).
144. Brewer, L. & Lamoreaux, R. in *Binary Alloy Phase Diagrams* (Massalski, T.) **3**, 2639–2641 (ASM International, 1990).
145. Penisson, J. & Vystavel, T. "Wetting of Molybdenum Grain Boundaries by Nickel: Effect of the Boundary Structure and Energy." *Acta Materialia* **48**, 3303–3310 (2000).
146. Heijwegen, C. & Rieck, G. "Diffusion in Mo-Ni, Mo-Fe and Mo-Co Systems." *Acta Metallurgica* **22**, 1269–1281 (1974).
147. Hwang, K. & Huang, H. "Identification of the Segregation Layer and Its Effects on the Activated Sintering and Ductility of Ni-Doped Molybdenum." *Acta Materialia* **51**, 3915–3926 (2003).
148. Rabkin, E., Weygand, D., Straumal, B., Semenov, V., Gust, W. & Brechet, Y. "Liquid Film Migration in a Mo(Ni) Bicrystal." *Philosophical Magazine Letters* **73**, 187–193 (1996).
149. Shi, X. & Luo, J. "Grain Boundary Wetting and Prewetting in Ni-Doped Mo." *Applied Physics Letters* **94**, 251908 (2009).
150. Lindley, T. & Smallman, R. "The Plastic Deformation of Polycrystalline Vanadium at Low Temperatures." *Acta Metallurgica* **11**, 361–371 (1963).
151. Hall, E. & Algie, S. "The Sigma Phase." *International Materials Reviews* **11**, 61–88 (1966).
152. Stoloff, N. & Davies, R. "The Mechanical Properties of Ordered Alloys." *Progress in Materials Science* **13**, 1–84 (1968).
153. Turchi, P., Kaufman, L. & Liu, Z. "Modeling of Ni–Cr–Mo Based Alloys: Part I—Phase Stability." *CALPHAD* **30**, 70–87 (2006).
154. Watson, A. & Hayes, F. "Some Experiences Modelling the Sigma Phase in the Ni-V System." *Journal of Alloys and Compounds* **320**, 199–206 (2001).
155. Pipitz, E. & Kieffer, R. "Einfluss Von Legierungszusätzen auf Festigkeitseigenschaften und Rekrystallisation Von Vakuumgesintertem Molybdän." *Zeitschrift Für Metallkunde* **46**, 187–194 (1955).

156. Wang, J. "Why $L1_2$ Intermetallics Are Brittle and How to Make Them Ductile." *Journal of Computer-Aided Materials Design* **4**, 157–163 (1998).
157. Farraro, R. & McLellan, R. "High-Temperature Elastic Properties of Polycrystalline Niobium, Tantalum, and Vanadium." *Metallurgical Transactions A-Physical Metallurgy and Materials Science* **10**, 1699–1702 (1979).
158. Harris, B. "The Influence of Some Solutes on Young's Modulus of Niobium." *Journal of Less-Common Metals* **12**, 247–250 (1967).
159. Vasil'eva, E., Tret'yakov, V., Prokoshkin, D. & Pustovalov, V. "Effect of Vanadium and Heat Treatment of the Elastic Characteristics of Niobium." *Metal Science and Heat Treatment* **17**, 706–708 (1975).
160. Valenza, F., Muolo, M. & Passerone, A. "Wetting and Interfacial Phenomena in Relation to Joining of Alumina via Co/Nb/Co Interlayers." *Journal of the European Ceramic Society* (2012) doi: 10.1016/j.jeurceramsoc.2012.10.009
161. Sprengel, W., Denkinger, M. & Mehrer, H. "Multiphase Diffusion in the Co-Nb and Ni-Nb Systems: Part I. Solid-Solid Phase Equilibria and Growth of Intermetallic Phases." *Intermetallics* **2**, 127–135 (1994).
162. Gupta, K. in *Phase Diagrams of Ternary Nickel Alloys* **2**, 83–91 (Indian Institute of Metals, 1991).
163. Pezzotti, G. Unpublished Work. (2011).
164. Eremenko, V., Prima, S. & Tret'yachenko, L. "Phase Diagram for the V-Nb-Ni System and Phase Transformations on Solidification of Alloys." *Russian Metallurgy* **6**, 184–190 (1990).
165. Roux, F. & Vignes, A. "Diffusion Dans Les Systèmes Ti-Nb, Zr-Nb, V-Nb, Mo-Nb, W-Nb." *Revue de Physique Appliquée* **5**, 393–405 (1970).
166. Brunsch, A., Krabichler, T. & Steeb, S. "Anomalous Behaviour During Interdiffusion in the System Nb-Mo." *High Temperatures-High Pressures* **5**, 199–206 (1973).
167. Pridantseva, K. & Solov'eva, N. "Thermal Expansion of Solid Solutions of Metals of Groups VI, V, and IV of the Periodic System with High Melting Points." *Metallovedenie i Termicheskaya Obrabotka Metallov* **8**, 41–44 (1966).
168. Pelleg, J. & Zaklos, Y. "Diffusion of ^{99}Mo in Vanadium." *Philosophical Magazine A-Physics of Condensed Matter Structure Defects and Mechanical Properties* **63**, 439–446 (1991).
169. Mortensen, A. & Cornie, J. "On the Infiltration of Metal Matrix Composites." *Metallurgical Transactions A-Physical Metallurgy and Materials Science* **18**, 1160–1163 (1987).